Geometric percolation of colloidal particles and how it is affected by external fields

Pihlajamaa, I.L.

Award date:
2021

Technische Universiteit
Eindhoven
University of Technology

Department of Applied Physics
Group of Soft Matter and Biological Physics

Geometric percolation of colloidal particles

and how it is affected by external fields

Ilian Pihlajamaa

Supervisors:
prof. dr. ir. P. van der Schoot
R. de Bruijn MSc

Eindhoven, March 2021

Abstract

Experimental work on the electrical percolation threshold of polymeric host materials enriched with electrically conductive nanofillers has produced highly scattered results even for superficially identical formulations. In the literature, many explanations for the underlying phenomenon have been put forth. In particular, the presence of electromagnetic or flow fields is almost inevitable in the production process of nanocomposites and is suggested to be the partial cause of this mutual disagreement in the experiments. To investigate this, we theoretically model percolation in two types of material. First, we consider dispersions of hard spherical particles subject to shear flow. We set up a model that combines a heuristic criterion for percolation and a Smoluchowski theory for the pair structure in shear flow. We find that the structural deformation induced by the shear flow increases or decreases the percolation threshold depending on the shear rate and the surface-to-surface distance over which electron transport occurs. Next, we numerically investigate equilibrium dispersions of hard nanorods subject to external orienting and disorienting quadrupolar fields using the connectedness Ornstein-Zernike formulation, explicitly taking their orientational degrees of freedom and liquid-crystalline transitions into account employing a formal minimisation of the Onsager free energy. We find that external quadrupolar fields can significantly increase the percolation threshold, cause complex re-entrant percolation behaviour, and induce bi- and triaxiality in the shapes of nanofiller clusters.

Contents

Chapter 1

Introduction

The addition of nanoparticles such as carbon nanotubes, carbon black, silver nanowires or graphene to common plastics can enhance their conductive properties tremendously [1–8]. For instance, the incorporation of a slight amount of a carbon nanotube additive into an insulating polymeric host has been shown to increase its electrical conductivity by over ten orders of magnitude [7]. These polymer composites have stirred up a great interest for industrial applications in photovoltaics [9, 10], optoelectronics [11], gas sensing [12], and liquid crystalline displays [13]. They have additionally been suggested for use as actuators [14, 15], smart materials [16, 17], electromagnetic interference shields [18], and optically transparent yet electrically conductive films [19].

Ordinarily, the large effect that nanoparticles have on the conductive properties of their insulating host material is seen in the context of percolation theory [20–22]. If sufficiently many nanofillers are added to the host, they form a conductive network that spans the entire material. It is through this network that electricity (or heat) can be conducted efficiently. At the particle density where a system spanning network is created, a sharp increase in the conductive properties of the material can be observed [23]. The packing fraction associated with this network formation is called the percolation threshold. Percolation theory is primarily aimed at finding this particle concentration. We stress that percolation theory does not predict the actual conductivity of the resulting nanocomposite; it is solely a geometric framework for establishing if a material-spanning network exists.

Common engineering applications require that the nanoparticle density in such composites be as low as possible to retain the advantageous properties of plastics such as their optical transparency, mechanical flexibility, and low manufacturing costs [24]. Therefore, the goal is to design conductive polymer composites that have a nanofiller concentration just above the percolation threshold. It has been shown that this threshold is highly dependent on the degree of anisometry of the nanoparticles [25–27]. For instance, the percolation threshold of ideal rod-like particles scales inversely proportional to their aspect ratio (the length-over-width ratio) [27]. This means that, in theory, it is possible to make the percolation threshold arbitrarily low by increasing the slenderness of the particles. However, since long, stiff particles, such as carbon nanotubes, are prone to breaking, there is a practical limit to the aspect ratio of conductive fillers in nanocomposites [28]. Therefore, it is important to be able to predict the percolation threshold quantitatively to efficiently manufacture conductive polymeric materials.

A major challenge has surfaced in recent decades. It turns out that the percolation threshold is not only very sensitive to the particle shape but also to many other factors, such as their size polydispersity [29–32], inter-particle interactions [33] and to the homogeneity [34] as well as isotropy [35] of their dispersion in the host. This sensitivity is so large, in fact, that results of

percolation experiments under laboratory conditions seem difficult to replicate on a quantitative level due to imperfections such as particle aggregation and alignment by the mixing process [36]. This also implicates that comparisons between experimental studies and theoretical work on the percolation threshold are qualitative at best.

To understand why these factors have such a significant impact on the percolation threshold, extensive analytical analyses have been conducted on all of the abovementioned characteristics for dispersions of rod-like particles [31, 35, 37]. Even after this host of work, physical understanding of the effects of the manufacturing process on the presence of conductive networks in the resulting composite remains lacking. One of the underlying fundamental difficulties is the inherent non-equilibrium nature of the way nanoparticles are commonly dispersed in the polymeric host. When the particle positions are subsequently frozen by polymerisation, a non-equilibrium structure remains. This raises foundational questions around the use of equilibrium liquid state theory to gain insight into the clustering properties of materials with non-equilibrium structures.

To take on this fundamental problem, we theoretically model percolation in a colloid of spherical particles subject to a shear flow. Since such a material is not in equilibrium, we choose to engage this problem with a percolation model that requires only structural input to estimate the percolation threshold. We provide this structural information by solving the non-equilibrium Smoluchowski equation on the two-particle level for the perturbation of the structure relative to that of the corresponding equilibrium material. Since the equilibrium structure of a dispersion of hard spheres is reasonably well understood, we are able to calculate the percolation threshold as a function of the shear strength. We compare the results of this theory with simulation results to establish its accuracy.

To aid the understanding of equilibrium percolation as well, model percolation in an equilibrium dispersion of long, hard, rodlike particles in external orienting and disorienting quadrupolar fields that model the external structural influences of externally applied flow or electromagnetic fields. Since we consider this dispersion in a state of thermal equilibrium with respect to these fields, we can use canonical liquid state theory, adapted for connectedness, to find the percolation threshold. We find that the percolation behaviour in this material is very rich due to the complex interplay between the (dis)orientation induced by the external field and the alignment caused by the excluded volume interactions between the hard rods. To gain further insight, we also analyse the dependence of the particle aspect ratio on the percolation threshold and evaluate the cluster shape in various regimes.

The remainder of this report is divided into five chapters. In the next two chapters, we describe the concepts and methods that we use in the later chapters to gain a physical understanding of the percolating behaviour of particles that experience external influences. In Chapter 2, we present a theoretical framework on the structure and connectivity in equilibrium, based on liquid state theory. In Chapter 3, we describe how to conduct molecular dynamics simulations and numerical clustering analysis. In Chapter 4, we use the concepts introduced in Chapters 2 and 3 to describe percolation of spheres in a shear flow. In Chapter 5, we apply the concepts discussed in Chapter 2 to model percolation in the second material, *i.e.*, long rods subject to external fields. In the last chapter, we give a conclusion and outlook.

Chapter 2

Geometric percolation in the liquid state

Summary

In this chapter, we present a brief, non-rigorous overview of the methods that have been developed in the context of liquid state theory to find the structure and degree of clustering of anisometric particles in equilibrium. In particular, we discuss the canonical Ornstein-Zernike equation and how it can be adapted to describe connectedness instead of structure. The aim of this chapter is mainly to introduce the underlying physical framework of the methods that we use in later chapters.

2.1 Introduction

The goal of this work is to study material spanning conductive networks of particles. In order for pairs of particles to conduct electricity, they do not need to physically touch. If two particles are close enough together, electrons can undergo quantum-mechanical tunnelling to 'hop' from one particle to another. The rate at which they do so decays exponentially with the surface-to-surface distance of the particles [38].

This exponential decay does not need to be taken into account explicitly to model the percolation threshold. It is believed that modelling particle connectedness as a sharp cut-off distance produces equivalent results to an exponentially decaying connectedness probability. Therefore, throughout this work, we do not explicitly take into account the conductivity of the particles, but use a geometric criterion to determine whether particles are connected. For this, we use the so-called cherry pit model: we surround each particle with a connectivity region. If two connectivity regions of particles overlap, we consider them connected. This region does not add any new inter-particle interactions. Therefore, the particles do not know whether they are connected to another particle or not.

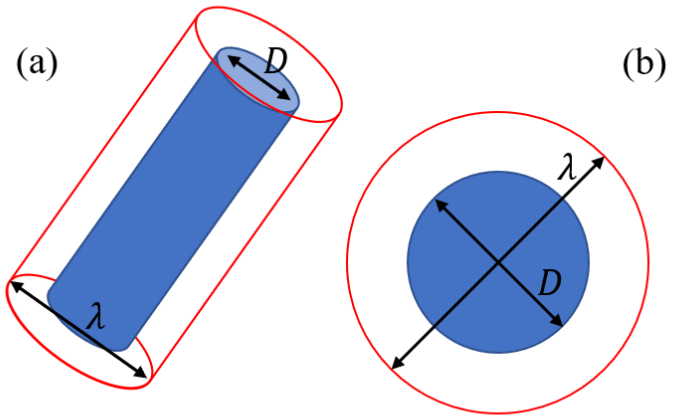

Figure 2.1: *Spherocylindrical (a) and spherical (b) cherry pit particles: we consider hard-core particles with diameter D surrounded by a connectivity shell of size λ which determines whether particles are connected. In the case of spherocylindrical particles, we have not drawn the hemispherical end-caps for clarity.*

In the case of spherical and spherocylindrical particles, we define the thickness of this connectivity shell around the particle by $(\lambda - D)/2$, where D is the hard core diameter of the particles. Here, λ is the total diameter of the connectivity region. This geometry is visualised in Fig. 2.1.

We note that since this cherry pit model does not introduce any new interactions between particles, we are effectively assuming that the particles are impervious to applied electric potentials and temperature gradients between particles. This assumption may hold only if the host matrix is fully polymerised, and the particle positions and orientiations are effectively frozen in before

the conductivity experiment is initiated.

We consider a dispersion of N anisometric particles in a volume V with thermal energy $k_BT = 1/\beta$. In principle, such a dispersion can have a position-dependent number density $\rho(\mathbf{r})$, which we explicitly take into account in this chapter. Since we are mostly interested in homogeneous dispersions however, we drop the position dependence in later chapters and consider it to be a constant $\rho(\mathbf{r}) = \rho = N/V$. Each particle has orientational degrees of freedom. To accommodate for them, we assign to each particle an unit orientation vector $\mathbf{u}$. We define the orientational distribution function $\psi(\mathbf{u})$ such that the probability of finding a particle with an orientation in $[\mathbf{u}, \mathbf{u} + \mathrm{d}\mathbf{u}]$ is $\psi(\mathbf{u})\mathrm{d}\mathbf{u}$. In the isotropic case, where the orientations of all particles are equally likely, we have $\psi(\mathbf{u}) = 1/4\pi$.

To find the particle density at which macroscopic clusters appear, we need to quantify the size of the clusters as a function of density. This is the aim of the remaining sections of this chapter.

2.2 Cluster size

A common method to tackle this problem is to start from the framework of liquid state theory. In the theory of liquids, the pair correlation function $g(\mathbf{r}_1, \mathbf{r}_2, \mathbf{u}_1, \mathbf{u}_2)$ quantifies the probability to find two particles at positions $\mathbf{r}_1$ and $\mathbf{r}_2$ with orientations $\mathbf{u}_1$ and $\mathbf{u}_2$ [39]. It is normalised such that $\iiiint \mathrm{d}\mathbf{r}_1\mathrm{d}\mathbf{r}_2\mathrm{d}\mathbf{u}_1\mathrm{d}\mathbf{u}_2\rho(\mathbf{r}_1)\rho(\mathbf{r}_2)\psi(\mathbf{u}_1)\psi(\mathbf{u}_2)g(\mathbf{r}_1, \mathbf{r}_2, \mathbf{u}_1, \mathbf{u}_2) = N^2$, where the integrations range over all positions and orientation of the particles. The pair correlation function provides detailed information about the microstructure of the arrangement of particles in gases, liquids and solids, and can be used to determine, among others, the static structure factor, the compressibility and the pressure of a material.

For notational convenience, we may choose to abbreviate the positions and orientations of all particles in the following sections. For example, we write the pair correlation function $g(1, 2) \equiv g(\mathbf{r}_1, \mathbf{r}_2, \mathbf{u}_1, \mathbf{u}_2)$. Note that in this new notation, we write the integral $\int \mathrm{d}1(\ldots)$ to abbreviate $\iint \mathrm{d}\mathbf{r}_1\mathrm{d}\mathbf{u}_1\rho(\mathbf{r}_1)\psi(\mathbf{u}_1)(\ldots)$. For example, the normalisation of the pair correlation function is now abbreviated by $\iint \mathrm{d}1\mathrm{d}2g(1, 2) = N^2$.

To use the methods of liquid state theory to our problem of geometric percolation, we divide the pair correlation function into two new functions $g(1, 2) = g^+(1, 2) + g^*(1, 2)$, the pair connectedness function $g^+(\mathbf{r}, \mathbf{r}', \mathbf{u}, \mathbf{u}')$ and the blocking function $g^*(\mathbf{r}, \mathbf{r}', \mathbf{u}, \mathbf{u}')$. They describe the probability of finding connected and disconnected particles with the specified positions and orientations. With these definitions and corresponding normalisations, it is straightforward to see that the number of connected particle pairs is equal to $N_c = \frac{1}{2}\iint \mathrm{d}1\mathrm{d}2g^+(1, 2)$, where the factor of one half is to avoid double counting.

We can use the expression for the number of particle pairs to find the average cluster size [40]. The argument goes as follows. Suppose we have a particle dispersion in which there are n_k clusters consisting of k particles. The total number of particles is known, and thus we have $N = \sum_k n_k k$. The probability that a particle belongs to a cluster of k particles is now kn_k/N. Therefore the average size of the cluster a randomly chosen particle belongs to is given by $S = \sum_k k^2 n_k/N$. The total number of connected particle pairs can now be calculated as the total number of connections within one cluster, summed over all clusters: $N_c = \sum_k n_k k(k-1)/2 = N(S-1)/2$. Using this last identity, together with the earlier obtained expression for N_c, we find

$$S = 1 + \frac{1}{N}\iint \mathrm{d}1\,\mathrm{d}2g^+(1, 2), \tag{2.1}$$

We note that this definition of S corresponds to the weight average cluster size, and not the number

average. We define the percolation threshold to coincide with the location of the divergence of this function. In Chapter 3, we show that this is indeed the choice that gives results consistent with simulations.

2.3 The pair distribution function

In liquid state theory, a successful approximation of the pair distribution function g can be obtained by the Ornstein-Zernike relation. We can adapt this relation to find an approximation for g^+ as well. First, we give a quick overview of the canonical Ornstein-Zernike relation, with emphasis on the underlying structure rather than mathematical rigour. For a more complete overview, we refer to Hansen & McDonald [39]. The derivation of the Ornstein-Zernike relation assumes that particles only interact through pair interaction potentials $U(1,2)$, and that the material is in an ergodic state of thermal equilibrium.

Ornstein and Zernike showed that the pair correlation function g can be related to another function C via an integral equation that was later named after them [41]

$$g(1,2) = 1 + C(1,2) + \int \mathrm{d}3 C(1,3)(g(3,2) - 1). \tag{2.2}$$

Here, C is called the direct correlation function[1], which can in principle be obtained by taking the second functional derivative of the excess free energy with respect to the density. Relation (2.2) is a recipe for finding the pair distribution function g, if the excess free energy is known. This, however, is in general not the case, and one often has to resort to (*ad hoc*) approximations of C.

The structure behind the Ornstein-Zernike relation is more clearly visible if we solve it recursively for g. This yields

$$\begin{aligned} g(1,2) = 1 + C(1,2) + \int \mathrm{d}3 C(1,3)C(3,2) \\ + \iint \mathrm{d}3\mathrm{d}4 C(1,3)C(3,4)C(4,2) + \ldots, \end{aligned} \tag{2.3}$$

which is an infinite sum of integrals. It turns out insightful to write such integrals as diagrams based on graph theory. The above equation then becomes[2]

$g(1,2) = 1 +$ 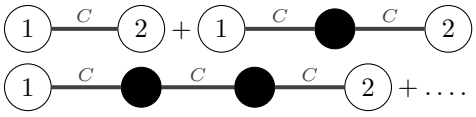 (2.4)

These diagrams allow us to see the structure in the integral expressions. Such diagrams always consist of circles linked by bonds. The white circles, called root points, denote the arguments of the expression that the diagram stands for. For example, the values of all diagrams in the above expression depend on the positions and orientations of particles 1 and 2. The black circles, called field points, denote integrations in the expression. For example, a single black circle denotes the operator $\int \mathrm{d}3(\ldots)$, acting on the remainder of the expression that the diagram represents. The integration variable 3 can be named anything and is therefore not specified in the black circle. A

[1] Note: in many standard texts, the direct correlation function is denoted by the small letter c, which in this work is reserved to denote a concentration. We chose to make it a capital to avoid confusion.

[2] For clarity, we have omitted prefactors that are usually included to account for the multiplicity of the diagrams [39].

bond connecting two circles indicates a function with the two points associated with the circles as arguments. A C-bond connecting two white circles labelled i and j denotes the expression $C(i, j)$ for example.

Eq. (2.4) tells us that the correlations between the locations and orientations of particles are transmitted through chains of intermediate particles. The correlations between directly neighbouring intermediate particles are quantified by the direct correlation function C.

As a result of the ability to apply both graph theory and density functional theory to these diagrams, it can be shown that the direct correlation function $C(1, 2)$ can also be expressed as an infinite sum of integrals. In fact, it has been found to equal the sum of a subset of all diagrams consisting of two white root points labelled 1 and 2 and an arbitrary number of black field points, connected by bonds that are associated with the Mayer function $f(1, 2) \equiv \exp(-\beta U(1, 2)) - 1$. In our case of impenetrable particles, $f = -1$ if the particles overlap and $f = 0$ if they do not. An added constraint to the diagrams in the expansion of C is that they cannot contain a circle that would leave the diagram disconnected upon its removal. Such circles are called connecting circles. The first few terms in the expansion of C are written down below

$C(1,2) =$ 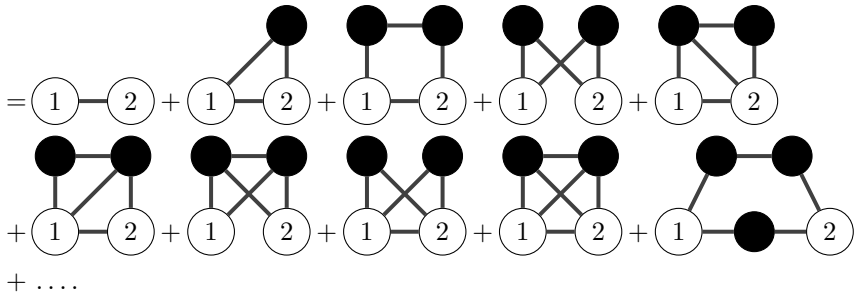 (2.5)

$+ \ldots .$

In the above diagrams, we have omitted the labels f above all bonds for clarity. For example, 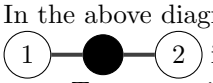 is not part of the expansion because it contains a black connecting circle.

To summarise, we have expressed the pair distribution function g as an infinite sum of integrals of the direct correlation function C (Eq (2.3)), which in turn can be calculated as an infinite sum of integrals of the pair potential (hidden in the Mayer functions f). The usual path forward is to devise an approximation of C either by explicitly neglecting many of the diagrams in its expansion or by bringing forward another expression of C in terms of U and possibly g. After having approximated C, a corresponding approximation can be found for g by solving the Ornstein-Zernike integral equation (2.2). Examples of classical approximations of the expansion (2.5) are the Percus-Yevick, hypernetted chain and second virial closure relations, each with their own merits [39]. In later chapters we make use of both the second virial closure as well as the Percus-Yevick closure.

The second virial closure is only accurate in the limit that $N/V \to 0$, and consists of neglecting all but the first diagrams in the above expansion. Therefore, the remaining closure is written as

$$C(1, 2) \approx f(1, 2). \tag{2.6}$$

The Percus-Yevick closure is more sophisticated, and yields accurate results up to intermediate packing fractions. Its functional form is given by

$$C(1, 2)(f(1, 2) + 1) \approx f(1, 2)g(1, 2), \tag{2.7}$$

which can be shown to exactly reproduce all second and third order diagrams in the expansion of $C(1, 2)$ [42].

Together with either one of these closures, the Ornstein-Zernike equation (2.2) can be solved to find the pair correlation function. In the case of homogeneous dispersions of spherical particles, the pair correlation function becomes dependent only on the distance between the particles $r = |\mathbf{r}_2 - \mathbf{r}_1|$ and is then often referred to as the radial distribution function. We plot the pair correlation function for a dispersion of hard spherical particles in Fig. 2.2, together with simulation results[3]. It is clear that the Percus-Yevick closure is accurate for much higher densities, even near until the fluid-solid transition (which occurs between $\rho_{\text{liquid}} D^3 = 0.94$ and $\rho_{\text{solid}} D^3 = 1.04$ [43]), whereas the second virial closure fails early in the low-intermediate density regime. Since we use the Percus-Yevick closure in Chapter 4 again to find the equilibrium pair correlation function, we report a numerical iterative procedure for finding a solution to the Ornstein-Zernike equation in App. F.

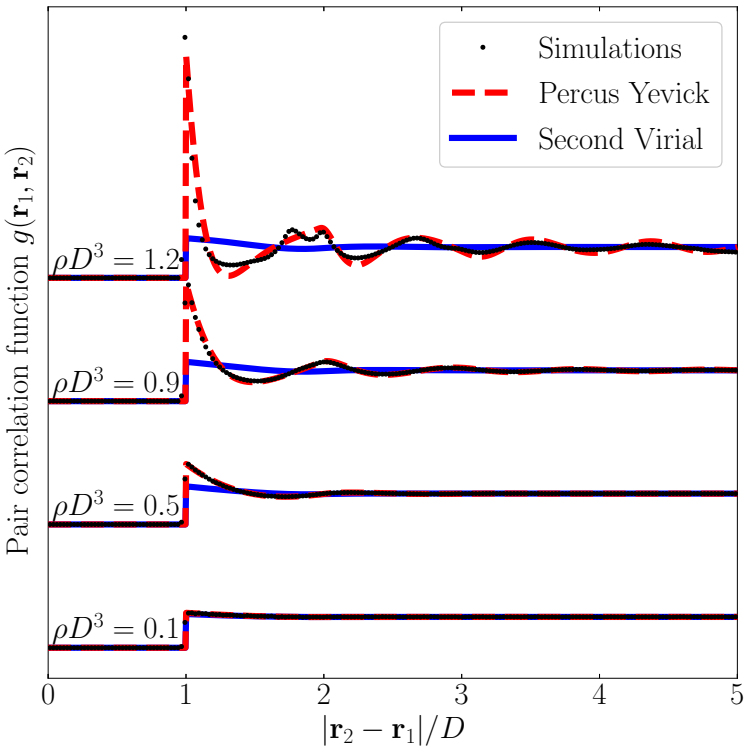

Figure 2.2: *Comparison of the pair correlation functions obtained with the second virial and Percus-Yevick closure for a homogeneously dispersed liquid of hard spheres. The different curves correspond to different densities. We have added an offset between them for clarity. For reference, we also plot the pair correlation function from a simulation of the same particles.*

[3]In fact, the dots and lines in Fig. 2.2 are for particles that interact through the potential given in Eq. (4.22) with $\epsilon_0 = 100$, $\epsilon = k_B T$, and $\sigma = 2^{-1/6} D$. This potential very closely matches hard-sphere interactions, while being more convenient for simulations than true hard-sphere interaction potentials.

2.4 The pair connectedness function

Coniglio *et al.* use the expansions of g and C to find an expression for the pair connectedness function g^+ [40]. To do this, they imagine that particles interact with two effective pair potentials, one describing the interactions between connected particles U^+, and the other describing the interactions between disconnected particles U^*. They are defined such that $U^+ = U$ and $U^* = \infty$ if the particles are connected and $U^+ = \infty$ and $U^* = U$ if they are not. This definition of U^+ and U^* ensures that $\exp(-\beta U) = \exp(-\beta U^+) + \exp(-\beta U^*)$. We can now define the corresponding Mayer functions $f^+ = \exp(-\beta U^+)$ and $f^* = \exp(-\beta U^*) - 1$, such that $f = f^+ + f^*$. Note that these new effective potentials are not connected to physical forces in any way. They are simply introduced to be able to conduct a mathematical cluster analysis.

Now that we have defined a way in which we can divide bonds between particles in connected and disconnected contributions, we can also divide the expansion of the direct correlation function $C = C^+ + C^*$, Eq. (2.5). If we denote a connected $f^+(\mathbf{r}_2, \mathbf{r}_2)$ bond with a bold line (1)—(2) and a disconnected $f^*(\mathbf{r}_2, \mathbf{r}_2)$ bond with a dotted line (1)···(2), the separation can be carried out diagrammatically. For example, the expansion up to third order becomes

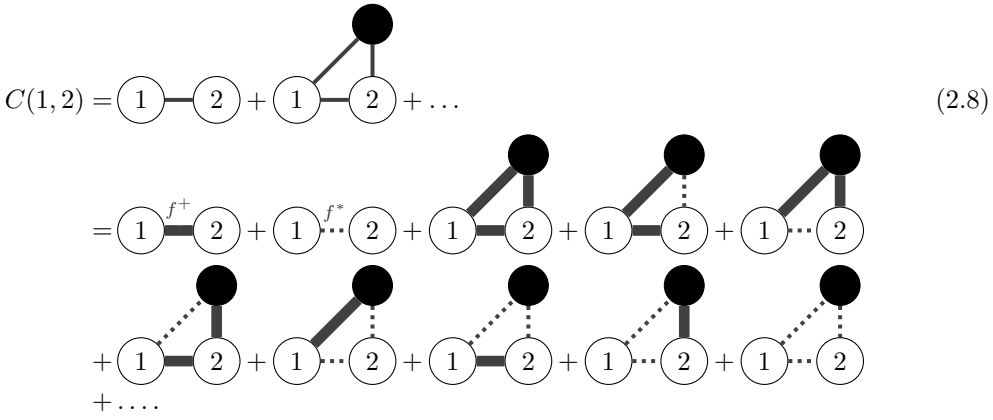

(2.8)

All diagrams with a continuous path of f^+ bonds between the white root points describe a situation in which particles 1 and 2 are connected, and therefore are part of the expansion of C^+, which we call the direct connectedness function. Thus, we write the first terms of the expansion of C^+ as

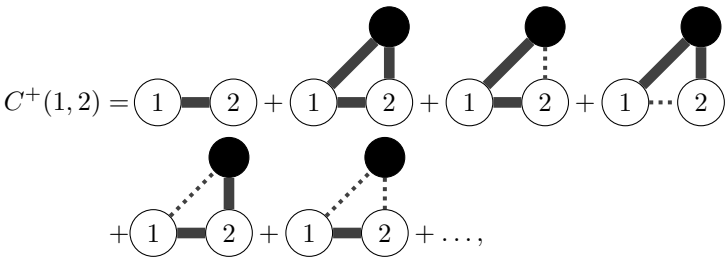

(2.9)

where all the other diagrams belong to C^*. It is straightforward now, to also divide the expansion of g in a connected part g^+ and a disconnected part g^*. Since g is written as a sum of linear chains of C bonds, see Eq. (2.4), it is intuitive that the expansion of g^+ consists solely of chains of C^+ bonds; if there had been any C^* bond in a such a chain, the two white particles would not

be connected. Therefore, we can write

$$g^+(1,2) = \quad + \quad + \quad + \ldots. \tag{2.10}$$

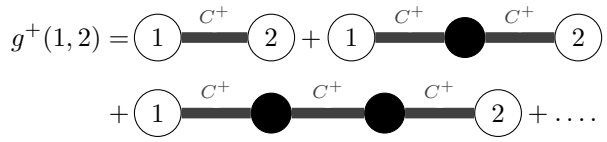

All remaining diagrams, such as 

within the expansion of g add up to g^*. The definitions of f^+ and f^* require us to also include the unity term in g in the expansion of g^*.

At this point, we have everything that we need in order to make headway. We have an expression of the cluster size as a function of the pair connectedness function g^+ (5.7), and in turn an expression of g^+ in terms of C^+, which can be rewritten recursively as

$$g^+(1,2) = C^+(1,2) + \int \mathrm{d}3 C^+(1,3) g^+(3,2), \tag{2.11}$$

and finally, we have an expression of C^+, see Eq. (2.9).

The last hurdle is to find an appropriate approximation for the direct connectedness function C^+. The simplest nontrivial approximation of C^+ is the second virial approximation, which can be obtained by neglecting all diagrams but the first, to end up with

$$C^+(1,2) \approx f^+(1,2) \tag{2.12}$$

A connectedness Percus-Yevick closure can also be constructed, although its form is slightly less elegant [40, 44]

$$C^+(1,2) \approx f^*(1,2) g^+(1,2) \exp(\beta U^+) + f^+(1,2) g(1,2) \exp(\beta U) \tag{2.13}$$

In contradiction to the excellent results of the regular Percus-Yevick closure, the connectedness Percus-Yevick closure shows clear deviations from simulation data, which can be seen in Fig. 2.3, where we show percolation threshold calculated with the Percus-Yevick closure. The Percus-Yevick closure clearly overestimates the percolation threshold significantly [44]. For a quantitative predictions, one must therefore find either a better closure of the connectedness Ornstein-Zernike equations, or use another, possibly heuristic, theory.

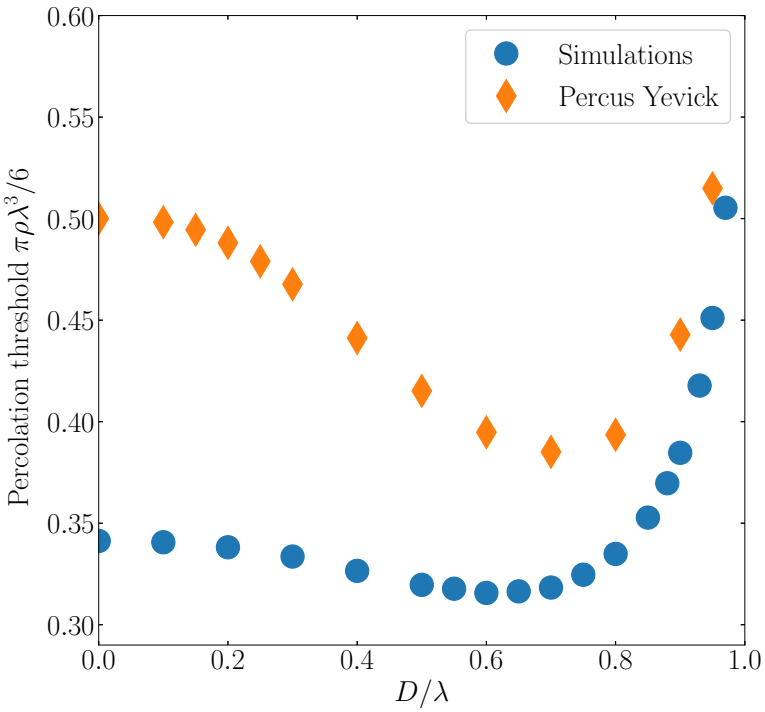

Figure 2.3: *The dimensionless percolation threshold for hard spheres calculated with the connectedness Ornstein-Zernike equation in conjunction with the Percus-Yevick closure as function of the ratio between the hard sphere diameter and the connectivity length. The calculations were by R. de Bruijn using the methods presented in [44]. We also print Monte Carlo simulation results of the same material due to M. Miller.*

2.5 Conclusion

In this section, we have briefly discussed the structure of the methods from liquid state theory that allow us to quantify the equilibrium structure of a liquid through the Ornstein-Zernike equation, and how to adapt this equation to the connectedness Ornstein-Zernike equation in order to describe the clustering behaviour of particles. This allows us to calculate the particle density at which the weight averaged cluster size diverges, which coincides with the density at which material spanning clusters first appear, also called the percolation threshold.

We also show that there is a stark contrast between the regular and connectedness version of the Ornstein-Zernike relation regarding the accuracy of the Percus-Yevick closure.

Chapter 3

Molecular dynamics and numerical cluster analysis

Summary

We present and analyse a method of finding the relation between the structural and the clustering behaviour of dispersions of hard spherical particles by means of computer simulation methods. The methods we present are able to find the percolation threshold in excellent agreement with literature values for relatively small particle trajectory data sets. In full accordance with earlier findings, we find that the spatial correlations induced by the hard-core inter-particle interactions create a non-linearity in the way that the percolation threshold scales with the particle size relative to a connectivity distance. This non-linearity is due to the complex interplay between two phenomena that are dominant at different particle sizes: the excluded volume interactions decrease the number of direct connections each particle can form. However, excluded volume effects also increase the local density around the hard core particle, increasing the number formed connections. Together, these phenomena cause the percolation threshold as function of the size of the hard-core diameter to have a local minimum.

3.1 Introduction

In this chapter, we describe the techniques we use to study the clustering behaviour of hard, spherical particles by means of computer simulations. The goal is not to show findings novel to the literature, but rather to describe comprehensively the simulation method we apply in Chapter 4. The first section of this chapter is devoted to molecular dynamics simulations. Specifically, we discuss how to solve the Langevin equation in a many particle simulation. In the second section, we explore how a set of particle trajectories from a molecular dynamics simulation can be used to gather clustering information, and in particular we describe an efficient method of finding the percolation threshold. In the last section, we discuss and conclude our results.

3.2 Molecular dynamics

In order to elucidate the time-resolved clustering behaviour of particles, we first need a way to generate their trajectories. Monte Carlo simulations are cusomarily used to this end due to their computational efficiency. However, it is difficult to apply them to out-of-equilibrium systems, which we intend to investigate in Chapter 4. Therefore, we instead use molecular dynamics simulations to find particle trajectories. In this section, we give a brief description of this method. If a more comprehensive overview is required, several textbooks have been composed on the subject, *e.g.*, the monograph of Rapaport [45].

Very generally, molecular dynamics simulations involve the large-scale integration of Newton's second law of motion. First, a specified number of particles N is given a position that lies somewhere in three-dimensional space, and they are additionally assigned a random initial velocity such that the temperature of the material corresponds to a prescribed value by the equipartition theorem. For each particle, the force acting on that particle is calculated, and an approximation is made regarding the change of its velocity and position over a small but non-zero time step Δt. This force might be due to some external influence, such as an electric field, or it can be induced by the interaction with another particle. Subsequently, all particle positions and velocities are now updated, and the forces are recalculated. This exercise is repeated until the trajectories of the particles allow for a sufficiently strong statistical analysis. Typically, a simulation consists of a total of 10^5 – 10^9 time steps.

3.2.1 Langevin dynamics

In practice, simulations are often course-grained to improve the efficiency and thereby the total time the simulation takes to run. This implies that some or all of the internal detail and degrees of freedom of simulated molecules or groups of molecules are discarded, retaining only much simpler entities for the computer to deal with. For example, it is not unusual in such simulations for a micron-sized colloidal particle to be treated as a point particle with no internal structure. This point particle interacts with similar point particles by an effective pair potential that is introduced such that it reproduces the behaviour of the original particles as accurately as possible. The search for an effective pair potential that accurately represents the often complex interactions of larger particles is highly non-trivial in many cases and often has to be based on an intricate understanding of the many-body behaviour of type of particle in question [46].

In the study of colloidal suspensions, there is another highly effective method one can use to simplify a molecular dynamics simulation. A colloidal suspension typically consists of large solute particles that are dispersed in a solvent of much smaller particles. In most cases, the equilibrium behaviour of the solvent is reasonably well understood and one is mostly interested in the behaviour of the solute. To that end, solvent particles are often completely removed from

the simulations, but have their effects taken into account implicitly [47]. The collisions of small solvent particles with large solute particles are then modelled by a random force acting on the solute particles. The equation of motion describing the evolution of the trajectory $\mathbf{x}_i(t)$ of a large solute particle under the influence of such an implicit solvent is called the Langevin equation, which is given by

$$m_i \frac{\mathrm{d}^2\mathbf{x}_i}{\mathrm{d}t^2} = -\nabla U(\mathbf{x}_i) - \gamma \frac{\mathrm{d}\mathbf{x}_i}{\mathrm{d}t} + \sqrt{2k_B T\gamma}\mathbf{F}_r(t) \tag{3.1}$$

for $i = 1, \ldots, N$. The Langevin equation states that for every particle, the product of its mass m_i and its acceleration is equal to the sum of three forces. The first force, which is expressed in terms of a potential energy above, is due to the conserved interactions of this solute particle with all other solute particles, in combination with all externally applied forces. The second force describes the damping effect that the solvent particles exert. A particle moving at some velocity through the solvent has to displace all the solvent particles in its way. This force is modelled as the product of a constant damping parameter γ and the velocity of the particle. According to Stokes' law, the damping parameter is related to the size of the particles according to $\gamma = 3\pi\mu\sigma$, where σ is the diameter of the particle, and μ is the dynamic viscosity of the medium. The third and last force is a random force, which describes the way the small solvent particles collide with a stationary solute particle as a random force $\mathbf{F}_r$. This random force has a mean of zero and is delta-correlated in time, implying that

$$\langle \mathbf{F}_r(t) \rangle = 0 \qquad \text{and} \qquad \langle \mathbf{F}_r(t_1)\mathbf{F}_r(t_2) \rangle = \delta(t_2 - t_1), \tag{3.2}$$

where $\delta(t)$ is the dirac-delta distribution and the angular brackets denote an ensemble average. The prefactor of this random force in Eq. (3.1) can be derived from the Fluctuation Dissipation Theorem [48]. The random force term is also responsible for maintaining the temperature of the dispersion, and is, therefore, sometimes also called a Langevin thermostat.

3.2.2 Interactions

The interactions between particles in molecular (or Langevin) dynamics simulations can be very complex. However, our goal is to model hard-core particles, which only prohibit any particle overlap but do not undergo other interactions. In molecular dynamics simulations, it is impractical to use 'true' hard-sphere potentials, since their corresponding forces are non-analytic[1]. Instead, we use a potential that is related to the so-called Lennard-Jones potential. The Lennard-Jones potential is given by

$$U_{\mathrm{LJ}}(r) = 4\epsilon \left(\left(\frac{\sigma}{r}\right)^{12} - \left(\frac{\sigma}{r}\right)^{6} \right). \tag{3.3}$$

Here, ϵ is a parameter that controls the strength of the potential, and σ is the size of the particle. This potential approximates the way in which very typical electroneutral atoms interact, and was first used to predict the viscosity of Argon [50]. The first term models the hard repulsion between particles ultimately due to the Pauli exclusion principle. The second term is the attraction caused by Van der Waals forces, which model the combined electromagnetic attraction caused by London, Debye, and Keesom forces [51].

To model hard-core particles, however, it is customary to ignore the attractive part of the potential and only use the short-ranged repulsion. We accommodate this by adapting the

[1] To use a true hard-sphere potential in a molecular dynamics simulation, it is possible to model the hard-core dynamics using so-called event-driven simulations [49]. This, however, is outside the scope of the present work.

Lennard-Jones potential to what is often called the Weeks-Chandler-Andersen potential [52]

$$U_{\mathrm{WCA}}(r) = \begin{cases} 4\epsilon\left(\left(\frac{\sigma}{r}\right)^{12} - \left(\frac{\sigma}{r}\right)^{6}\right) + \epsilon, & r < 2^{1/6}\sigma \\ 0, & r \geq 2^{1/6}\sigma. \end{cases} \tag{3.4}$$

The removal of the attractive tail of the Lennard-Jones potential causes particles to lose the inclination to aggregate. This ensures that the particles remain homogeneously dispersed throughout the simulation domain, which is essential, since the degree of homogeneity has been shown to have a major influence on the percolation threshold [22, 53]. In the rest of this chapter, we use the value of σ to refer to the size of the particles. Note that results calculated for 'hard' particles interacting through a Weeks-Chandler-Anderson potential with a particle size σ should differ slightly with respect that calculated for particles of the same size interacting with a true hard-sphere potential. We discuss this in more detail in Section 3.3.

3.2.3 Time integration

After having calculated the total force acting on a particle, we need to translate this to an approximation of the displacement of that particle in a finite time period Δt. To do this, we could resort to simple Taylor polynomials,

$$\mathbf{x}(t+\Delta t) = \mathbf{x}(t) + \mathbf{v}(t)\Delta t + \mathbf{a}(t)\frac{\Delta t^2}{2} + \ldots, \tag{3.5}$$

$$\mathbf{v}(t+\Delta t) = \mathbf{v}(t) + \mathbf{a}(t)\Delta t + \ldots \tag{3.6}$$

$$\mathbf{a}(t) = \frac{1}{m}\mathbf{F}(t) \tag{3.7}$$

where we define $\mathbf{F}(t)$ as the total force on a particle, and its velocity $\mathbf{v}(t)$ and acceleration $\mathbf{a}(t)$ as the first and second time derivatives of the particle trajectory. Neglecting all higher order terms provides us with a direct way to calculate the displacement of all particles given the force acting upon them. Unfortunately, this method is notoriously unstable and requires the time step Δt to be chosen impractically small to prevent non-physical explosions [45]. In this work, we use a different time integration scheme, called the Velocity Verlet scheme, which is both more accurate and less prone to instabilities [54].

The Velocity Verlet scheme is very similar to the naive scheme outlined above, but uses a better approximation for the velocity. This results from the fact that this algorithm is one order more accurate than the more simple Taylor method above[2]. At any time step, the scheme consists of performing the following steps in succession: [55]

1. Calculate the new positions using $\mathbf{x}(t+\Delta t) = \mathbf{x}(t) + \mathbf{v}(t)\Delta t + \mathbf{a}(t)\frac{\Delta t^2}{2}$;
2. Using the new position vectors, calculate the new forces on all particles using the pair potentials;
3. Calculate the new acceleration using the force derived from the new particle positions $\mathbf{a}(t+\Delta t) = \frac{1}{m}\mathbf{F}(t+\Delta t)$;
4. Calculate the new velocity using the average of the new and the old acceleration $\mathbf{v}(t+\Delta t) = \mathbf{v}(t) + \Delta t(\mathbf{a}(t) + \mathbf{a}(t+\Delta t)/2$.

The properties of this scheme cause it to be very well suited for molecular dynamics simulations, and it has been adopted as one of the most commonly used integration schemes [55].

[2]The order of an integration scheme describes the scaling of the discretisation error. A second order scheme is a scheme for which the local discretisation error scales with Δt^2.

3.2.4 Boundary conditions

All macroscopic systems—whether they are breaths of air or bars of metal—consist of too many particles to simulate explicitly using modern computers. For example, a typical breath of air contains roughly 10^{20} molecules, whereas the largest molecular dynamics simulation performed to date included 'only' 10^9 particles, and needed to run on 130,000 processors to reach a performance of 1 ns per day [56]. In order to gain any information about bulk properties of materials, it is therefore necessary to introduce periodic boundary conditions. This means that we simulate particles in a finite simulation box, and imagine that this box tiles all of space. Every particle in our simulation box also exists in all other boxes as a *periodic image*. An illustration of this idea is given in Fig. 3.1.

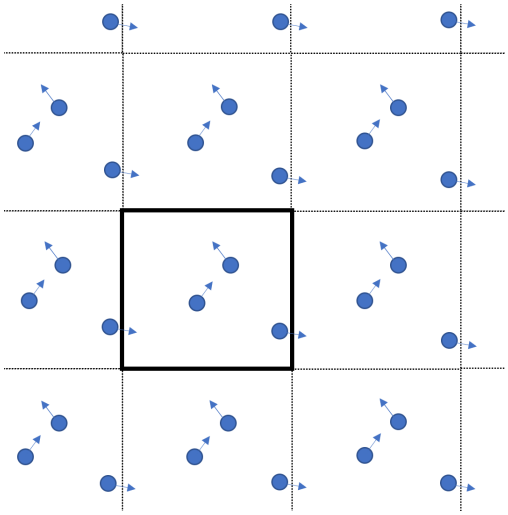

Figure 3.1: *Two-dimensional illustration of periodic boundary conditions. The central simulation box envelops three particles. One of which is about to leave the box on the right, as its image enters on the left.*

In principle, every particle should feel the presence of all images of all other particles and all images of itself. However, by convention, we only calculate the interaction between a particle and the nearest image of another particle, such that the maximal number of interactions to be calculated is equal to $N(N-1)/2$. This convention has the requirement that the box size is much bigger than the range of the interaction. For especially long-ranged interactions such as Coulombic forces, more elaborate methods have been constructed [57]. A second consequence of the finite size of the simulation box is that no correlations can be obtained over a length scale longer than halve of the box size. Therefore, in a simulation of a physical phenomenon that has long range spatial correlations, care must be taken to make the simulation box sufficiently large.

In this chapter, we conduct several Langevin dynamics simulations using the LAMMPS software package that implements the methods we have outlined above [58]. We conduct the simulations in Lennard-Jones units, meaning that the mass m, Boltzmann constant k_B, particle size σ and interaction strength unit ϵ are set to unity. Unless otherwise specified, we set the temperature to $T = \epsilon/k_B$, the damping constant to $\gamma = 10$, and the time step to $\Delta t = 10^{-3}\tau$, where $\tau = \sqrt{m\sigma^2/\epsilon}$ is the unit of time. To obtain SI values of the parameters listed above, a choice has to be made for the mass, size and interaction strength of the simulation. For example,

if we set the particle size to equal one nanometer, the mass to $m = 10^4\,\mathrm{g/mol}$ and the interaction strength such that $T = 300\,\mathrm{K}$, we find by Stokes' law that the dynamic viscosity of the solvent is somewhat lower than that of water. We stress that this choice is not unique, and that our simulations are equally valid for any other choice of units, as long as the other parameters are re-interpreted accordingly.

We initialise the simulation by placing every particle on a lattice and equilibrate the simulation for at least 100τ. After this initial equilibration time we save the particle positions every time unit τ for a total simulation time of $10^4\tau$. We use these particle trajectories in order to calculate the cluster sizes.

3.2.5 Shear simulations

In Chapter 4, we perform simulations of dispersions of particles in simple shear flow. This means that we assume that the colloidal particles are not dispersed in a solvent at rest, but in a solvent with a positionally dependent velocity $v_x = \dot{\gamma} y$, where $\dot{\gamma}$ is the shear rate. To effectively simulate this with an implicit solvent, we need to implement two changes. Firstly, whenever a particle passes one of the periodic boundaries in the y-direction, we need to remap its velocity in the x-direction to match its new location. For example, if a particle leaves the positive y-boundary, its image entering the simulation through the negative y-boundary has its x-velocity changed by $-\dot{\gamma} L_y$, where L_y is the box dimension in the y-direction. Such boundary conditions are called Lees-Edwards boundary conditions [59].

The second aspect we need to change is the thermostat. To ensure that we are simulating particles at a given temperature T, we need to take into account that the background shear velocity should not contribute to the calculation of the global temperature. Therefore, one needs to use the velocity of the particles relative to the local background velocity in the temperature calculation. This choice effectively means that we simulate the particles in local equilibrium with respect to the moving background fluid.

Having implemented these adaptations, our simulations show a linear velocity profile as intended. To be quantitative and be able to compare with other work, two dimensionless numbers are often introduced. The first is called the Peclet number $\mathrm{Pe} = \dot{\gamma}\sigma^2/4D_0$, and is used to quantify the strength of the shear flow, relative to the diffusion. In its definition, $D_0 = k_B T/\gamma$ is the single particle diffusion constant, which can also be determined by calculating the slope of the mean squared displacement of isolated particles $\left\langle (\mathbf{x}(t) - \mathbf{x}(0))^2 \right\rangle = 6D_0 t$ in the absence of a flow field. The second number is the particle Reynolds number $\mathrm{Re_p} = \rho_s \dot{\gamma}\sigma^2/4\eta = 3\pi\rho_s\dot{\gamma}\sigma^3/4\gamma$, where ρ_s is the density of the solvent. The particle Reynolds number quantifies the relative effect of the flow and the inertia on the motion of the particle. Using the example parameters of above, and assuming that the solvent is water, these dimensionless numbers are given by $\mathrm{Pe} = 2.5\dot{\gamma}$ and $\mathrm{Re_p} \approx 10^{-}2\dot{\gamma}$, where $\dot{\gamma}$ is given in units of τ^{-1}. The fact that the particle Reynolds number is low indicates that the role of inertia is small. Indeed, in much of the analysis on sheared colloidal dispersions, the particle Reynolds number is assumed to vanish. This places us in the Stokes flow regime, where the governing equations for the particle motion are linear [60]. Throughout the remainder of this document, we make the same assumption.

3.3 Cluster analysis

In this section, we describe the methods that we apply in order to analyse particle clustering. Throughout this document, we approach connectivity and percolation purely geometrically, *i.e.*, we introduce some distance criterion λ to be satisfied in order to consider particles connected, as described in Chapter 2. Since this does not introduce any new interactions or bonds, we can

simply use the full molecular dynamics trajectories without any alterations, and extract the clustering behaviour. We use the same connectivity criterion as described in Chapter 2: if the distance between the centres of mass of two particles is smaller than the connectivity length λ, we consider the particles to be directly connected. Two particles can be indirectly connected through direct connections with other particles, in which way larger clusters are created.

To calculate what particles should be grouped into clusters, we perform a full hierarchical clustering procedure to find the linkage matrix for a given set of particle positions, using the algorithm presented in Ref. [61]. The rows of the linkage matrix in essence describe the order in which clusters are merged as the connectivity length λ increases. Each row of the matrix includes the labels of the particles that are merged, and the distance between the clusters that are merged. For example, the first row always indicates that the pair of particles with the smallest mutual distance is merged into a cluster of two particles. The last row describes the merger of two clusters into a single cluster that encompasses all particles in the simulation box.

Using this linkage matrix, it is relatively easy to find how the particles should be divided into clusters for a specific value of λ. To do this, we iterate over the rows of the matrix, clustering particles as prescribed, until we reach a merger with a cluster distance larger than our value of λ.

3.3.1 Mean cluster size

Having defined the way in which we cluster particles, it is now possible to measure how the average cluster size behaves as we change the density and hard-core diameter of the particles. In Fig. 3.2a, we logarithmically plot the average cluster size for varying connectivity volume fraction, that we define as $\varphi_\lambda = \pi\rho\lambda^3/6$ for two system sizes. In the figure, we also make a distinction between the number average cluster size $\sum_k kn_k / \sum_k n_k = N/\sum_k n_k$, and the weight average cluster size $\sum_k k^2 n_k/N$, where n_k is the number of clusters of k particles. As is to be expected, for very low connectivity volume fractions, both mean cluster sizes are unity, since no particles are connected. As the connectivity volume fraction increases, the mean cluster size also increases, until it saturates when all particles are connected. The mean cluster size in that case is equal to the total number of particles in the simulation, which is a finite-size effect.

In the intermediate regime, the number average cluster size and the weight average cluster size show qualitatively different behaviour. The number average cluster size seems to increase exponentially with the connectivity volume fraction, visible from the linear behaviour in the figure. The weight averaged cluster size, however, seems to diverge at a fixed connectivity length. Of course, since our system is finite, a real divergence is impossible giving rise to a quick saturation of the cluster size. The location of this divergence of the weight averaged cluster size can be identified as the percolation threshold, as we stated in Section 2.2. We can clarify this by plotting the same figure for non-interacting particles, in which case the percolation threshold is established to six decimal places to be $\pi\rho\lambda^3/6 = 0.341889(3)$ [62]. This value roughly coincides with the inflection point of the weight average cluster sizes in Fig. 3.2b.

If we compare Fig. 3.2a with Fig. 3.2b, we can clearly see the effect that the hard core repulsion has on the mean cluster size. This effect is twofold. Firstly, the repulsion in the case of interacting particles prevents particles from being connected as long as the connectivity length is smaller than the particle diameter. This means that the mean cluster size only starts significantly increasing as the connectivity volume fraction is larger than the hard core volume fraction $\pi\rho\sigma^3/6 \approx 0.37$. Secondly, the excluded volume effect of the hard cores also decreases the variance in the nearest neighbour distances between particles. This implies that the connectivity length at which all particles are connected in a single cluster is much lower. This is clearly visible in the figures through the fact that the number average cluster size saturates at much lower

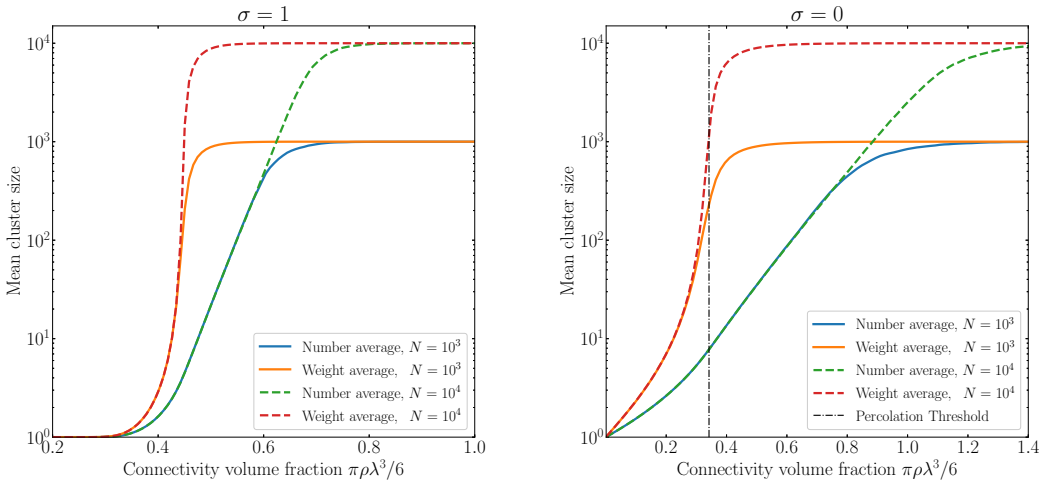

(a) **(b)**

Figure 3.2: *The weight- and number-averaged cluster size for hard (a) and penetrable (b) spheres as a function of the connectivity volume fraction $\pi\rho\lambda^3/6$ at number density $\rho\sigma^3 = 0.7$. In figure (b), we indicate the literature value of the percolation threshold, which coincides with the location at which the weight averaged cluster size grows most rapidly. Both the number- and weight-averaged cluster size are shown for two different system sizes of $N = 10^3$ and $N = 10^4$ particles. This system size determines to what value the mean cluster sizes saturate.*

connectivity length for interacting particles than it does for non-interacting particles.

It is possible to obtain the percolation threshold by the analysis of how the weight averaged cluster size behaves as the connectivity length increases, at constant density. However, a more accurate and direct method has been developed in literature, which relies on finding the probability that a percolating cluster appears in a simulation, and investigating how this probability scales with system size. In the next section, we analyse and apply this method to find how the percolation threshold behaves as the ratio σ/λ changes.

3.3.2 Percolation threshold

In the thermodynamic limit, the percolation threshold is well-defined. That is, there exists a volume fraction above which a percolating network always forms, and below which it never forms. A percolating network can be understood as a network that spans the entire material, or in other words, a network that creates a path from one side of the material to the other. In a finite simulation, unfortunately, there are two difficulties that are not present in 'infinitely'[3] large materials. Firstly, the definition of a percolating network is ambiguous. Should this imply that the network touches opposite ends of the simulation box, or that it connects to its image through the periodic boundaries to form an effectively infinite network? Secondly, in finite systems, the percolation threshold does not exist, *i.e.*, there is a nonzero probability that a dispersion of particles well below the percolation threshold happens to span the entire simulation box. This

[3]By infinite, we mean that it satisfies the thermodynamic limit. For all our intents and purposes, any macroscopic material is infinite.

means that we need a way to extract the percolation threshold from finite simulations, while it is by definition a process that happens on infinite scales. In short, the first problem is how to define a percolating cluster in a finite system, and the second is how to define the percolation threshold. We deal with the former first and revisit the latter later in this section.

The question of how to define a percolating cluster in finite simulations has been answered in different ways in the literature [63]. The most common approach is to define a percolating cluster to be either a spanning cluster or a wrapping cluster. A spanning cluster is a cluster that constitutes a continuous path from any boundary of the simulation box to the opposite boundary. It does thereby span the simulation box, but it does not necessarily span the periodic continuation of the simulation box. A wrapping cluster is a cluster that is connected through the periodic boundaries to an image of itself, thereby spanning the continuation of the simulation box, but not necessarily the simulation box itself. In some works, a percolating network is required to span both the simulation box and its periodic continuation. In this work, we call such clusters bridging. To clarify this, we graphically illustrate our three different definitions of a percolating cluster in Fig. 3.3. In Fig. 3.3a, we show an example of a spanning cluster. Additionally, we show a bridging and a non-bridging wrapping cluster in Figs. 3.3b and 3.3c. We stress that all bridging clusters also belong to the set of all spanning and wrapping clusters.

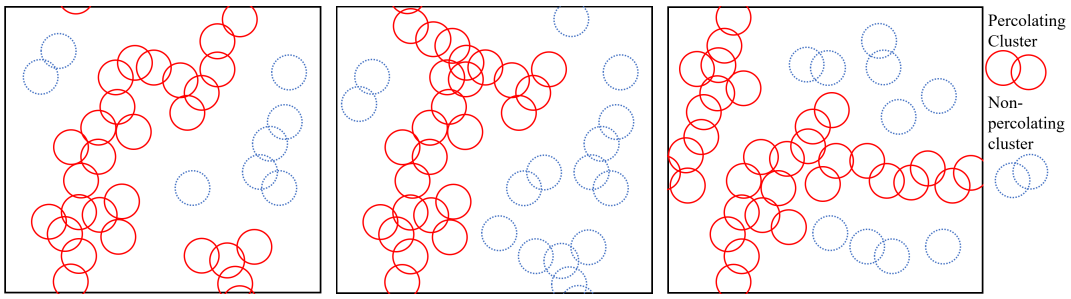

Figure 3.3: *Three different definitions for percolating clusters, illustrated in two dimensions: (a) A spanning cluster that connects the boundaries of the simulation box, but does not span the periodic continuation of the simulation box; (b) A bridging cluster which spans both the simulation box and its periodic continuation; (c) A wrapping, but not bridging cluster that spans the entire material but not the simulation box.*

Each of the three definitions has been used in the literature of simulations of the percolation threshold. For example, Refs. [64–66] use spanning clusters in their analysis, Refs. [53, 67] use wrapping clusters, and [68] use bridging clusters. The difference between the latter two definitions is subtle and not often made explicit, but as we show later in this chapter, if all wrapping clusters are included, a significantly more accurate prediction for the percolation threshold is obtained at a given simulation size at the cost of being slightly more computationally expensive.

One should also choose whether to require a percolating cluster to percolate in at least any one or two directions [63], or in precisely one, two or three directions [69]. For simplicity, we choose to require that a percolating network percolates in at least any one of the three directions. We note that all of the above definitions converge to the same percolation threshold as the simulation size increases. The speed of this convergence, however, may vary.

We now address the second problem we posed earlier this section. In order to define the percolation threshold in a finite system, such that it is independent of the simulation size and that it corresponds to the percolation threshold of an infinitely large material, we calculate the

percolation probability $P_{\mathrm{p}}(\lambda)$ as a function of the connectivity volume fraction λ. This probability corresponds to the fraction of particle configurations that include a percolating cluster if the connectivity length is set to a value of λ. In the thermodynamic limit, this probability is zero below the percolation threshold and one above. However, in finite simulations, it is a monotonically increasing function that becomes steeper as the number of particles increases.

We calculate this probability in a method similar to that presented by Nigro *et al.* [70]. Given the set of particle positions at t_i, we calculate the critical value $\lambda_{c,i}$ for the connectivity length that first produces a percolating cluster. This critical value indicates that in that particle configuration a percolating network is produced for all $\lambda \geq \lambda_c$, since increasing the connectivity length can never disconnect any particles. Therefore, we can use the set of these critical connectivity lengths to find the percolation probability $P_{\mathrm{p}}(\lambda)$. The resulting approximation is

$$P_{\mathrm{p}}(\lambda) \approx \frac{1}{N_t} \sum_{i=1}^{N_t} \vartheta(\lambda - \lambda_{c,i}), \tag{3.8}$$

where $\vartheta(x)$ is the Heaviside step function and N_t is the number of particle configurations sampled.

The procedure described above is different from the more common discrete sampling of $P_{\mathrm{p}}(\lambda)$, where the probability function is estimated at several predefined values of λ by generating and averaging over a large number of independent configurations for each λ. We believe that the advantages of the method we use over this discrete sampling method are that each particle configuration contributes information for all λ, reducing the total number of independent configurations necessary to get similarly strong statistics. Additionally, this method ensures that the percolation probability $P_{\mathrm{p}}(\lambda)$ is monotonically increasing by construction, further decreasing the statistical noise in the final probability function. Lastly, it eliminates all interpolation errors that are introduced when the value of the percolation probability is needed at some specified value of the connectivity length λ that was not part of the set of values on which it was sampled.

To find the critical value of the connectivity length $\lambda_{c,i}$ in a sample, we perform a full hierarchical clustering procedure to find the linkage matrix for a given set of particle positions without taking the boundary conditions into account. As explained earlier, this linkage matrix quantifies in which order the particles should be clusters with increasing λ. After this linkage matrix is calculated, it is not difficult to determine to which cluster each particle belongs for a specific connectivity length λ. This information can be used to determine whether or not a spanning, wrapping or bridging cluster has formed. The algorithm for detecting spanning and bridging clusters from here is trivial.

To find all the wrapping clusters, we construct a cluster graph in which each vertex is a cluster and each edge indicates a connection from one cluster to another through one of the periodic boundary conditions[4]. We also include information about through which boundary the connections are made. In order to find a continuous path from one cluster to an image of itself, we use a breadth-first search algorithm on the cluster graph [71]. This procedure is visualised by the schematic in Fig. 3.4. If such a path is found for any cluster, we know that a percolating cluster exists and what particles it comprises. With a simple binary (bisection) search, we can now determine the smallest λ for which a percolating cluster is formed, which we call $\lambda_{c,i}$. The set of $\lambda_{c,i}$ for all i lets us determine the percolation probability with Eq. (3.8). We note that in three dimensions, the continuous wrapping paths from a cluster to one of its images can become quite complex.

Once the percolation probability function is obtained, there are several methods available

[4]In the language of graph theory, a vertex is a circle, and an edge is a connection between circles.

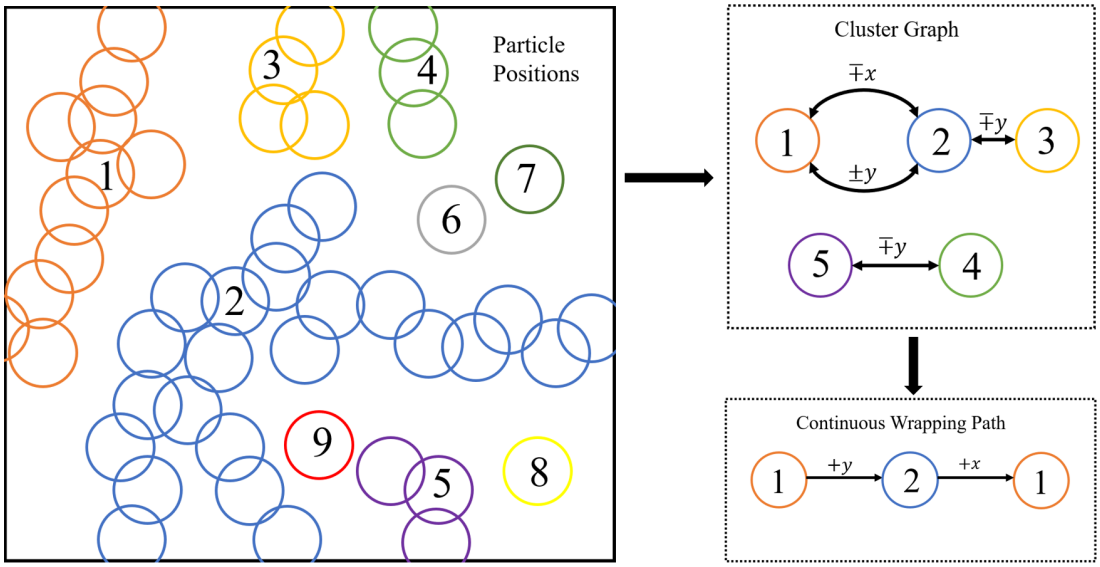

Figure 3.4: *Schematic of the procedure by which we determine the existence of a wrapping cluster. Given a set of particle positions, we first naively divide them into clusters without taking the boundary conditions into account. Next, we construct a graph containing information about what cluster is connected to what other cluster through the periodic boundaries. For example, an arrow from 1 to 2 labelled with a $\mp x$ indicates that 1 is connected to 2 through the $-x$-boundary, and 2 to 1 through the $+x$-boundary. We perform a breadth-first search on this graph to find a continuous path from any cluster to an image of itself. The final wrapping cluster in the cartoon consists of the clusters labelled 1, 2, and 3, including all their images.*

by which the percolation threshold can be extracted. In the thermodynamic limit, we know that the percolation probability vanishes below the percolation threshold, and is equal to unity above it. This allows us to find the percolation threshold with relative ease in a multitude of ways. For example, one can find the connectivity volume fraction where the percolation probability equals some specified value, say $P_{\mathrm{p}}(\lambda) = 0.5$, for multiple simulation sizes at constant number density and extrapolate this location to $1/N \to 0$, where N is the number of particles in the simulation box [68]. There are many more methods for achieving the same results, some of which have the benefit of determining the relevant critical exponents *en passant* [66]. A relatively simple method, which we employ in this work, is to find the intersection between two percolation probability curves at different system sizes [63]. If the simulation contains sufficiently many particles, this intersection point accurately approximates the percolation threshold. In Fig. 3.5, we show the percolation probabilities obtained for spanning, wrapping and bridging clusters for different cluster sizes for non-interacting particles. Each curve is determined from the trajectories from one molecular dynamics simulation, from which in every time span of τ one particle configuration is used up to a total of $N_t = 10^4$ configurations. In Fig 3.5, we also indicate percolation threshold.

We find that the intersections of the probability curves for all three methods converge to the same percolation threshold. However, the wrapping method converges significantly faster and for smaller system sizes than the other two methods do, corroborating the earlier findings of Ref. [63]. Another interesting feature in Fig. 3.5 is the considerable difference between the curves pertaining to the curves of wrapping and bridging clusters. At the percolation threshold, the

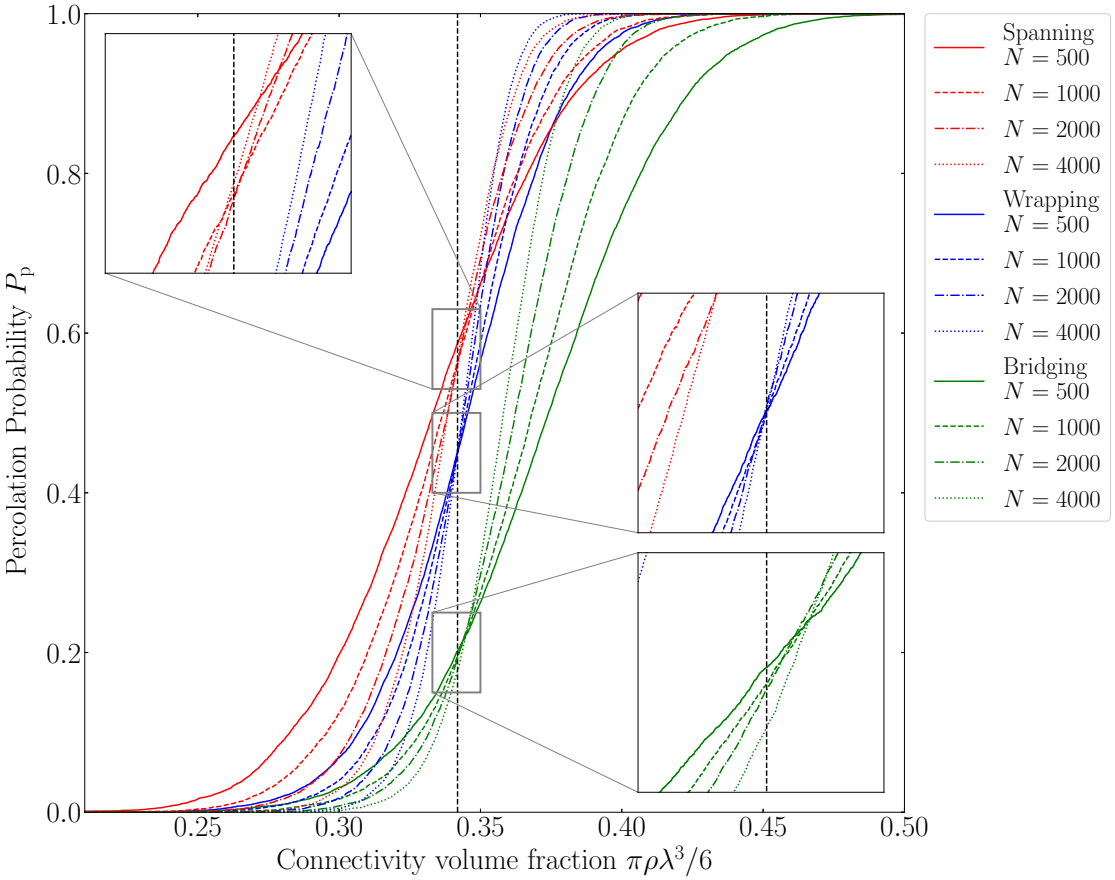

Figure 3.5: *Percolation probability curves P_p as a function of the connectivity volume fraction $\pi\rho\lambda^3/6$ for the three different definitions of percolating clusters of non-interacting particles: spanning clusters, wrapping clusters and bridging clusters. Each set of probability curves is plotted for four different system sizes N. The dashed black line indicates the known percolation threshold [62], and the insets show where the curves for the different definitions intersect each other.*

fractions of wrapping clusters that bridge is smaller than 50%, independent of the simulation size. This means that at the threshold, most clusters are not connected to any of their six nearest images, but to ones located in further away cells.

In the rest of this work, we use the intersection between the probability curves of simulations of $N = 500$ and $N = 4000$ with the wrapping cluster criterion to determine the percolation threshold, with a total of $N_t = 10^4$ configurations. For non-interacting particles, this yields a percolation threshold of $\pi\rho\lambda^3/6 = 0.34187$, which deviates less than 0.01% from the literature value [62].

Having fully established the methods by which we can determine the percolation threshold, we can evaluate the effect that hard-core interactions exert on it. To do this, we conduct molecular dynamics simulations for different values of the Lennard-Jones particle size σ at constant number density. In Fig. 3.6a, we plot the resulting percolation threshold as a function of σ/λ. We see that for small to intermediate σ, the percolation threshold decreases, whereas for high σ, the trend reverses and the percolation threshold increases with an increase in particle size.

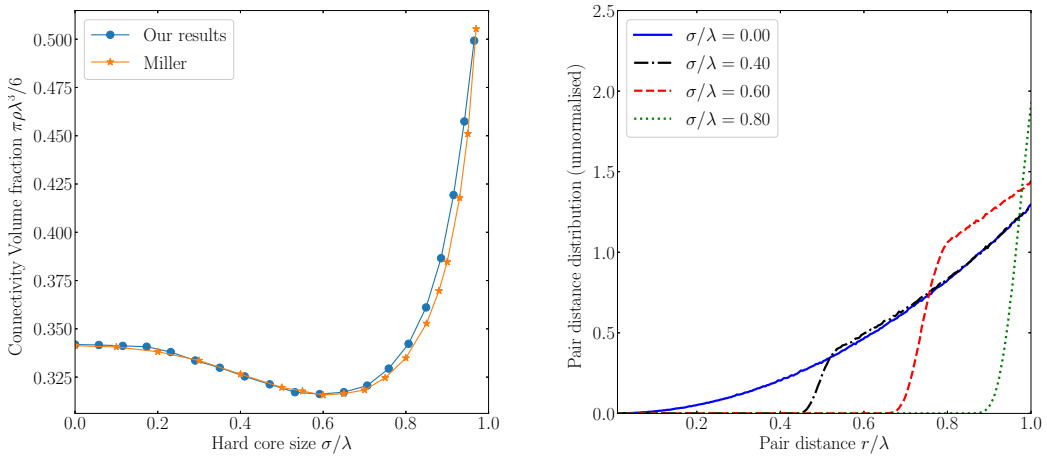

(a) **(b)**

Figure 3.6: *(a) The dimensionless percolation threshold $\pi\rho\lambda^3/6$ as a function of the ratio of the particle size σ and the connectivity length λ, as determined by the procedure described in the main text. Also plotted are the results of the equilibrated hard-sphere (diameter σ) Monte Carlo simulations due to Miller [72]. In (b) we present the pair distance distribution ($\propto r^2 g(r)$) at connectivity volume fraction $\rho\pi\lambda^3/6 = 0.3$ for varying σ/λ ratios. The area under these curves is proportional to the coordination number, i.e., the average number of direct connections that each particle has.*

This behaviour can be explained as the result of the interplay between two physical phenomena. These phenomena can be seen more clearly in Fig. 3.6b, where the pair distance distribution, which is proportional to $r^2 g(r)$, is plotted at the percolation threshold for three different values of the ratio σ/λ as a function of the particle distance. We show only small distances $0 \leq r \leq \lambda$, where the pair of particles form direct connections. If $\sigma/\lambda = 0$, the pair distance distribution scales quadratically with r, since $g(r) = 1$ in that case. For $0 < \sigma/\lambda 0 < 1$, the excluded volume interactions prohibit particles from being very close together, which decreases the number of direct connections each particle has. This phenomenon causes the percolation threshold to increase as σ/λ increases, and causes the very steep rise for high σ/λ, since the volume in which particles can be directly connected becomes very small. For intermediate values of σ/λ, this effect is subdominant to a second phenomenon, which causes the local minimum in the percolation threshold seen in Fig. 3.6a.

Since an increase of the hard excluded volume increases the particle crowding, the local density around a particle's hard core increases. This in turn increases the number of direct connections each particle has. The connections that this phenomenon adds are more important for long-range connectivity than the connections that the hard particle excludes, because they bridge larger distances. This the reason why the percolation threshold can be decreased by excluded volume interactions.

In Fig. 3.6a, we also plot the results of equilibrated Monte Carlo simulations of percolation of hard spheres due to Ref. [72]. We see that for small σ/λ, the deviations with our data are negligible and can be attributed to statistical noise on either side. For larger values of σ/λ,

we can see the effect of the different interaction potentials, implicating that a Weeks-Chandler-Andersen potential slightly increases the percolation threshold compared to a true hard-sphere potential.

3.4 Discussion and conclusion

In this chapter, we have described a simulational method and analysis framework to find the percolation threshold in dispersions of spherical interacting particles. We find that our method gives results consistent to very high accuracy with known literature values. The influence of hard core interactions between the particles either decreases or increases the percolation threshold depending on the size of the particle relative to the connectivity length. This nonlinearity is explained as the combined effect of two phenomena. On the one hand, the excluded volume interactions decrease the number of direct connections each particle makes by decreasing the volume in which particles can be connected. On the other, the expulsion of particles by the excluded-volume effects causes a local increase in the microscopic density around the particles, which aids long-range connectivity. Concluding, we believe that a comparison between previous literature data and results generated by the method described in this chapter provide sufficient confidence that we can apply the method to finding the percolation threshold in sheared suspensions too. Therefore, we apply the method described above to percolation of this non-equilibrium system to test the accuracy of the theoretical work presented in Chapter 4.

Currently, a method of analytically predicting the percolation threshold of (hard) spheres with quantitative precision remains elusive [73]. In contrast to the case of rodlike particles, described in Chapter 5, closures for connectedness Ornstein-Zernike equation fail to quantitatively predict the percolation threshold, despite being highly accurate for predicting the structure of hard-sphere fluids [44]. Other methods, such as the one we extensively use in Chapter 4, often rely either on fitting procedures or other heuristic arguments. In the interest of aiding the development of new analytical tools with more predictive power, we provide spatial and temporospatial pair connectedness, blocking and correlation functions slightly above and below the percolation threshold for various values of the hard sphere volume fraction, in Appendix E.

Chapter 4

Percolation of spherical colloids in shear flow

Summary

In this chapter, we present a model that is designed to predict the percolation threshold in an out-of-equilibrium dispersion of spherical particles subject to simple shear flow. The model combines the heuristic percolation criterion of Alon *et al.* with a theoretical description of the shear-induced distortion of the structure by Blawzdziewicz *et al.* for dilute suspensions without hydrodynamic interactions [74, 75]. To test the accuracy of the model and its ingredients, we compare with simulation results. We find that shear flow can both slightly increase and decrease the percolation threshold, depending on the connectivity length. We conjecture that the decrease is due to the emergence of shear-induced linear contact clusters. This conjecture is supported by our simulation finding that shear flow elongates clusters.

4.1 Introduction

If a polymer composite host is enriched with nanofiller particles, the degree of homogeneity of the dispersion of the nanoparticles is of great influence to the resulting enhancement of the properties of the polymer composite [76]. Hence, great care is taken in the manufacturing process to disperse the nanofillers evenly. Often this is done by techniques such as sonication, manual mixing or shear mixing, followed by casting and curing the composite [77]. These methods can successfully help dispersing the particles and preventing aggregation of the nanofillers. However, because the curing is done relatively quickly after the mixing—to prevent aggregations—the structure of the nanofillers is essentially frozen in, preventing them to reach their thermodynamic equilibrium configurations.

This means that if the goal is to model the percolation threshold in such polymer composites, the use of equilibrium liquid state theory as described in Chapter 2, is fundamentally flawed since the particles cannot be assumed to behave as if they would in equilibrium. To circumvent this issue, a quantitative, out-of-equilibrium percolation theory is needed. Unfortunately, no such theory is known to the authors. An alternative is to take a more heuristic approach, such as we do in this chapter. We use a simple geometric criterion for the percolation threshold that was developed to be able to predict the percolation threshold for particles of any shape from their pair correlation function[1] [74]. We combine this with a Smoluchowski equation for the pair correlation function of particles in shear flow. Together, these two ingredients provide us with a relatively simple way to qualitatively predict the percolation threshold in sheared dispersions.

In this work, we restrict ourselves to dispersions of spherical particles. In principle, a model such as this could be constructed for anisometric particles as well. However, the complicated dynamics of such particles induced by a shear flow in combination with their phase transition behaviour would render such a model either much more complicated or much less predictive. Even spherical particles exhibit nontrivial properties induced by shear flow. For example, an applied shear flow is known to either increase or decrease the viscosity of the medium significantly depending on the strength of the flow field, phenomena which are known as shear thinning and thickening [60]. Additionally, sheared particles have been reported to aggregate hydrodynamically in chain-like structures at low to moderate volume fractions [78, 79], and have been predicted to exhibit long-range order near walls [80]. Moreover, a shear strain can hysteretically deform the crystalline structure of densely packed spherical particles into a so-called sliding layer structures, or can break it completely in case of sufficiently strong flow fields [81].

In equilibrium, hard-core particles have infinitely brief collisions. In sheared dispersions of which the particles are sufficiently large that the shear flow dominates the diffusive mobility of the particles, however, two hard-core repulsive particles may hydrodynamically stick to each other for finite contact times. On the basis of this insight, de Gennes conjectures that infinite clusters appear at some critical volume fraction, where such clusters comprise an infinite number of physically touching particles [82]. This is in close analogy with the cherry-pit percolation problem where the particles need not touch to be considered connected. Because of the sheared origin of these 'contact clusters', de Gennes argues that such clusters must have a very transient nature, meaning that connections between particles are formed and broken in accordance with some average contact time. These conjectures has recently been provided with evidence by simulations, which find the emergence of simulation spanning contact clusters at volume fractions around $\varphi = 0.3-0.4$, depending on the simulation size [83]. Additionally, the simulations indicate that the clusters are roughly linear, extremely transient and that they conform reasonably well to standard isotropic percolation theory. Two-dimensional simulations of similar sheared dispersions also show that such clusters have a highly transient nature, indicated by their stretching, compressing,

[1] which will turn out to be accurate as long as the particles are not very 'pointy'.

and rotating behaviour, the latter leading to the transport of particles in the gradient direction perpendicular to the flow field [84].

Many theories have been proposed to describe the structure of particles in a flow field analytically. The starting point of which is often the Smoluchowski equation that describes the dynamics of the many-body particle distribution function [85, 86]. The N-body equation is averaged over $N-2$ degrees of freedom to yield an equation for the 2-body distribution, which is closely related to the pair correlation function. In its general form, this equation exactly reproduces the dynamics of the many-body distribution function at the Brownian timescale, taking into account all many-body colloidal and hydrodynamic interactions. It is, however, still of little practical use since it explicitly contains the unknown 3-body distribution function, for which an equation can be constructed similarly by averaging over the $N-3$ degrees of freedom. This equation then contains a 4-body distribution, and so on, creating a hierarchy of coupled integro-differential equations. In practise, one often approximates the 3-body interactions either by factorising them into 2-body interactions [87–89] or related approximations [90–93], or by neglecting them altogether [75, 94–96]. A similar choice must be made for hydrodynamic interactions: they are either disregarded [75, 89, 93], approximated by some heuristically known parametrisation [94], or taken into full account at the two-body level [91, 97].

In this chapter, we follow the work of Blawzdziewicz and Szamel who disregard all hydrodynamic and three-body interactions to produce an equation for the pair correlation function of hard spheres in a simple shear flow that can be solved analytically with relative ease [75]. The resulting radial distribution function is believed to become exact in the dilute limit, and has been shown to reproduce the known shear-thinning behaviour of hard spheres qualitatively, and shows the same kind of boundary-layer behaviour as theories based on more complete Smoluchowski equations [95].

This chapter is structured as follows. Firstly, we outline the heuristic percolation criterion of Alon, Balberg and Drory [74] that predicts the percolation threshold based only on the pair correlation function. Secondly, we give an overview of the Smoluchowski based theory of Blawzdziewicz and Szamel and its predictions for the pair correlation function of sheared particles. Thirdly, we combine the two theories into a single framework that predicts the percolation threshold in a sheared suspension. Throughout this chapter, we make comparisons with molecular dynamics simulation results to establish the validity of the made assumptions and to assess how they can be improved.

4.2 A heuristic percolation criterion

In this section, we describe the percolation criterion developed by Alon *et al.* [74], developed to predict the percolation threshold for anisometric particles based only on geometric structural input. In the presence of non-equilibrium flow fields, its geometric and heuristic nature is an advantage, since it is not rooted in equilibrium statistical mechanics. The model has been shown to give accurate results for permeable spheres, cubes, circles and squares, and does not lose its predictive power when polydispersity or attractive particle interactions are introduced [67].

We present the criterion specifically for monodisperse hard spheres. For a presentation applicable to particles that are anisometric, polydisperse in size or shape, or interact with different interparticle potentials, we refer to Refs. [67, 74]. We consider a dispersion of N spherical particles with diameter D that are impenetrable, *i.e.*, we assign an infinite energy to a configuration where any pair of particles overlap and zero energy otherwise. We disperse them homogeneously in a volume V, such that the macroscopic number density is $\rho = N/V$. The structure encoded in the pair correlation function $g(r)$ can be calculated accurately with the Ornstein-Zernike relation

in conjunction with the Percus-Yevick closure as described in Chapter 2. If the centre-to-centre distance of a pair of particles is smaller than the connectivity length λ, we call them directly connected.

Alon, Balberg and Drory postulate that the percolation threshold must be determined by two length scales. The first, l, is the average distance between directly connected particles (that is, particles with a mutual distance $< \lambda$). The second, L_2, is given by the average distance between particles that both have two or more direct connections. Such particles are seen as the backbones of a percolating cluster, since only by particles with two or more connections, connectivity can be propagated. All such particles have a mantle of directly connected neighbours around them that are on average a distance l away from each other. Alon *et al.* state that a percolating cluster exists if the mantles of such particles overlap. In other words, percolation threshold is determined by the condition $L_2 = 2l$, which is visualised in Fig. 4.1.

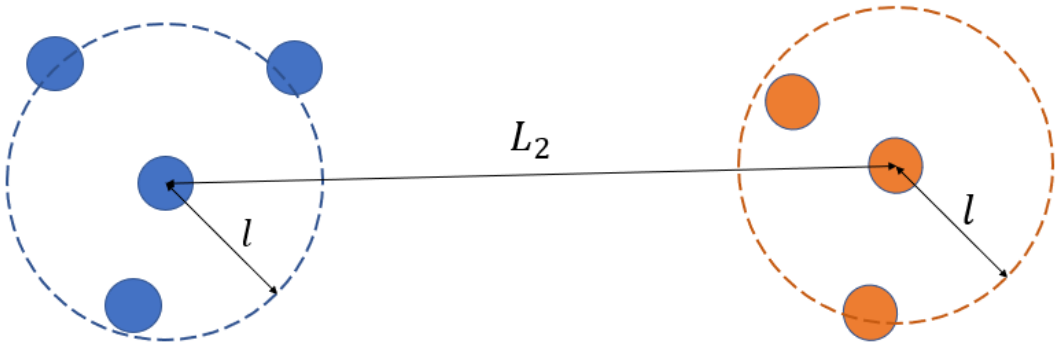

Figure 4.1: *Percolation is postulated to occur when the average nearest distance L_2 between a pair of particles with two or more connections is smaller than twice the average distance between directly connected particles, i.e., particles whose mutual distance is smaller that the connectivity length λ.*

To find the percolation threshold, we only need to calculate both the length scales and find at what density they are equal. We start by calculating the weighted distance l between two directly connected particles. Since the probability of finding a particle in a volume $\mathrm{d}^3\mathbf{r}$ at position $\mathbf{r}$ relative to a test particle is equal to $\rho g(\mathbf{r})\mathrm{d}^3\mathbf{r}$, we surmise that the mean squared distance reads

$$l^2 = \frac{\int_{V_\lambda} \mathrm{d}^3\mathbf{r} g(\mathbf{r}) r^2}{\int_{V_\lambda} \mathrm{d}^3\mathbf{r} g(\mathbf{r})}. \tag{4.1}$$

Here, we integrate over a so-called connectivity volume V_λ being the volume around a particle in which the centre of another particle can travel while remaining directly connected to the first. In our case of spherical connectivity volumes, we simply have $\int_{V_\lambda} \mathrm{d}^3\mathbf{r} = 4\pi \int_0^\lambda \mathrm{d}r\, r^2$. For the averaging, we use the second moment of the pair correlation function $g(|\mathbf{r}|)$ over the volume V_λ, instead of the first because it gives slightly better results, according to Alon and coworkers. It essentially gives the regions in the connectivity shell that are farther away a larger weight.

The second length scale L_2 is defined as the average closest distance between particles that each have two or more connections. To approximate this length scale, we assume that

the probability that a randomly chosen particle has k direct connections obeys the Poisson distribution $P_k = B^k \exp(-B)/k!$, where B is the average number of connections per particle. This assumption turns out to be exact if the particles are ideal [98, 99], and from our simulations we find it to be accurate for non-ideal particles too, see Fig. 4.2a. The effective density of particles that have at least two neighbours is now easily calculated

$$\rho_2 = \rho(1 - P_0 - P_1) \tag{4.2}$$
$$= \rho\left(1 - (1 + B)\exp(-B)\right). \tag{4.3}$$

The average volume per particle that has two or more neighbours is $1/\rho_2$. Assuming that this volume is spherical, Alon *et al.* find the average distance between particles with at least two neighbours to be $L_2 = 2(4\pi\rho_2/3)^{-1/3}$. The average number of neighbours B in the expression of ρ_2 can be evaluated from

$$B = \rho \int_{V_\lambda} \mathrm{d}^3\mathbf{r} g(\mathbf{r}) = 4\pi\rho \int_D^\lambda \mathrm{d}r^2 g(r). \tag{4.4}$$

The condition $2l = L_2$ is now an equation that depends only on the pair correlation function $g(r)$ and the number density ρ. In equilibrium, the pair correlation function can be calculated from liquid state theory as described in Chapter 2.

The logical path forward is therefore to combine the condition with the Ornstein-Zernike relation and the Percus-Yevick closure. Using Brent's root finding algorithm [100], we numerically solve this nonlinear set of equations to obtain the percolation threshold as function of D/λ. The result is presented in Fig. 4.2b, where we also plot our simulation results and the solution of the connectedness Ornstein-Zernike relation closed with the Percus-Yevick approximation. It is clear that this simple criterion outperforms this closure and is quantitative up to a few per cent.

With this simple percolation criterion, we can investigate the influence of a flow field on the percolation threshold with only the radial distribution function as input. Unfortunately, calculating this function for an arbitrary flow field is not straightforward. Therefore, we dedicate the next section to the method we use to obtain it in simple shear.

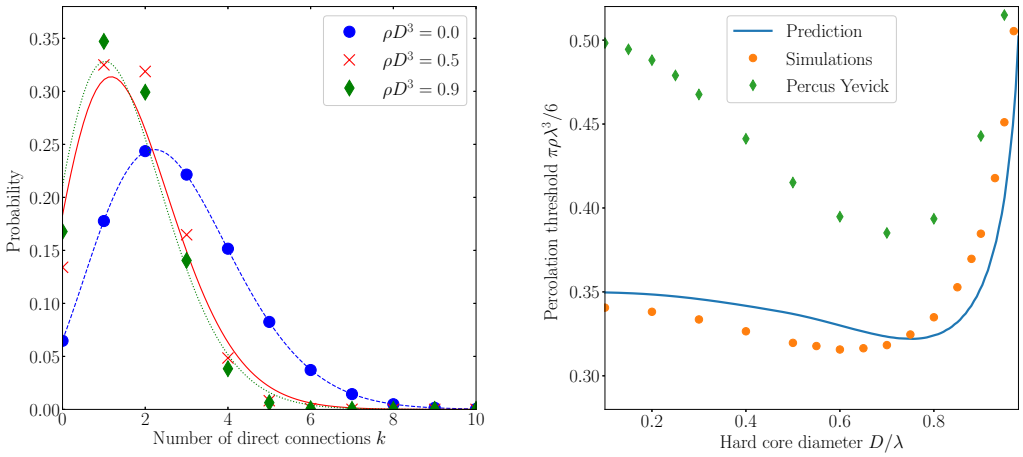

(a) **(b)**

Figure 4.2: *(a) Distribution of direct connections at the percolation threshold at several densities determined with our molecular dynamics simulations of hard spheres. The lines are the corresponding Poisson distributions. The figure shows that even at high densities, the number of connections are approximately Poisson distributed. (b) Percolation threshold as function of the hard-core diameter D scaled by the connectivity length λ of the particles. The line shows the prediction of the method of Alon et al., and the dots are Monte Carlo results due to Mark Miller. The predictions from liquid state theory with the Percus-Yevick closure from Chapter 2 are indicated by the diamonds.*

4.3 Pair correlation function

In this section, we focus on finding the pair correlation function of a colloidal dispersion of hard, spherical particles in a flow field. To simplify our analysis, we only consider simple shear flow, which we define by imposing the macroscopic velocity field $\mathbf{V} = \dot{\gamma} y \hat{\mathbf{x}}$, where $\dot{\gamma}$ is the shear rate. To simplify comparisons with our simulations and other works, we introduce a dimensionless parameter that quantifies to what degree particle transport occurs through the background velocity field relative to thermal particle diffusion. We identify this parameter as a Peclet number and define it as $\mathrm{Pe} = \dot{\gamma} D^2 / 4 D_0$. Here, D is the hard-core diameter of the particles as before, and D_0 is the self-diffusion constant, which by Stokes' law can be related to the solvent viscosity as we eluded to in Chapter 3. We have chosen to include a factor of 4 in the definition of the Peclet number because it is usually defined in terms of the hard-core radius of particles instead of the diameter.

We derive an approximation for the pair correlation function $g(\mathbf{r}, \mathrm{Pe})$ for a sheared dispersion from the many-body Smoluchowski equation. This equation describes the time-dependent N-body probability density function $P_N(\mathbf{r}_1, \ldots, \mathbf{r}_N, t)$ of interacting particles on Brownian time scales, and it can be derived from the Langevin equation (3.1) in the limit that the particles' inertia is subdominant to the viscous damping [101]. This limit is reached at timescales where the diffusive mean squared displacement of the particles is much larger than their inertial displacement, *i.e.*, if $t \gg 2mD_0/k_BT$. Here we have defined m as the particle mass and k_BT as the thermal

energy.

If we neglect all hydrodynamic interactions between the particles, we can write down this many-body Smoluchowski equation as [85]

$$\frac{\partial P_N}{\partial t} = \sum_{i=1}^{N} \nabla_i \cdot \left(D_0 \nabla_i P_N + D_0 \beta P_N \nabla_i \Psi - \dot{\gamma} y_i P_N \hat{\mathbf{x}} \right), \tag{4.5}$$

where $\beta = (k_B T)^{-1}$ is the inverse thermal energy, ∇_i is the gradient operator with respect to the ith particle position $\mathbf{r}_i$ ($i = 1, 2, \ldots, N$), and Ψ is the potential energy, which we assume to be pair-wise additive

$$\Psi(\mathbf{r}_1, \ldots, \mathbf{r}_N) = \sum_{i=1}^{N} \sum_{j>i}^{N} U(\mathbf{r}_i, \mathbf{r}_j). \tag{4.6}$$

Here $U(\mathbf{r}_i, \mathbf{r}_j)$ is the pair potential between particles i and j. For hard particles, $U(\mathbf{r}_1, \mathbf{r}_2) = \infty$ if the particles overlap and $U(\mathbf{r}_1, \mathbf{r}_2) = 0$ if they do not.

From the Smoluchowski equation (4.5), we can derive an equation for the pair correlation function by integrating over the positions of particles $3, \ldots, N$, because this integration results in an equation for the 1- and 2-body probability density functions P_1 and P_2 which can be related to the pair correlation function g as

$$g(\mathbf{r}_1, \mathbf{r}_2, t) = \frac{P_2(\mathbf{r}_1, \mathbf{r}_2, t)}{P_1(\mathbf{r}_1, t) P_1(\mathbf{r}_2, t)}, \tag{4.7}$$

where the 1- and 2-body probability density functions can be obtained from their N-body counterpart by integrating out the other particle positions

$$P_1(\mathbf{r}_1, t) = \int \mathrm{d}\mathbf{r}_2 \ldots \mathrm{d}\mathbf{r}_N P_N(\mathbf{r}_1, \ldots, \mathbf{r}_N, t); \tag{4.8}$$

$$P_2(\mathbf{r}_1, \mathbf{r}_2, t) = \int \mathrm{d}\mathbf{r}_3 \ldots \mathrm{d}\mathbf{r}_N P_N(\mathbf{r}_1, \ldots, \mathbf{r}_N, t). \tag{4.9}$$

In Eqs. (4.8) and (4.9), the integration ranges over all of three-dimensional space for each integrated particle position.

The full integration of the Smoluchowski equation over the coordinates $\mathbf{r}_i$ ($i = 3, 4, \ldots, N$) is slightly involved and its details are not crucial in order to understand the remainder of this chapter. Therefore, we present the results here and refer to Appendix A for the complete derivation. In the derivation, we have divided the pair correlation function in an equilibrium contribution $g_0(r)$ and a shear-induced perturbation $\delta g(\mathbf{r}, \mathrm{Pe})$, such that $g(\mathbf{r}, \mathrm{Pe}) = g_0(r) + \delta g(\mathbf{r}, \mathrm{Pe})$. The equilibrium pair correlation function $g_0(r)$ is only dependent on the radial coordinate and therefore is often referred to as the radial distribution function. Since equilibrium statistical mechanics provides an accurate theory for the equilibrium pair correlation function, as discussed in Chapter 2, we aim our focus mainly at the shear-induced perturbation. The integration of the Smoluchowski equation (4.5) results in a boundary value problem for this perturbation.

$$2D_0 \nabla^2 \delta g - \dot{\gamma} y \frac{\partial \delta g}{\partial x} = 0 \qquad r > D, \tag{4.10}$$

$$2D_0 \frac{\partial \delta g}{\partial r} - \dot{\gamma} \frac{xy}{r} \delta g = \dot{\gamma} \frac{xy}{r} \qquad r = D, \tag{4.11}$$

where we note that $\delta g = 0$ for $r < D$.

This boundary value problem is the starting point of the theory of Blawzdziewicz and Szamel [75]. To find an analytical solution, we use arguments similar to theirs, which were partly inspired by the work of Elrick [102]. The differential equation (4.10) essentially ensures conservation of mass, while the boundary condition (4.11) requires that there is no mass flux into excluded volume of the hard-core particles. In the derivation of this boundary-value problem from the Smoluchowski equation, several assumptions and approximations were made. We enumerate them below.

1. We assume that the pair-distribution function is stationary, that is, $\partial g/\partial t = 0$. This holds if the shear velocity field has been present for sufficiently long that the structure of the dispersion has had time to fully develop.
2. We assume that the macroscopic density is homogeneous. In this case, we can use $P_1(\mathbf{r}_1, t) = 1/V$, and $g(\mathbf{r}_1, \mathbf{r}_2) \equiv g(\mathbf{r}) = V^2 P_2(\mathbf{r}_1, \mathbf{r}_2)$, where we define $\mathbf{r} = |\mathbf{r}_2 - \mathbf{r}_1|$.
3. We assume that the particles only interact through additive pair interactions, see Eq. (4.6).
4. As already mentioned, we neglect all hydrodynamic interactions, that is, we neglect all interactions between particles that are mediated by the solvent. These include both short-ranged lubrication forces and long-ranged hydrodynamic many-body interactions. The validity of this approximation depends both on the volume fraction of the dispersion and on the shear rate. It is known that if either one of those parameters is large (*e.g.* $\varphi > 0.2$ or $\mathrm{Pe} > 10$), significant qualitative changes are seen in the structure of sheared dispersions due to the presence of these interactions [103, 104]. If both are low, however, the differences seem mainly of quantitative nature.
5. Eqs. (4.10) and (4.11) are derived in the dilute limit that the volume fraction $\varphi \to 0$. This means that we neglect all many-body correlations by disregarding the effect that particle crowding causes structural correlation apart from that caused by the pair potential itself. This approximation causes our theory to be invalid anywhere outside the very dilute regime, since we have seen in Chapter 2 that visible structural correlations start to occur at very low densities. In fact, with this approximation we implicitly assume that the equilibrium pair correlation function $g_0(\mathbf{r}) = \exp(-\beta U(\mathbf{r}_1, \mathbf{r}_2)) = \vartheta(|\mathbf{r}| - D)$, where $\vartheta(r)$ is the Heaviside step function. To extend the validity of our theory to higher densities, we re-introduce many-body correlations at a later stage in this chapter.

The last approximation removes all density dependence from the shear-induced perturbation of the pair correlation function. By comparison with molecular dynamics simulations, we test to what degree this is the case later this chapter.

We proceed by nondimensionalising Eqs. (4.10) and (4.11) by introducing new variables $\mathbf{r}' = (x', y', z')^T = \mathbf{r}\sqrt{\frac{\dot\gamma}{2D_0}}$ and $\delta g'(x', y', z') = \delta g(x, y, z)$, such that Eqs. (4.10) and (4.11) read

$$\nabla'^2 \delta g' - y' \frac{\partial \delta g'}{\partial x'} = 0 \qquad r' > \sqrt{2\mathrm{Pe}}, \tag{4.12}$$

$$\frac{\partial \delta g'}{\partial r'} - \frac{x'y'}{r'}\delta g' = \frac{x'y'}{r'} \qquad r' = \sqrt{2\mathrm{Pe}}. \tag{4.13}$$

The influence of the strength of the shear flow is now completely contained within the location of the boundary. To solve this boundary-value problem, we first find solutions to Eq. (4.12) in terms of Green's functions and then use a method similar to the method of images to satisfy the boundary condition (4.13). Because the full derivation of the solution might distract from our message, we present it in Appendix B, and simply state the result here.

The result of the boundary-value problem is given by the infinite linear combination of

functions $T'_{\alpha\beta}(\mathbf{r}')$:

$$\delta g'(\mathbf{r}') = \sum_{\alpha,\beta=0}^{\infty} C^{\alpha\beta} T'_{\alpha\beta}(\mathbf{r}') \qquad r' > \sqrt{2\mathrm{Pe}}, \tag{4.14}$$

in which $C^{\alpha\beta}$ are coefficients that are determined by the boundary condition. The functions $T'_{\alpha\beta}(\mathbf{r}')$ are given by

$$T'_{\alpha\beta}(x', y', z') = \tag{4.15}$$
$$\frac{1}{4}\int_0^\infty \mathrm{d}\tau \left(\frac{1}{\tau\pi}\right)^{3/2} \sqrt{\frac{3}{\tau^2+12}} \left(\frac{\partial}{\partial x'}\right)^\alpha \left(\frac{\partial}{\partial y'} + \tau\frac{\partial}{\partial x'}\right)^\beta \exp\left(-\frac{y'^2}{4\tau} - \frac{z'^2}{4\tau} - \frac{3(2x'-y'\tau)^2}{4\tau(\tau^2+12)}\right).$$

We find the coefficients $C^{\alpha\beta}$ by expanding the boundary condition in terms of spherical harmonics. To do this, we first insert $T'_{\alpha\beta}(\mathbf{r}')$ into the right-hand side of the boundary value (4.13) and subsequently write the result as a linear combination of real-valued spherical harmonics $Y_{lm}(\hat{\mathbf{r}}')$ with coefficients $j^{lm}_{\alpha\beta}$ for each α and β.

$$\frac{\partial T'_{\alpha\beta}}{\partial r'} - \frac{x'y'}{r'} T'_{\alpha\beta} = \sum_{l=0}^{\infty}\sum_{m=-l}^{l} j^{lm}_{\alpha\beta} Y_{lm}(\hat{\mathbf{r}}'). \tag{4.16}$$

Here, the real spherical harmonics are defined in terms of the regular spherical harmonics $\hat{Y}^m_l(\hat{\mathbf{r}}')$ as

$$Y_{lm} = \begin{cases} \frac{i}{\sqrt{2}}\left(\hat{Y}^m_l - (-1)^m \hat{Y}^{-m}_l\right) = \sqrt{2}(-1)^m \mathrm{Im}\left(\hat{Y}^{|m|}_l\right) & m < 0 \\ Y^0_l & m = 0 \\ \frac{1}{\sqrt{2}}\left(\hat{Y}^{-m}_l + (-1)^m \hat{Y}^m_l\right) = \sqrt{2}(-1)^m \mathrm{Re}\left(\hat{Y}^{|m|}_l\right) & m > 0. \end{cases} \tag{4.17}$$

Each coefficient $j^{lm}_{\alpha\beta}$ can be determined by multiplying both sides of Eq. (4.16) with the corresponding real spherical harmonic and integrating over the entire boundary, that is, the surface of the sphere with $r' = \sqrt{2\mathrm{Pe}}$. Due to the orthogonality of the real spherical harmonics, this yields the expansion coefficients

$$j^{lm}_{\alpha\beta} = \int_0^{2\pi} \mathrm{d}\phi' \int_0^{\pi} \mathrm{d}\theta' \sin(\theta') Y^{lm}(\theta', \phi') \left(\frac{\partial T'_{\alpha\beta}}{\partial r'} - \frac{x'y'}{r'} T'_{\alpha\beta}\right). \tag{4.18}$$

Using the fact that $x'y'/r'^2 = \sqrt{4\pi/15}\, Y_{2,\text{-}2}(\hat{\mathbf{r}}')$, we now write the full boundary condition (4.13) as

$$\sum_{\alpha,\beta=0}^{\infty} C^{\alpha\beta} \sum_{l=0}^{\infty}\sum_{m=-l}^{l} j^{lm}_{\alpha\beta} Y_{lm}(\hat{\mathbf{r}}') = \sqrt{\frac{8\pi\mathrm{Pe}}{15}}\, Y_{2,\text{-}2}(\hat{\mathbf{r}}') \qquad r' = \sqrt{2\mathrm{Pe}}, \tag{4.19}$$

or, more compactly,

$$\sum_{\alpha,\beta=0}^{\infty} C^{\alpha\beta} j^{lm}_{\alpha\beta} = \sqrt{\frac{8\pi\mathrm{Pe}}{15}} \delta_{l,2}\delta_{m,\text{-}2}, \tag{4.20}$$

for all integers $0 \leq l < \infty$ and $-l \leq m \leq l$, again due to the orthogonality of the real spherical harmonics. Eq. (4.20) is a system of infinitely many linear equations in the coefficients $C^{\alpha\beta}$.

To summarise, we have expressed the solution of the boundary value problem constituted by Eqs. (4.12) and (4.13) as an infinite linear combination of the functions $T_{\alpha\beta}(\mathbf{r}')$ with coefficients $C^{\alpha\beta}$, which in turn can be expressed as the solution of an infinite system of linear equations

with coefficients $j_{\alpha\beta}^{lm}$. The latter coefficients can be calculated with Eq. (4.18). The solution as presented above have a slightly different form than those presented by Blawzdziewicz *et al.* The reason for this difference probably stems from a different choice of dimensionless variables.

To make headway, we proceed by solving the linear system of Eq. (4.20) numerically, truncating all terms for which $\alpha+\beta > l_{\max}$ and all equations for which $l > l_{\max}$. As we know that $-l \leq m \leq l$ by the definition of the spherical harmonics, and that $j_{\alpha\beta}^{lm} = 0$ if $l-m$ is odd (the corresponding real spherical harmonics are not even in z, which they have to be in our expansion since our boundary value problem is), we are left with a square system of real-valued linear equations that is easily solved. We also numerically perform the integrations given in Eqs. (4.18) and (4.15) respectively using a Lebedev quadrature and Simpson's rule [55, 105]. In Appendix F, we describe the numerical procedure in more detail.

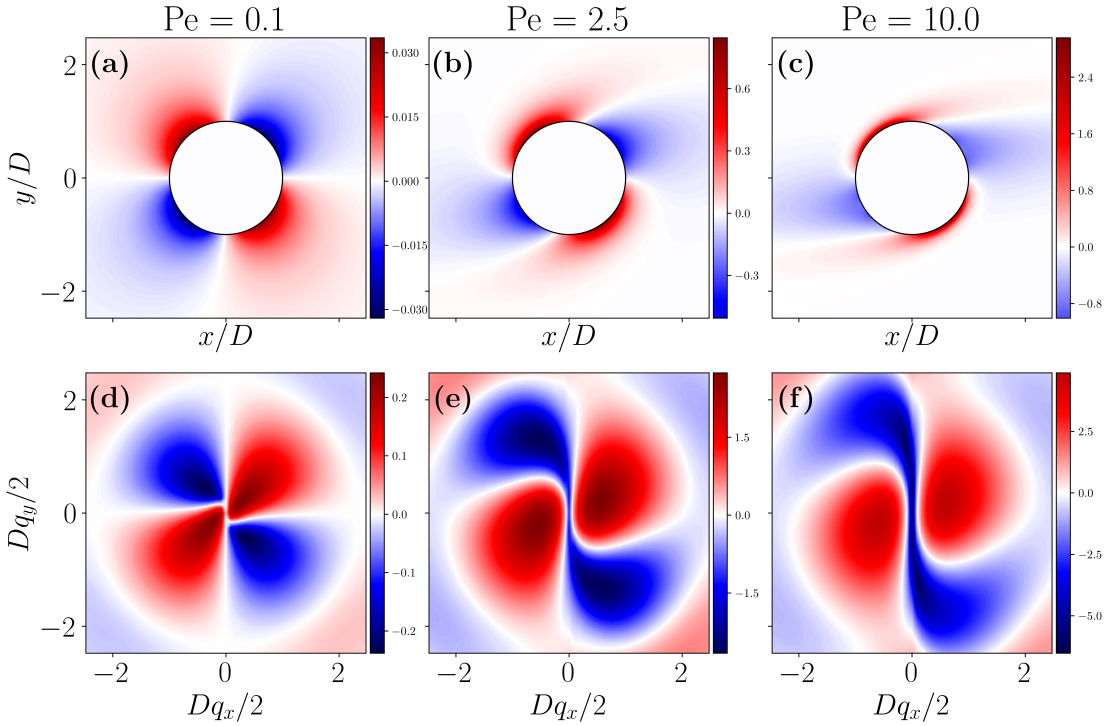

Figure 4.3: *The influence of a simple shear flow in the xy-plane on the radial distribution function of hard, spherical particles. In Figs. (a), (b), and (c) we show the function* $\delta g(\boldsymbol{r}, \mathrm{Pe}) = g(\boldsymbol{r}, \mathrm{Pe}) - g(r, 0)$ *for* $\mathrm{Pe} = 0.1$, 2.5, *and* 10.0. *In (d), (e), and (f), we show the influence of simple shear with the same shear rates on the perturbation of the structure factor* $(S(\boldsymbol{q}, \mathrm{Pe}) - S(q, 0))/\varphi$, *where* φ *is the hard-core volume fraction of the dispersion and* $S(\boldsymbol{q}, \mathrm{Pe})$ *is the static structure factor where the flow field is quantified by the Peclet number* Pe.

The results that follow a truncation given by $l_{\max} = 10$ are visualised in Fig. 4.3. In the literature, the results are often presented in terms of the perturbation of the structure factor $S(\mathbf{q}, \mathrm{Pe}) = 1 + \rho \int \mathrm{d}\mathbf{r} (g(\mathbf{r}, \mathrm{Pe}) - 1) \exp(i\mathbf{r}\cdot\mathbf{q})$, because this quantity can be measured experimentally with scattering experiments. Therefore, we also present the perturbation of the structure factor $S(\mathbf{q}, \mathrm{Pe}) - S(q, 0)$, which might aid in comparing with literature. The results from our numerical procedure are visually indistinguishable from those by Blawzdziewicz and Szamel.

We see that for all Peclet numbers, the perturbation in the structure respects the inversion

symmetry of the boundary value problem (4.10) and (4.11). In addition, we observe that for low Peclet numbers, the compressional ($xy < 0$) and extensional quadrants ($xy > 0$) of δg are very similar in shape, but different in sign. This indicates that positive and negative fluctuations in the pair correlation function are diffusively dissipated in a similar way, as long as they are small. When they become larger, as the Peclet number increases, this symmetry is broken, and a boundary layer is formed in the compressional quadrant, whereas a low-density 'wake' is formed in the extensional quadrant, in which the pair correlation function can be close to zero for high Peclet numbers.

The presence of this long wake induces a negative boundary layer in the low $\mathbf{q}$ structure factor. Dhont showed that the width of this boundary layer scales with $\mathrm{Pe}^{1/2}$ and that its presence causes the structure factor to be non-analytic in Pe, that is, for small Pe

$$S(\mathbf{q}, \mathrm{Pe}) \neq S_0(\mathbf{q}) + \mathrm{Pe}S_1(\mathbf{q}) + \mathrm{Pe}^2 S_2(\mathbf{q}) + \mathrm{Pe}^3 S_3(\mathbf{q}) + \ldots, \tag{4.21}$$

for any set of functions $S_i(\mathbf{q})$ [95].

In the work on the analytical method presented by Blawzdziewicz and Szamel [75] that we use here, a detailed comparison is made with the similar analytical theories of Dhont [95], Schwarzl and Hess [92], and Ronis [106]. Additionally, Blawzdziewicz and Szamel show that this method qualitatively reproduces the shear thinning behaviour that was found in experiments for this type of particle. In the remainder of this work, we set $l_{\max} = 10$, because the inclusion of more terms in the expansion does not visually change the results up to Pe, but does cause the method to become computationally expensive. Blawzdziewicz and Szamel also state that this cut-off leads to sufficiently converged results.

4.4 Comparison with simulation data

We now have an approximation of the pair correlation function, which is the only quantity required as input for our percolation criterion. Nothing now restrains us from calculating the percolation threshold for colloidal suspensions in shear flow. However, before we do so, we think it is important to first establish to what extend our theoretical prediction of the pair correlation function compares to simulations. In other words, we want to make sure that this theory gives accurate results such that we can correctly interpret the obtained percolation threshold at a later stage. To that end, we perform Langevin dynamics simulations along the lines as described in Chapter 3.

In Chapter 3, we have performed all simulations with the standard Weeks-Chandler-Andersen potential. This potential is introduced because when simulated, it gives results for macroscopic material properties that are accurate up to the high density regime [107]. However, slight deviations might occur at lower densities in the microscopic structure. To simplify the comparison between the theoretical and simulation results, we therefore slightly adapt the potential to better model hard spheres by rescaling the potential by a constant ϵ_0. The new potential is given by

$$U_{\mathrm{WCA}}(r) = \begin{cases} 4\epsilon_0\epsilon\left(\left(\frac{\sigma}{r}\right)^{12} - \left(\frac{\sigma}{r}\right)^{6}\right) + \epsilon_0\epsilon, & r < 2^{1/6}\sigma \\ 0, & r \geq 2^{1/6}\sigma. \end{cases} \tag{4.22}$$

In the rest of this chapter, we set $\epsilon_0 = 100$, $\epsilon = 1k_BT$ and $D = 2^{1/6}\sigma$. We visualise this change in the pair-potentials in Fig. 4.4. We stress that the difference between a Weeks-Chandler-Andersen potential with $\epsilon_0 = 1$ and $\epsilon_0 = 100$ is unlikely to result in large changes to macroscopic material properties, including the percolation threshold. This potential was merely chosen to be able to eliminate the soft characteristics in the microstructure.

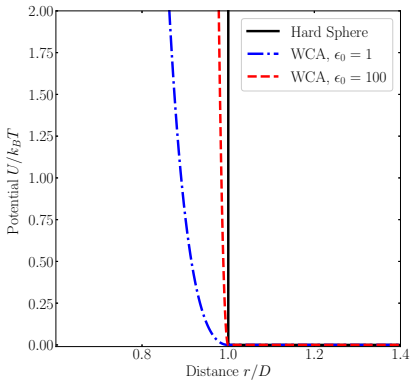

Figure 4.4: *The figure shows the pair potentials we use in this work as function of the particle distance. The analytical theory of this chapter is based on a hard-sphere potential of which we compare the results to the results of simulations of particles interacting with a Weeks-Chandler-Andersen potential with* $\epsilon_0 = 100$.

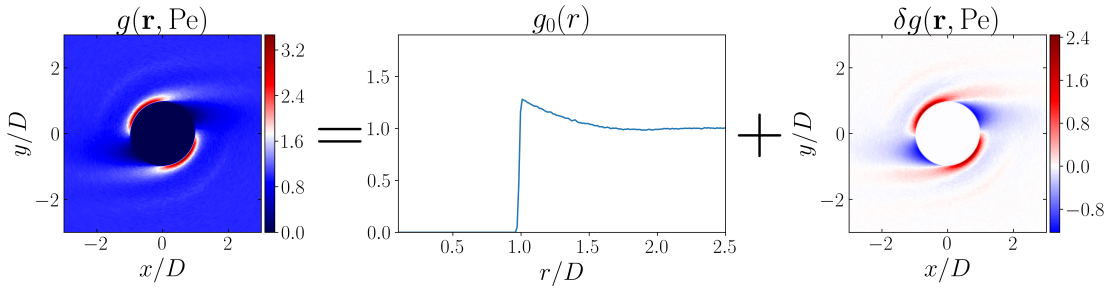

Figure 4.5: *The pair correlation function* $g(\boldsymbol{r}, \mathrm{Pe})$*, equilibrium pair correlation function* $g_0(r)$ *and its perturbation* $\delta g(\boldsymbol{r}, \mathrm{Pe})$ *of a dispersion of hard particles in a shear flow, obtained with Langevin dynamics simulations, discussed in Chapter 3. The pair correlation function* $g(\boldsymbol{r}, \mathrm{Pe})$ *was obtained from a simulation at a volume fraction* $\varphi = 0.1$ *at Peclet number* $\mathrm{Pe} = \dot{\gamma}D^2/4D_0 = 10.1$*, and* $g_0(r)$ *was obtained from a simulation at* $\mathrm{Pe} = 0$ *at the same volume fraction. The perturbation* $\delta g(\boldsymbol{r}, \mathrm{Pe})$ *is calculated by taking the difference of the two.*

In order to find the perturbation of the pair distribution function in our simulations, we perform three simulations. Firstly, we perform a simulation in the absence of flow in very dilute conditions ($\varphi \approx 10^{-4}$) to obtain the free-particle diffusion constant D_0 by measuring the mean squared displacement $\left\langle (\mathbf{r}(t) - \mathbf{r}(0))^2 \right\rangle = 6D_0 t$ and calculating its slope. The result never differs more than 2% from Einstein's theoretical prediction of $D_0 = k_B T/\gamma$. To obtain the equilibrium pair correlation function $g_0(r)$, we perform a simulation in the absence of a flow field at some volume fraction φ. To find the shear-dependent pair correlation function $g(\mathbf{r}, \mathrm{Pe})$, we subsequently perform a simulation at the same volume fraction with the flow field turned on at shear rate $\dot{\gamma}$ with corresponding Peclet number $\mathrm{Pe} = \dot{\gamma}D^2/4D_0$. In the last expression, we use the diffusion constant D_0 from the dilute equilibrium simulation, and we check whether the imposed shear rate $\dot{\gamma}$ matches the resulting velocity profile in the sheared simulation. The perturbation of the

pair correlation function is again defined by $\delta g(\mathbf{r}, \mathrm{Pe}) = g(\mathbf{r}, \mathrm{Pe}) - g_0(r)$. An example of the three functions in that expression from a typical simulation is given in Fig. 4.5.

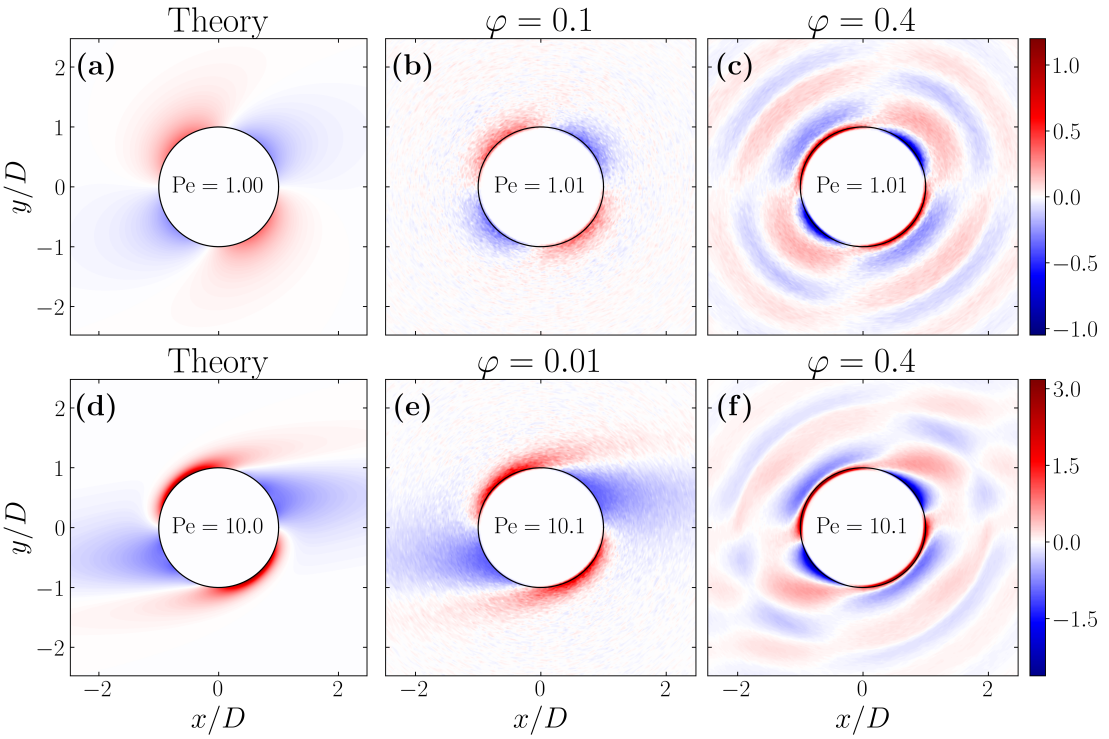

Figure 4.6: *Comparison between theory and simulations of the shear-induced perturbation of the pair-correlation function $\delta g(\boldsymbol{r}, \mathrm{Pe})$ at low and high volume fractions of hard, spherical particles in the flow-gradient plane. The figures in the first column (a, d) correspond to the theoretical model, whereas the second (b, e) and third (c, f) column correspond to low and high volume fractions φ. The first row (a-c) represents dispersions at Peclet number $\mathrm{Pe} \approx 1$, and for the second $\mathrm{Pe} \approx 10$. Each row shares a colour bar that indicates the values of $\delta g(\boldsymbol{r}, \mathrm{Pe})$. For clarity, we added a thin black line at $r = D$ indicating the theoretical excluded volume of hard, spherical particles. Note that both dilute simulations were not conducted at the same density. For the low-Peclet case, we set $\varphi = 0.1$, whereas we choose $\varphi = 0.01$ for the high-Peclet case.*

In this Fig. 4.5, we see that the perturbation $\delta g(\mathbf{r}, \mathrm{Pe})$ has qualitatively the same features as the theoretical model in Fig. 4.3c. That is, we see a boundary layer developing in the compressional quadrant, and a wake in the extensional quadrant. However, the observant reader might also notice a qualitative difference between the theoretical and simulation data. It seems that a second-order peak in the pair correlation function is now present, whereas it is not in the equilibrium function $g_0(r)$. This indicates that the presence of shear flow induces a local density increase near the boundary in the compressional quadrant, which might suggest that shear-induced chain-formation is taking place as observed in experiments [78, 79]. This phenomenon is not present in the theory presented in Fig. 4.3c, since the theoretical model is derived with the assumption that three-body correlations are negligible. The latter difference is also visible in the equilibrium pair correlation function, which distinctly deviates from a step function. In the next section, where we use the pair correlation function to calculate the percolation threshold, we

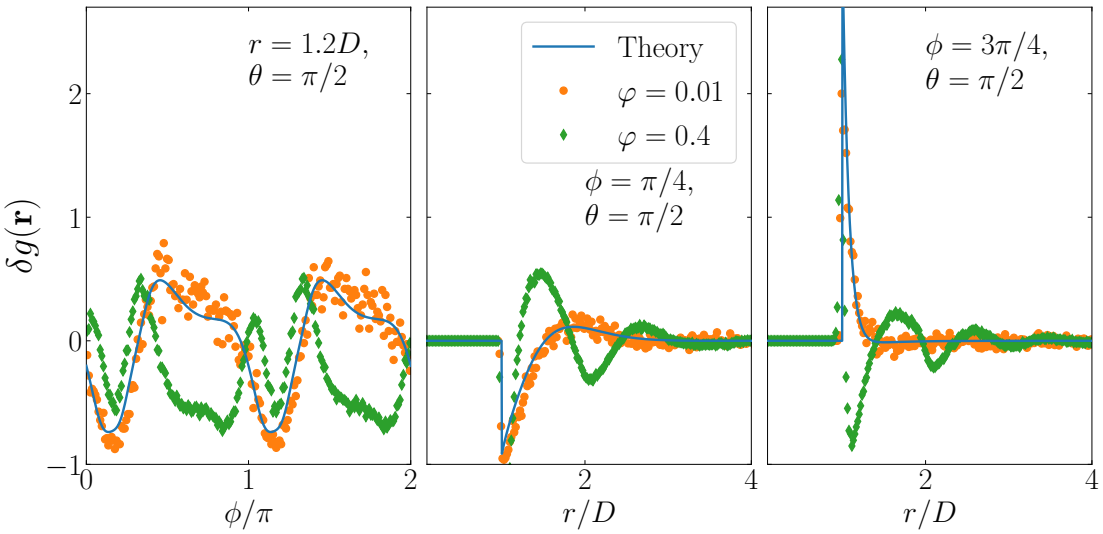

Figure 4.7: *Shear-induced perturbation of the pair-correlation function* $\delta g(\boldsymbol{r}, \mathrm{Pe})$ *of spherical particles along three different curves in the flow-gradient plane according to the theory and to simulations at volume fraction* $\varphi = 0.01$ *and* $\varphi = 0.4$ *for Peclet number* $\mathrm{Pe} = 10$. *Figure (a), (b) and (c) correspond to the perturbation at constant radial distance if* $r = 1.2D$, *and along the curves* $\boldsymbol{r} = r(\hat{\boldsymbol{x}} + \hat{\boldsymbol{y}})/\sqrt{2}$, *and* $\boldsymbol{r} = r(-\hat{\boldsymbol{x}} + \hat{\boldsymbol{y}})/\sqrt{2}$ *respectively.*

make a correction for this discrepancy.

To make a more comprehensive comparison between theoretical and simulation results, we present Figs. 4.6 and 4.7. In Fig. 4.6 we show the shear-induced perturbation in the xy-plane for two different Peclet numbers in a low- and high-density simulation. We see that at a low volume fraction φ, the results qualitatively match the theoretical model excellently, at least up to $\mathrm{Pe} = 10$. In the high-density case, however, we find that the many-body interactions induce highly complex correlations, which are qualitatively different from the behaviour that our theoretical model captures. Such correlations are also present in the equilibrium pair correlation function at this density. However, the perturbation of the shear-flow on these structural correlations is a nontrivial one. At low Peclet numbers, we see that the peaks of the equilibrium pair correlation function are either enlarged or suppressed depending in the compressional and extensional quadrant respectively. The opposite happens with the troughs. This means that in the compressional quadrant, the flow increases the amount of structural correlations, whereas the opposite happens in the extensional quadrant. If the strength of the shear flow is increased, this behaviour persists in the compressional quadrant but deforms in the extensional quadrant creating interesting structural patterns.

A more quantitative comparison is made in Fig. 4.7, where we plot the same data presented in Fig. 4.6d–f along the curves characterised by $r = 1.2D$, $\phi = \pi/4$ and $\phi = 3\pi/4$ all lying in the xy-plane, where we define θ, and ϕ as the polar and azimuthal coordinate. The figure shows that the theoretical model slightly underestimates the shear-induced perturbation at very low volume fractions. This slight discrepancy might be induced by a number of factors, such as numerical discretisation errors or non-convergence of Eq. (4.20) for $l_{\max} = 10$. Additionally, it might be induced by simulation inaccuracies such as finite time-stepping or the slight failure of the pair potential to represent a true hard sphere potential. The combined effect of the latter two explanations can also be seen at the particle boundary in the compressional quadrant in

Fig. 4.6, where it is visible that other particles are able to non-physically penetrate the $r < D$ region slightly. At high volume fractions we again see that the theoretical model qualitatively fails to predict the high-density features of $\delta g(\mathbf{r}, \mathrm{Pe})$. In fact, we see the emergence of a new peak in the perturbation of the pair correlation function at constant radius (leftmost plot). In the constant-angle plots (middle and right), we primarily see a large increase in the structural correlations for high densities, which is to be expected.

We have shown that we have obtained an approximation of the shear-induced perturbation of the pair-correlation function that is quantitative at low densities. In this work, we make no attempt at improving this approximations for many order correlations, since we believe that the current theory is sufficient to capture the qualitative behaviour of the percolation threshold of sheared dispersions, at least as long as the percolation threshold is located at low hard-core volume fractions, which is the case if the hard-core diameter D is sufficiently small compared to the connectivity length λ.

To proceed, we use the theory of this section in the next section in conjunction with the heuristic presented in Section 4.2 to approximate the percolation threshold.

4.5 Percolation threshold

Since we are in possession of a geometric criterion to find the percolation threshold that requires only a pair correlation function as input, and of an estimate for the effect that simple shear exerts on that pair correlation function, we can now combine the two models to find the influence of a flow field on the percolation threshold, which is our primary goal.

In the previous section, we evaluate the pair correlation function as the sum of its equilibrium value and a distortion, the former of which we approximate by $g_0(r) = \exp(-\beta U(r))$, with $U(r)$ the hard-sphere interaction potential. In doing so, we have removed all density dependence from the pair correlation function $g(\mathbf{r}, \mathrm{Pe})$, which is only valid if the volume fraction $\varphi \ll 1$. To extend the validity of our model, we re-introduce the density dependence in the pair correlation function in an *ad hoc* fashion by approximating the equilibrium contribution with the solution of the Ornstein-Zernike equation closed with the Percus-Yevick approximation that we describe in Section 2.3. The resulting pair correlation function is now the sum of an accurate equilibrium term and a low-density shear-induced perturbation.

We now numerically integrate the pair correlation function over the connectivity shell to find an approximation of the two implicitly density dependent length scales l and L_2 as they are defined in Section 4.2. We subsequently use Brent's root finding method to find the density that satisfies $2l = L_2$ for a given ratio D/λ.

In Fig. 4.8a, we present our results on the effect of shear flow on the percolation threshold according to our model. We compare them to simulation results plotted in Fig. 4.8b. If the hard-core diameter D goes to zero and particle interactions become negligible, we find that the effect of the shear flow on the percolation threshold is almost non-existent. This is to be expected, of course, since the flow field does not induce any structural changes if the particles do not interact, *i.e.*, if $D = 0$. In the intermediate and high D/λ regime, the results show that an applied shear flow can both increase and decrease the percolation threshold of a material depending on the hard-core size and strength of the flow field.

We conjecture that the shear-induced decrease of the percolation threshold is closely related to the emergence of shear-induced contact clusters [82–84]. Even at volume fractions where such clusters are finite, they might play a significant role in aiding long-range connectivity and therefore in decreasing the percolation threshold with respect to the equilibrium situation.

Fig. 4.8 indicates that there is good qualitative agreement between our theoretical model

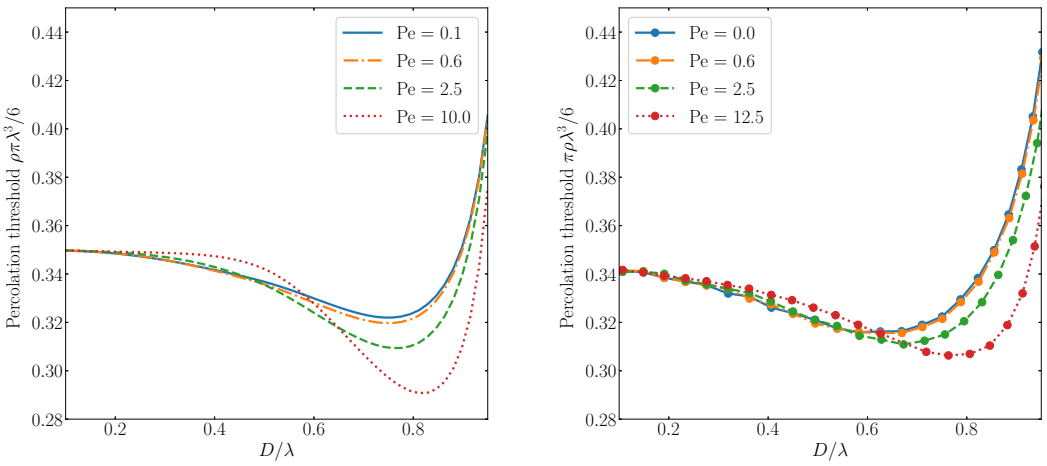

(a) **(b)**

Figure 4.8: *Theoretical (a) and simulation (b) results of the dimensionless percolation threshold of a dispersion of hard spherical particles subject to a simple shear flow as function of the ratio of the hard core diameter D and connectivity length λ. The strength of the shear flow is quantified with the Peclet number* Pe. *The lines in (b) are guides to the eye. Note that the set of Peclet numbers is not exactly equal in both figures.*

and simulation results of the percolation threshold. Our model correctly predicts the shear flow to induce an increase and subsequent decrease of the percolation threshold and gives an accurate approximation of the location of the cross-over between these two regimes. Quantitatively, our theory seems to overestimate the effect of the shear flow on the percolation threshold especially at high D/λ, where the hard core volume fraction is high and the shear flow significantly affects many body correlations as we show in Fig. 4.6.

We stress that we neglect all hydrodynamic interactions in both the theory and simulations, without providing any justification for this simplification. Therefore, we do not expect that either our theory or simulation results provide quantitative agreements with experiments. However, since hydrodynamical interactions have been shown to not qualitatively change the structure of sheared dispersions at sufficiently low densities, we expect our results to qualitatively hold even if hydrodynamical interactions are properly included.

In order to find an indication to what extend clusters are elongated due to the shear flow, we calculate the gyration tensor for each cluster in a molecular dynamics simulation, and average over all clusters and 10^3 independent particle configurations. Given that we have particle positions $\mathbf{r}_j$ that all belong to the same cluster, where $j = 1, \ldots, k$ and k is the number of particles in that cluster, we can define the gyration tensor in the form of a matrix reading

$$\mathbf{S} = \frac{1}{k}\sum_{j=1}^{k}(\mathbf{r}_j - \mathbf{R})(\mathbf{r}_j - \mathbf{R})^T, \tag{4.23}$$

where $\mathbf{R}$ is the centre of mass position of the cluster. Since most clusters contain only one particle, giving $\mathbf{S} = \mathbf{0}$, it is useful to take the weight average instead of the normal number average of $\mathbf{S}$ to

give more significance to larger clusters and to get better statistics.

The eigenvalues and -vectors of the resulting mean gyration tensor give information about the shape of the average cluster [108]. The eigenvectors lie along the principal axes of the clusters and the eigenvalues give the corresponding moments. In Fig. 4.9a we plot the eigenvalues as a function of the Peclet number below the percolation threshold at volume fraction $\varphi = 0.16$ and $D/\lambda = 0.82$. We label the eigenvalues such that $\lambda_3 > \lambda_2 > \lambda_1$. We find that the eigenvector corresponding to λ_2 always lies along the z-axis, whereas the remaining two eigenvectors always lie in the xy-plane. In Fig. 4.9a we see that the clusters grow when the strength of the shear flow increases. Interestingly, we also see that the smallest eigenvalue is largely unaffected by the flow field for this particular choice of parameters. Additionally, the flow field causes the clusters to become triaxial, that is, their sizes are notably different along their three principal axes.

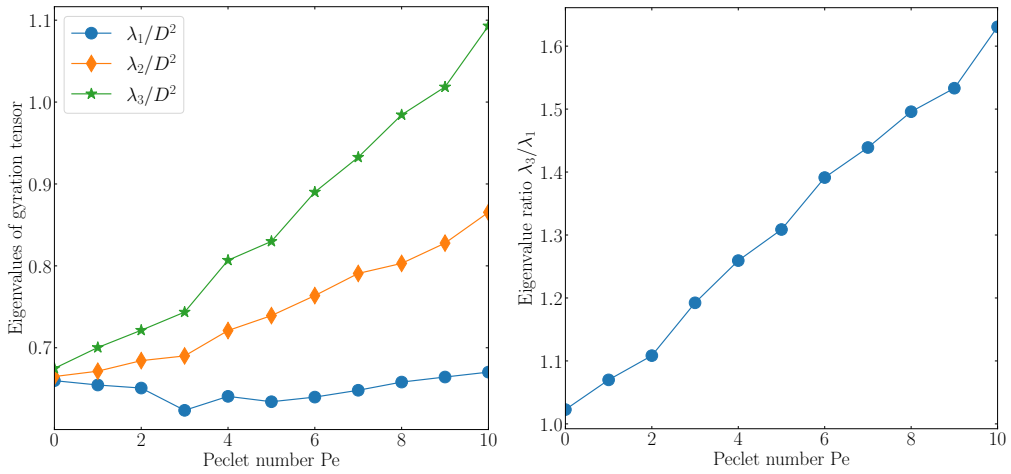

(a) **(b)**

Figure 4.9: *(a) Eigenvalues and (b) ratio of largest and smallest eigenvalue of the mean gyration tensor of particle clusters as a function of the strength of the shear flow. The eigenvalues were obtained by calculating the gyration tensor averaged over each cluster in a simulation of* $N = 1000$ *particles below the percolation threshold at connectivity volume fraction* $\pi\rho\lambda^3/6 = 0.30$ *and* $D/\lambda = 0.82$*. The corresponding hard-core volume fraction is* $\varphi = 0.16$*.*

In Fig. 4.9b, we plot the ratio of the largest and smallest eigenvalue as a function of the Peclet number. This ratio is a measure of the anisometry of the particles and it seems to increase linearly with the Peclet number in this regime. Due to a lack of time, we have not been able to perform a more comprehensive study of how this anisometry behaves throughout our parameter space. It remains to be seen whether the linear increase found for this particular set of parameters is characteristic of the shear-dependent cluster shape, or if more complex shear-induced elongation behaviour exists.

Our observation of these elongated clusters gives some, yet inconclusive, evidence for our conjecture that the shear-induced decrease of the percolation threshold is caused by the emergence linear contact clusters. We have not yet performed any other analysis to further substantiate this claim. Follow-up work shall therefore need to shed more light on this issue.

4.6 Discussion and conclusion

In this chapter, we have presented a model that gives a qualitatively accurate description of the percolation threshold of sheared suspensions of spherical particles in the absence of hydrodynamic interactions. The model is based on the conjunction of a heuristic percolation criterion presented by Alon, Balberg and Drory [74] and the theory for the shear-induced distortion of the pair correlation function by Blawzdziewicz and Szamel [75]. In order to test the validity of the two works, we have compared both independently with results of Langevin dynamics simulations as described in Chapter 3.

Alon, Balberg and Drory's percolation criterion is based on a purely geometric argument, applicable in out-of-equilibrium materials. It states that the percolation threshold is achieved if two length-scales are equal. This equality condition results in a nonlinear equation of the density that only requires the pair correlation function as external input. In accordance with earlier simulation studies [67, 74], we find that the heuristic percolation criterion gives accurate agreement with simulations for hard, spherical particles for all ratios of the hard-core diameter and the connectivity length.

Using the theory of Blawzdziewicz and Szamel, we provide the pair-correlation function that is required as input for the percolation heuristic. This work approximates the shear-induced perturbation of the dilute pair correlation function on the Smoluchowski equation at the two-particle level, neglecting all hydrodynamic interactions and influences of three-body correlations on this perturbation. We use this perturbation together with the equilibrium structure provided by standard liquid state theory (see Chapter 2) to find an approximation of the pair correlation function that is accurate up to the intermediate density regime, in which the coupling between many-body interactions and the imposed shear flow become non-negligible. We show by means of Langevin dynamics simulations that the theory for the perturbation of the pair correlation function in shear flow is very accurate in the dilute limit. However, as expected, significant deviations start to occur as the particle volume fraction increases.

Put together, the two theories provide a predictive framework for the percolation threshold in sheared suspensions that gives semiquantitative agreement with simulations of hard spherical particles. Both the theory and simulations indicate that shear flow can increase or decrease the percolation threshold depending on the hard-core diameter, connectivity range, and shear rate. We postulate that the decrease is due to the emergence of linear clusters of particles that aid long-range connectivity.

A decrease in the percolation threshold of suspensions due to shear-induced clusters has also been found in experiments. In particular, Schueler *et al.* have showed that they could engineer the percolation threshold of carbon black in a polymer resin to be as low as 0.06 vol% by using shear flow to induce particle aggregations with low fractal dimensions [109]. This stands in stark contrast to the 'equilibrium' percolation threshold of carbon black, which is roughly 0.2-0.3 vol%. Micrographs of the resulting structure show that material-spanning aggregations are formed that include a high fraction of the carbon black particles.

The heuristic framework presented in this chapter can in principle be adapted for anisometric particles. However, as the particle shape departs far from sphericity, the heuristic percolation criterion fails [67]. To model percolation of sheared dispersions of rods, for example, significant changes in the structure of this criterion are required. Additionally, the Smoluchowski equation should be adapted to account for the rotational diffusion of anisometric particles and the non-isotropy of the particle mobility.

Chapter 5

Percolation of hard nanorods in an external field

Summary

We present a numerical study on the continuum percolation of rodlike particles in the presence of orientational and disorientational quadrupolar fields. With this research, we aim to qualify the effects of externally applied axial and planar orientational order on the concentration at which percolating networks form. We perform a comprehensive analysis of the behaviour of the weight average number of particles in a cluster as function of the strength of the external field, the particle density, and particle aspect ratio, taking into explicit account the intrinsically induced order by excluded volume effects, including the concomitant low-density phase transitions. We find that these external quadrupolar fields can raise the percolation threshold substantially and cause exotic, nontrivial behaviour of the cluster size and shape.

5.1 Introduction

Because of the fact that the percolation threshold in homogeneous materials scales approximately inversely with the aspect ratio of network forming particles [27], it is especially beneficial from an engineering perspective to use highly anisotropic nanofillers. In this spirit, a large fraction of the physics literature on percolation is focused on describing networks and percolation behaviour of rodlike particles, both theoretically and experimentally. This is a challenging subject not only due to the phenomena mentioned in Chapter 1, but also due to the fact that rodlike particles spontaneously self-organise orientationally at low packing fractions. These phase transitions are hard to prevent because the particles undergo them driven fully by entropy [101, 110]. This implies that in order to investigate the influence of factors such as length polydispersity or dispersive inhomogeneity on the percolation threshold, one has to take the phase behaviour of long rodlike particles into careful consideration.

In addition to entropy-driven alignment, externally induced alignment is ubiquitous in real materials due to processes in their manufacturing such as shear strains and externally applied electromagnetic fields. Therefore, in order to comprehend the structure and percolation of highly anisotropic nanoparticles, we must understand the interplay between internal and external particle alignment.

Finner *et al.* have shown that such dispersions of rod-like particles in external orienting fields exhibit complex behaviour [111]: in the dilute limit, the particles cannot create material-spanning clusters. As one adds more particles, the average network grows, until its size diverges at the percolation threshold. At even higher densities, however, the alignment induced by the external field and excluded-volume interactions can suppress percolation. This is called re-entrance behaviour. To restore the percolating state, one could fruitfully choose to add even more particles, regaining system-spanning networks. However, testament to the nonlinearity of the interplay between the effects on the network size of the addition of particles and the induced alignment induced by those additional particles, percolation can again break down and form again at even higher densities. In summary, as the density increases monotonically and everything else remains constant, percolation can appear from a non-percolating state up to three times [111].

With the present work, we would like to extend Finner's numerical analysis of percolation in orientational fields, by also considering disorientational fields. Disorientational fields can exist both as external electromagnetic quadrupolar fields and as the flow field resulting from the uniaxial compression of the sample material. Additionally, one could conceivably model the confinement of nanorods between two walls as them being subject to a strong disorientational field in three dimensions.

The word 'disorientational' might be considered a misnomer. The difference between an orientational and a disorientational field is that the former pushes particles towards an axis whereas the latter pushes them away from an axis toward the plane perpendicular to that axis. Paradoxically, a disorientational field does induce order and can cause a phase transition from an unordered isotropic phase to an ordered liquid crystalline phase [112]. Furthermore, in rod-like dispersions subject to disorientational fields, a symmetry breaking can occur that is not seen in materials subjected to orientational fields. We try to clarify the physical reason behind this distinction below.

In a dispersion of rod-like particles subject to a small external orienting field, the particles align slightly along the field axis. If the density is increased, excluded volume effects can induce a phase transition from what is called the paranematic state to the nematic state, in which the particles are strongly aligned. The axis along which the particles are aligned, which is called the nematic director, is the same as the external field axis. The resulting orientational distribution therefore possesses azimuthal symmetry, see Fig. 5.1.

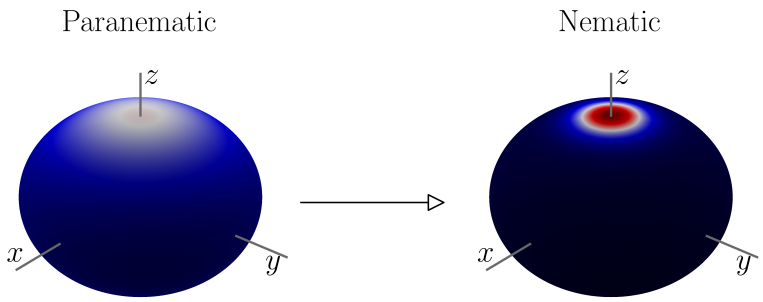

Figure 5.1: *Orientational distribution of rod-like particles subject to an orientational external field directed along the z-axis. The colour indicates the fraction of particles aligned in the corresponding direction with increasing probability density from blue to white to red. The figure shows the phase transition from a low-density paranematic state (left), to a high-density nematic state (right).*

In a dispersion of those same particles subject to a small disorientational field, however, the particles align away from the field axis. Now, if the particle density is increased, the same phase transition to a nematic state can occur. In this case, the nematic director always lies in the plane perpendicular to the field axis, see Fig. 5.2. Because of the fact that the external field and the excluded volume effects do not drive the particles in the same direction, the resulting nematic phase is biaxial, *i.e.*, it is no longer symmetric under rotations around the director. If the external disorienting field becomes infinitely strong, it forces all particles to be oriented in the xy-plane.

Finner's numerical work found partial disagreement with the results of an earlier analytical treatment of Otten *et al.* on the influence of externally induced particle alignment on the percolation threshold [113]. This is especially relevant because it is almost inevitable to introduce some sort of particle alignment during the manufacturing process, whether or not intentionally. For computational reasons, Finner *et al.* only considered external orientational fields and not disorientational case. In this chapter, we present a more comprehensive study on the effects of external quadrupolar fields on the percolation threshold.

In this chapter, we conduct an extensive numerical study on the properties and behaviour of rod-like particles subject to a quadrupole field; both orientational and disorientational. Thereby we extend earlier works, which either only consider orientational fields [111] as described above, or perform computations on a lattice [114], or do not take into account the excluded volume interactions between rods [115]. We investigate how the percolation threshold depends on the system parameters, *i.e.*, the particle concentration, external field strength, particle aspect ratio and a connectivity criterion that specifies particle connections. We also briefly investigate the shape of non-percolating clusters and its dependence on the underlying thermodynamic phase.

The remainder of this chapter is divided into three parts. Firstly, we devote a section on

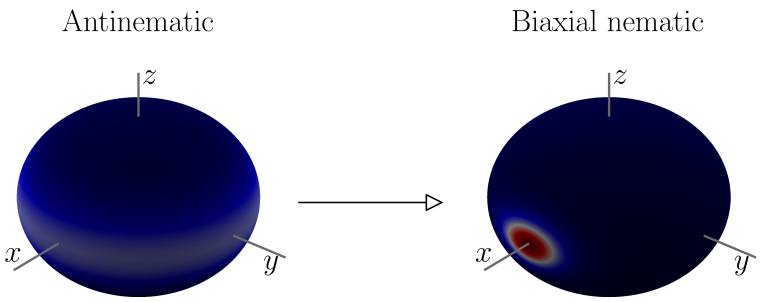

Figure 5.2: *Orientational distribution of rod-like particles subject to a disorientational external field which drives the particle orientations away from the z-axis. The colour indicates the fraction of the particles aligned in the corresponding direction with increasing probability density from blue to white to red. The figure shows the phase transition from a low-density antinematic state (left), to a high-density nematic state (right).*

Onsager theory, which allows us to find the orientational distribution function for particles and the locations of the relevant phase transitions in the limit of infinite aspect rations. Secondly, we apply continuum percolation theory to find when dispersions of those particles percolate. In the last section, we investigate the effect of the aspect ratio by extending the theory presented in the previous sections.

5.2 Onsager theory

A dispersion of impenetrable rod-like particles has been shown to undergo a transition from a isotropic phase to a nematic phase by Onsager in one of his seminal papers [116]. His treatise, which is believed to become exact in the limit of infinitely slender particles, is based on the balance of translational and orientational entropy. He shows that at sufficiently high concentrations, the particles must orient themselves along a common axis, called the nematic director, because this configuration allows for more translational freedom in the expense of rotational freedom, thereby increasing the total entropy. Onsager theory was shown to become quantitatively accurate if $L/D \gtrsim 100$ [117].

5.2.1 The orientational distribution function

In this work, we use Onsager's framework to find the particle orientational distribution function $\psi(\mathbf{u})$, where the orientation is given in spherical coordinates by $\mathbf{u} = (\sin\theta\cos\phi,\ \sin\theta\sin\phi,\ \cos\theta)^T$ with θ and ϕ the polar and azimuthal angle. We assume that the particles can be accurately modelled as spherocylinders having length L and diameter D. The particles are impenetrable, meaning that we assign an infinite energy to a configuration where any two particles overlap.

Apart from this excluded volume interaction, the particles do not interact. We introduce a dimensionless parameter $c = \pi\rho L^2 D/4$, which is equal to the product of the aspect ratio and the hard-core volume fraction in the slender-particle limit. Here $\rho = N/V$, is the macroscopic number density. The parameter c plays the role of the particle concentration in the rest of our work and we address it as such. However, note that any remark we make containing a phrase like "as the concentration increases" can also be interpreted to mean "as the particle aspect ratio increases".

We assume that the particles are subject to an external field of quadrupole type. This is the most natural external field to consider, since it respects the symmetries of the rod-like particles. We rotate our coordinate system such that the field axis coincides with the z-axis. This field assigns an energy to each particle given by

$$\frac{U}{k_B T} = -K \cos^2 \theta. \tag{5.1}$$

Here $k_B T$ is the thermal energy and K is the dimensionless field strength. If K is positive, the particles favour being aligned along the z-axis, and we call the field orientational. If K is negative, however, the particles prefer to be aligned in the xy-plane, and the field is called disorientational or planar.

Onsager showed that the free energy per particle in units of thermal energy can be written up to an arbitrary constant as

$$\frac{F}{N k_B T} = \ln c + \langle \ln \psi(\mathbf{u}) \rangle + \frac{4c}{\pi} \langle\langle |\mathbf{u} \times \mathbf{u}'| \rangle\rangle' - K \langle \cos^2 \theta \rangle. \tag{5.2}$$

In the above equation, we introduced a shorthand notation for the angular averaging operator $\langle \ldots \rangle \equiv \int \mathrm{d}\mathbf{u} (\ldots) \psi(\mathbf{u})$, where the integration runs over all orientations on the unit sphere[1]. The first term in the free energy corresponds to the translational entropy of an ideal gas, while the second accounts its orientational entropy. The third term describes the excluded volume interactions and essentially is a measure of the size of the average volume that is not available to a particle because of the other particles. The size of this volume is proportional to the average length of the cross product of the two particle orientations, or, more simply put, proportional to the average sine of the angle between two particle orientations. This product can be calculated explicitly in terms of the orientations of two particles with orientations $\mathbf{u}$ and $\mathbf{u}'$ to be

$$|\mathbf{u} \times \mathbf{u}'| = \sqrt{1 - (\cos\theta \cos\theta' + \sin\theta \sin\theta' \cos(\phi - \phi'))^2}. \tag{5.3}$$

The goal of Onsager theory is to find the equilibrium orientational distribution function $\psi(\mathbf{u})$, which quantifies how the particles are oriented in thermal equilibrium. An expression for the equilibrium orientational distribution function can be obtained by formally minimising the free energy with respect to $\psi(\mathbf{u})$ under the normalisation constraint that the orientational distribution must integrate to one. This yields the Onsager equation

$$\psi(\mathbf{u}) = \frac{1}{Z} \exp\left(K \cos^2 \theta - \frac{8c}{\pi} \langle |\mathbf{u} \times \mathbf{u}'| \rangle' \right), \tag{5.4}$$

where Z is a constant that ensures normalisation. Eq. (5.4) is a nonlinear integral equation for $\psi(\mathbf{u})$ due to its presence in the angular integral in the exponent. A successful method for approximating the solution of the Onsager equation, applied by Onsager himself for $K = 0$

[1] *Mutatis mutandis* for the primed variable.

and by Khoklov and Semenov for $K \neq 0$, consists of guessing the functional form of $\psi(\mathbf{u}; \{\alpha_i\})$, dependent on some combination of parameters $\{\alpha_i\}$ and then minimising the free energy (5.2) with respect to these parameters. However, numerical analysis has shown that some results from this procedure are quantitatively inaccurate [118, 119].

Therefore, we choose to solve this equation numerically with the method of recursive iteration: first we make a rough estimate of the function $\psi(\mathbf{u})$ and then use Eq. (5.4) to find a better approximation. We repeat this until the solution has converged. We treat the procedure as converged when the maximal difference between two subsequent iterations is smaller than 10^{-8}. In fact, it has been shown that this procedure is highly convergent when applied to the Onsager equation [120]. Typically, a numerically accurate solution is found after roughly 10–30 iterations. To approximate the integral, we use the Lebedev quadrature of order 131, yielding highly accurate approximations of integrals on the unit sphere. More information on this quadrature in given in Appendix F.1.

5.2.2 Order parameters and the phase diagram

Given the equilibrium orientational distribution function $\psi(\mathbf{u})$, we can quantify the amount of order in a dispersion of particles by looking at two order parameters. The first, $S_1 = (3\langle\cos^2\theta\rangle - 1)/2$, is the conventional nematic order parameter, which quantifies to what extend the rods are aligned along the z-axis (which coincides with the external field axis). This order parameter is unity if all particles are aligned along this axis, and vanishes if the particles are distributed isotropically. If all the particles are aligned in the xy-plane, we have $S_1 = -1/2$. Knowledge of S_1 can be used to identify if the particles are in the isotropic or nematic phase in the case of orienting fields ($K > 0$).

The second order parameter, $S_2 = \langle\cos(2\phi)\sin^2\theta\rangle$, quantifies to which extend the orientational distribution is asymmetric with respect to a rotation about the azimuthal axis and can be used to see if a phase transition has occurred in the case of disorienting fields. S_2 equals zero if the orientational distribution is symmetric with respect to rotations around the z-axis, and $S_2 = 1$ if all particles are oriented along the x-axis. In the case of disorientational fields, a nematic field could develop along all directors in the xy-plane because each of these directions is energetically equivalent. The result of the numeric recursive iteration therefore depends on our initial guess of the orientational distribution. We choose this initial guess such that, if the particles organise themselves in a nematic phase for $K < 0$, the resulting director always lies along the x-axis.

Figure 5.3 shows the density dependence of both order parameters for orientational and disorientational fields. For sufficiently strong orientational fields ($K = 1$ qualifies), we find that both order parameters increase continuously with concentration; there is no sharp transition between a slightly ordered and a very ordered liquid crystal. However, in the case of strong disorientational fields, $K = -2$ for example, the figure shows that such a transition exists: at some concentration the derivative of the order parameters is discontinuous. Khokhlov and Semenov found that this continuous phase transition occurs for arbitrarily strong disorientational fields and show that it occurs at $c = 3\pi^2/16 \approx 1.85$ for $K \to \infty$ [112].

Onsager found that for sufficiently small external fields, the particles can lower their free energy by separating into two phases, a low density unordered phase, and a high density ordered phase. To find the value of the densities of two coexisting phases, the common tangent method is often used. This method translates to the requirement that the two phases are in thermal equilibrium: the pressures and chemical potentials are equal in both phases.

The dimensionless pressure p and chemical potential μ can both be expressed in terms of the free energy F, whose value we can evaluate having already found the equilibrium $\psi(\mathbf{u})$,

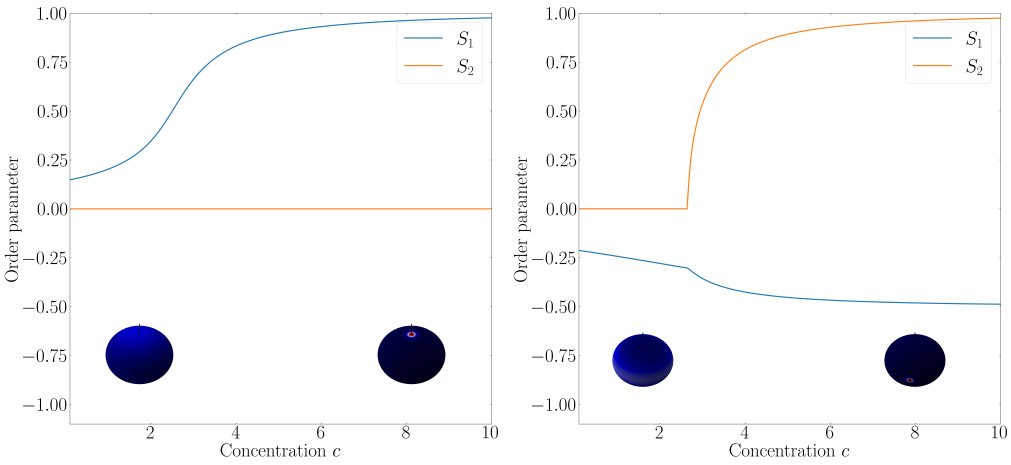

(a) $K = 1$ **(b)** $K = -2$

Figure 5.3: *The order parameters* $S_1 = (3\langle\cos^2\theta\rangle - 1)/2$ *and* $S_2 = \langle\cos(2\phi)\sin^2\theta\rangle$ *as function of concentration for (a) orienting fields and (b) disorienting fields. The insets show the orientational distribution function at the concentration corresponding to their locations. The colours used have the same meaning as in Fig. 5.1 and 5.2.*

as [101]

$$p = -\frac{c}{\rho k_B T}\left(\frac{\partial F}{\partial V}\right)_{N,T} = c^2\frac{\partial f}{\partial c} \qquad \text{and} \qquad \mu = \frac{1}{k_B T}\left(\frac{\partial F}{\partial N}\right)_{V,T} = f + p/c. \tag{5.5}$$

For a fixed field strength, we can solve the system of equations $p(c_1) = p(c_2)$ and $\mu(c_1) = \mu(c_2)$, where $c_1 \neq c_2$. The solutions are shown as function of K in Fig. 5.4. From this Figure, we can identify six phases. If the external field K is equal to zero, and the particle dispersion is sufficiently dilute, the orientational distribution function takes a constant value $\psi(\mathbf{u}) = 1/4\pi$, meaning that there is no order. This phase, which is not indicated in the figure, is called isotropic. In the isotropic phase, it is easy to show that $S_1 = S_2 = 0$. If the concentration is increased to fall in the range $c \in (3.290, 4.191)$, the particles spontaneously separate into isotropic domains of density $c = 3.290$ and high density nematic domains where $c = 4.191$. If $c > 4.191$, all particles are in the nematic phase. We find the location of the boundaries of the phase coexistence region, commonly referred to as binodals, to at least three decimal places consistent with their literature values [121].

If we point our attention to a dispersion subject to an orienting external field $K > 0$, the behaviour we find is dependent on the field strength. If the field is weak, the qualitative behaviour is unchanged: upon an increase of concentration, the now called paranematic phase (the field induces slight nematic order) transitions to a nematic phase through a region of phase coexistence. If the field is strong enough, however, the distinction between the external field induced paranematic phase and the concentration induced nematic phase vanishes. This region in which this distinction is lost is called superparanematic. The corresponding critical point is located at $K = 0.255$ and $c = 3.2$.

A disorienting field causes qualitatively different behaviour than an orienting field. Instead of a critical point, a tricritical point ($K = -1.18$, $c = 2.86$) marks the suppression of phase coexistence. At this tricritical point, the discontinuous phase transition transitions into a

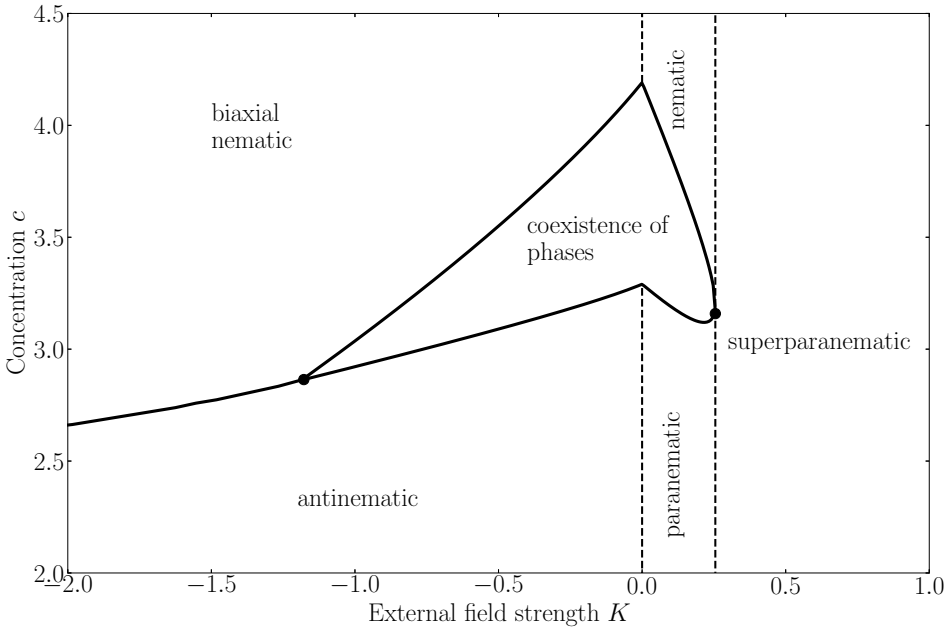

Figure 5.4: *Phase diagram of long rod-like particles in the concentration/external field plane. We can identify several phases by their distinctive symmetries. For sufficiently weak external fields, the dispersion can separate in a high density and a low density phase. The region in which this can occur is enclosed by the binodals, which are indicated as solid lines. We find a critical point at* $K = 0.255$ *and a tricritical point at* $K = -1.18$*. At the tricritical point, the binodals converge, and form a continuous phase transition between the antinematic and biaxial nematic phase.*

continuous one. For $K \ll 0$, the antinematic and the biaxial nematic phase are separated by this continuous phase transition, of which the location is determined by the location of the discontinuities in the derivatives of the order parameter S_2, see Fig. 5.3b for example.

This phase diagram is not a new result. It was calculated by Khoklov and Semenov by analytical variational methods and by Varga *et al.* using similar numerical methods to ours [112, 118, 119]. Varga *et al.* showed that the methods employed by Khokhlov and Semenov overestimate the critical and tricritical field strength by a factor of approximately 2. Our calculations corroborate that finding and show precise agreement with those of Varga and coworkers.

In real dispersions of long rods, other ordered high density phases such as the smectic phases can also be found. Therefore, the diagram printed in Fig. 5.4 is only complete if the particle aspect ratio is sufficiently high that we can justify taking the low-density limit.

5.3 Geometric percolation

Having found a way to quantify the orientational distribution using Onsager theory, we can now start to deal with our main target: percolation. We use the framework we set up in Chapter 2 to find the percolation threshold. We assume that each particle has a connectedness shell with diameter λ, which determines the regions in which we consider particles to be connected. In Chapter 2, we discussed how to find the weight average cluster size within this model. For homogeneously dispersed rodlike particles, it can be expressed as

$$S = 1 + \rho \int \mathrm{d}\mathbf{r} \langle \langle g^+(\mathbf{r}, \mathbf{u}, \mathbf{u}') \rangle \rangle', \tag{5.6}$$

where g^+ now only depends on the distance between the particles instead of both their absolute positions, such that we can define the coordinate $\mathbf{r}$ as $\mathbf{r}_2 - \mathbf{r}_1$. In this case, the density ρ is not dependent on any spatial coordinate. As we showed in chapter 3, it is appropriate to define the percolation threshold as the density at which this function diverges.

Note also that the definition of the average cluster size S is very similar to that of the static structure factor at vanishing wave length, but instead of an integration over g, the cluster size is found by integrating only over the connectedness part of g, named g^+. Due to this striking similarity, we find it irresistible to generalise by interpreting the average cluster size S as the value of the 'connectedness structure factor' S^+ at zero wave vector $S = S^+(\mathbf{q} = 0)$, such that

$$S^+(\mathbf{q}) = 1 + \rho \langle \langle \hat{g}^+(\mathbf{q}, \mathbf{u}, \mathbf{u}') \rangle \rangle', \tag{5.7}$$

and

$$\hat{g}^+(\mathbf{q}, \mathbf{u}, \mathbf{u}') = \int \mathrm{d}\mathbf{r} e^{-i\mathbf{q}\cdot\mathbf{r}} g^+(\mathbf{r}, \mathbf{u}, \mathbf{u}'). \tag{5.8}$$

This interpretation of S^+ allows us to extract not only information on the size of the clusters of particles, but also about their shape by considering nonzero wave vectors. We exploit this in a later section. For now, we focus solely on the cluster size.

5.3.1 The pair connectedness function

We make headway by applying theory introduced in Chapter 2. We have an expression of the cluster size as a function of the pair connectedness function g^+ (5.7), and in turn an expression of g^+ in terms of C^+, which can be rewritten recursively as

$$g^+(\mathbf{r}, \mathbf{u}, \mathbf{u}') = C^+(\mathbf{r}, \mathbf{u}, \mathbf{u}') + \rho \int \mathrm{d}\mathbf{r}'' \left\langle C^+(\mathbf{r} - \mathbf{r}', \mathbf{u}, \mathbf{u}'') g^+(\mathbf{r}', \mathbf{u}'', \mathbf{u}') \right\rangle'', \tag{5.9}$$

and finally, we have an expression of C^+, see Eq. (2.9). We hinted earlier at the fact that this problem might be more natural to tackle in Fourier space than in real space, which is more tangible here due to the convolutional nature of the integral above. To determine the cluster size, or more generally the connectedness structure factor, we need the Fourier transform of the pair connectedness function $\hat{g}^+$, see Eq. (5.7). Therefore, we solve Eq. (5.9) in the Fourier domain as well. We have

$$\hat{g}^+(\mathbf{q}, \mathbf{u}, \mathbf{u}') = \hat{C}^+(\mathbf{q}, \mathbf{u}, \mathbf{u}') + \rho \langle \hat{C}^+(\mathbf{q}, \mathbf{u}, \mathbf{u}'') \hat{g}^+(\mathbf{q}, \mathbf{u}'', \mathbf{u}') \rangle'', \tag{5.10}$$

where we assume that the dispersion of particles is homogeneous in space, and where we use the fact that a convolution product in real space becomes a normal product in reciprocal space. If

the orientational distribution is isotropic, the orientational averages factorise and Eq. (5.10) can be averaged over $\mathbf{u}'$ and solved straightforwardly [122], giving

$$S^{+}(\mathbf{q}) = 1 + \frac{\rho \left\langle \left\langle \hat{C}^{+}(\mathbf{q}, \mathbf{u}, \mathbf{u}') \right\rangle \right\rangle'}{1 - \rho \left\langle \left\langle \hat{C}^{+}(\mathbf{q}, \mathbf{u}, \mathbf{u}') \right\rangle \right\rangle'}, \tag{5.11}$$

where the percolation threshold can be easily identified to be at $\rho = 1/\langle\langle \hat{C}(\mathbf{0}, \mathbf{u}, \mathbf{u}')\rangle\rangle'$. In symmetry-broken phases, such as the nematic and antinematic, this expression does not give the correct value for the percolation threshold, and we must solve the full integral equation (5.10) and subsequently average to find the cluster size. However, the so-called excluded-volume approximation $\rho = 1/\langle\langle \hat{C}(\mathbf{0}, \mathbf{u}, \mathbf{u}')\rangle\rangle'$ is an occasionally used approximation in analytical models for approximating the percolation threshold. In Appendix C, we investigate to what degree this approximation gives accurate results in symmetry-broken phases.

Since we expect the percolation threshold for long rods to be at low volume fractions, we do not need a sophisticated closure for the Ornstein-Zernike equation. Therefore, we use the second virial approximation

$$C^{+}(1,2) \approx f^{+}(1,2) = \begin{cases} 1 & \text{if 1 and 2 are connected and do not overlap,} \\ 0 & \text{otherwise.} \end{cases} \tag{5.12}$$

This approximation is believed to become exact in the limit that $L/D \to \infty$, since, in that limit, the particle density at the threshold goes to zero with D/L [123]. The second virial closure is especially well suited for application in the Fourier domain. This can be easily seen by considering the fact that $\hat{C}^{+}(\mathbf{0}, \mathbf{u}, \mathbf{u}')$ is just the real-space integral of $C^{+}(\mathbf{r}, \mathbf{u}, \mathbf{u}')$. By Eq. (5.12), we can interpret $\hat{f}^{+}(\mathbf{0}, \mathbf{u}, \mathbf{u}')$ as the volume of space that one particle can occupy while being directly connected to a second particle, given their orientations $\mathbf{u}$ and $\mathbf{u}'$. This volume can be calculated to be

$$\begin{aligned} \hat{C}^{+}(\mathbf{0}, \mathbf{u}, \mathbf{u}') &\approx \hat{f}^{+}(0, \mathbf{u}.\mathbf{u}') \\ &= 2L^2(\lambda - D)|\mathbf{u} \times \mathbf{u}'| + 2\pi L\left(\lambda^2 - D^2\right) + \frac{4\pi}{3}\left(\lambda^3 - D^3\right) \\ &\approx 2L^2(\lambda - D)|\mathbf{u} \times \mathbf{u}'|, \end{aligned} \tag{5.13}$$

where the second and third term in the second line account for the effects of the end-caps of the spherocylinders, which become negligible as $L/D \to \infty$ [115]. We use the second virial closure for now. In Sec. 5.4, we employ a better approximation for particles with finite slenderness. The fact that this $|\mathbf{u} \times \mathbf{u}'|$ term shows up here as well as in Onsager theory is not a coincidence. In fact, one could state that this is due to the very definition of the direct correlation function being the second derivative of the excess free energy with respect to the density. This means that limit in which this virial approximation holds is equivalent to the Onsager limit. In this limit, the second virial approximation for percolation becomes exact in the same way that the Onsager free energy does.

5.3.2 Percolation islands

Having established a theoretical model for the pair connectedness function $\hat{g}^{+}(\mathbf{q}, \mathbf{u}, \mathbf{u}')$ and the associated cluster size $S = 1 + \rho\langle\langle \hat{g}^{+}(\mathbf{0}, \mathbf{u}, \mathbf{u}')\rangle\rangle'$, we can now employ a numerical procedure to investigate the behaviour of these functions. First, we find the orientational distribution

function as described in Sec. 5.2. The second step is solving the integral equation (5.10). However, we can reduce the dimensionality of the problem by averaging this equation over $\mathbf{u}'$, and solving for $\hat{h}(\mathbf{u}) = \langle \hat{g}^+(\mathbf{0}, \mathbf{u}, \mathbf{u}') \rangle'$. In terms of this intermediate function h, the connectedness Ornstein-Zernike equation now reads

$$\hat{h}(\mathbf{u}) = \left\langle \hat{C}^+(\mathbf{0}, \mathbf{u}, \mathbf{u}') \right\rangle' + \rho \left\langle C^+(\mathbf{0}, \mathbf{u}, \mathbf{u}'') \hat{h}(\mathbf{u}'') \right\rangle'', \tag{5.14}$$

with $S = 1 + \rho \left\langle \hat{h}(\mathbf{u}) \right\rangle$. In contrast to the nonlinear Onsager equation for the orientational distribution function, Eq. (5.14) is linear. This means that we do not need to perform the recursive iteration described in Sec. 5.2. Instead, we discretise it, and write it as a matrix equation, which is straightforward to solve

$$\mathbf{h} = \mathbf{b} + \mathbf{A}\mathbf{h}, \qquad \Longrightarrow \qquad \mathbf{h} = (\mathbf{I} - \mathbf{A})^{-1}\mathbf{b}, \tag{5.15}$$

where $h_i = h(\mathbf{u}_i)$, $b_i = \sum_j \psi_j w_j \hat{C}^+(\mathbf{0}, \mathbf{u}_i, \mathbf{u}_j)$, and $A_{ij} = \rho C^+(\mathbf{0}, \mathbf{u}_i, \mathbf{u}_j) w_j \psi_j$. Here we define ψ_j as the discretised orientational distribution function and w_j as the weight associated with grid-point $\mathbf{u}_j$ in the angular integration described in Appendix F.1.

The cluster size is now easily calculated with $S = 1 + \rho \sum_i h_i \psi_i w_i$. A positive finite value for S indicates a non-percolating dispersion, whereas a percolating dispersion is characterised by an non-physical, negative cluster size. We find the percolation threshold by requiring that $1/S = 0$, which translates to the physical requirement that the average cluster size diverges at the onset of percolation. A visual explanation of this procedure is provided in Fig. 5.5. We perform a linear interpolation in order to accurately find the percolation threshold. In Fig. 5.5, also the isotropic spinodal is indicated. This is the concentration below which the recursive iteration of the Onsager equation starting from a nematic trial function, converges to an isotropic distribution instead [124].

We have scanned the parameter space spanned by our three main parameters c, K, λ/D to obtain a comprehensive diagram that shows when percolation occurs, which we show in Fig. 5.6. If the connectedness shell thickness $\lambda < 1.15D$, the alignment induced by the external field and concentration prevents percolating clusters from appearing all together. This was shown analytically and confirmed by Monte Carlo simulations by Finner *et al.* [125]. If $1.15D < \lambda < 1.236D$, enclosed percolation islands are present [111, 125]. In this regime, for sufficiently weak external fields, percolating particle clusters are formed in the dilute phases (isotropic, paranematic, and antinematic). Upon an increase in the concentration or field strength, the additional induced alignment causes the percolating clusters to disconnect. This interplay between the effects of an increase in concentration causes very complex behaviour in the region around $\lambda = 1.24D$. Here, the percolation islands fan out, and transform from islands to peninsulas to normal coastlines. Within this transition there are examples of repeated re-entrance effects, where percolating clusters can form and break down multiple times.

A second observation we make from Fig. 5.6 is that the biaxial nematic phase, which can occur if $K < 0$, displays qualitatively different percolation behaviour than the uniaxial nematic phase ($K > 0$). The presence of the continuous phase transition for $K < 0$, creates a non-differentiability in the percolation diagram which is not present for $K > 0$.

5.3.3 Correlation lengths

We can use the connectedness structure factor $S^+(\mathbf{q})$ to investigate the shape of non-percolating clusters, to get a clearer understanding of the effects of biaxiality in the orientational distribution function on cluster formation. We quantify the shape of the clusters by evaluating the small

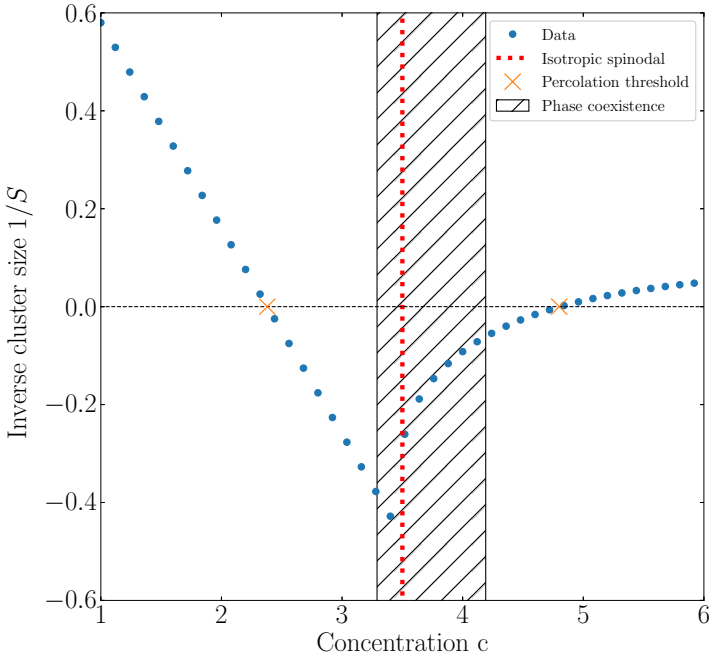

Figure 5.5: *Inverse cluster size as function of concentration for $K = 0$ and $\lambda/D = 1.21$. The percolation threshold is obtained by requiring that the mean cluster size diverges, i.e., $1/S = 0$. This figure illustrates the method that we use to find the percolation threshold for any value of the external field strength K and the connectivity range λ/D. In the figure, also the phase coexistence region and the isotropic spinodal are indicated as reference.*

$\mathbf{q} \to 0$ behaviour of the structure factor. First, we wil identify the correlation lengths in the small-wavelength expansion of the connectedness structure factor, and we subsequently illustrate a method of efficiently obtaining them. To start, we can immediately write down the expansion of the structure factor for small $\mathbf{q}$

$$S^+(\mathbf{q}) = S^+(\mathbf{0}) + \frac{1}{2}\left.\frac{\partial^2 S^+}{\partial q_x^2}\right|_{\mathbf{q}=\mathbf{0}} q_x^2 + \frac{1}{2}\left.\frac{\partial^2 S^+}{\partial q_y^2}\right|_{\mathbf{q}=\mathbf{0}} q_y^2 + \frac{1}{2}\left.\frac{\partial^2 S^+}{\partial q_z^2}\right|_{\mathbf{q}=\mathbf{0}} q_z^2 + \ldots, \tag{5.16}$$

because of the symmetry argument that our theory must be invariant to the transformation $\mathbf{q} \to -\mathbf{q}$, since our particles are inversion symmetric. This means that any term that is not even in all spatial directions, q_x, q_y, and q_z must vanish. The coefficients in front of the quadratic terms in q give us information about the shape of clusters. Therefore, it is customary to interpret them in terms of correlation lengths. Here, we define the correlation lengths as

$$\frac{S^+(\mathbf{q}) - 1}{S^+(\mathbf{0}) - 1} = \frac{\langle\langle \hat{g}^+(\mathbf{q}, \mathbf{u}, \mathbf{u}')\rangle\rangle'}{\langle\langle \hat{g}^+(\mathbf{0}, \mathbf{u}, \mathbf{u}')\rangle\rangle'} = 1 - \xi_x^2 q_x^2 - \xi_y^2 q_y^2 - \xi_z^2 q_z^2 + \ldots, \tag{5.17}$$

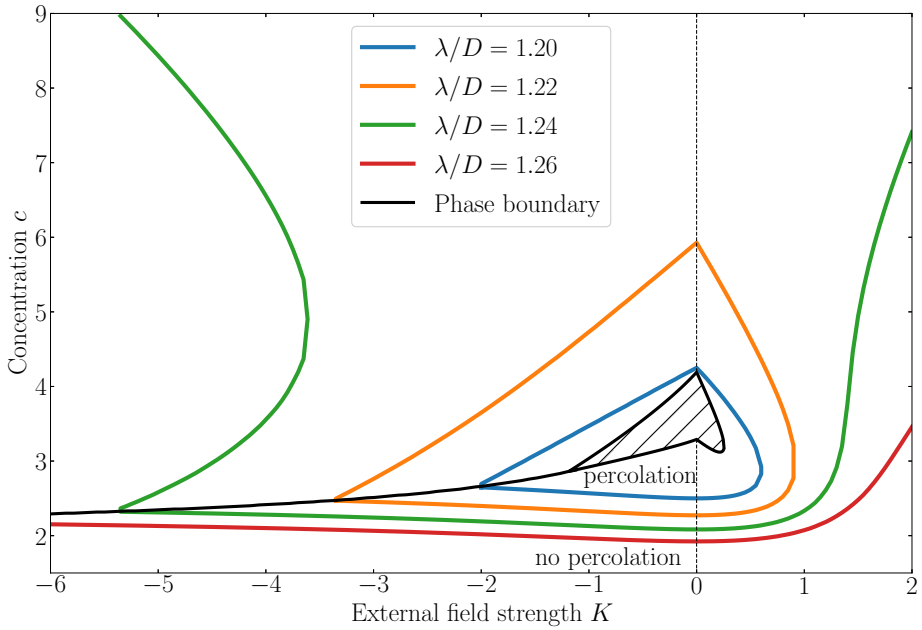

Figure 5.6: *The occurrence of percolation for varying concentration c, external field strength K and connectedness shell thickness λ/D. For very low concentration, no percolating cluster exists. As the concentration increases, a percolating cluster is formed and possibly destroyed (and sometimes reformed) dependent on the value of the external field strength and the connectivity range λ/D. Also indicated in the figure are the binodals and second order phase transition computed from Onsager theory, see Fig. 5.4.*

where ξ_x is the correlation length in the x-direction, and so on. These correlation lengths are qualitative, not quantitative, measures of the average dimensions of a cluster, and therefore are better suited to indicate cluster shape than size. To calculate these lengths, we need to calculate the pair connectedness function for finite wave vectors. To do this, we first require to obtain an expression for the direct connectedness function $\hat{C}^+(\mathbf{q},\mathbf{u},\mathbf{u}') = \hat{f}^+(\mathbf{q},\mathbf{u},\mathbf{u}')$. In the slender rod limit and for $\mathbf{qD} \ll 1$, this can be shown to equal

$$\hat{C}^+(\mathbf{q},\mathbf{u},\mathbf{u}') = \hat{f}^+(\mathbf{q},\mathbf{u},\mathbf{u}') = 2L^2(\lambda - D)|\mathbf{u}\times\mathbf{u}'|j_0\left(\frac{L}{2}\mathbf{q}\cdot\mathbf{u}\right)j_0\left(\frac{L}{2}\mathbf{q}\cdot\mathbf{u}'\right) \tag{5.18}$$

using Straley's oblique coordinate system [113, 126], where the spherical Bessel function $j_0(x) = \sin(x)/x$. With this expression, it is now possible to solve the connectedness Ornstein-Zernike equation (5.10) to get the full wave vector dependence of $\hat{g}^+$, and extract the correlation lengths.

However, there is a numerically less expensive way to go about this problem. We can derive an expression for the leading order anisotropic term in an expansion of the pair connectedness function

$$\hat{g}^+(\mathbf{q},\mathbf{u},\mathbf{u}') = \hat{g}^+(0,\mathbf{u},\mathbf{u}') + \left.\frac{\partial^2\hat{g}^+(\mathbf{q},\mathbf{u},\mathbf{u}')}{\partial\mathbf{q}\partial\mathbf{q}}\right|_{\mathbf{q}=0} : \mathbf{q}\,\mathbf{q} + \ldots, \tag{5.19}$$

where we define the double dot product : as the sum of the element-wise product of the matrices, and diadic products with $(\mathbf{a}\,\mathbf{b})_{ij} = a_i b_j$, where $\mathbf{a}$ and $\mathbf{b}$ are vectors. In Eq. (5.19), the linear term drops out for symmetry reasons.

The matrix of coefficients $\frac{\partial^2 \hat{g}^+(\mathbf{q},\mathbf{u},\mathbf{u}')}{\partial \mathbf{q}\partial \mathbf{q}}\Big|_{\mathbf{q}=0}$ contains all the information we need to find the correlation lengths, see Eq. (5.17). Therefore, we can restrict our calculation to finding this matrix instead of the full $\hat{g}^+(\mathbf{q},\mathbf{u},\mathbf{u}')$. We derive an expression for this matrix by taking the second derivative of the connectedness Ornstein-Zernike equation (5.10) and evaluating at $\mathbf{q} = 0$. Because the first derivatives of both $\hat{g}^+$ and $\hat{C}^+$ vanish at $\mathbf{q} = 0$, this simplifies to

$$\begin{aligned}\frac{\partial^2 \hat{g}^+(\mathbf{q},\mathbf{u},\mathbf{u}')}{\partial \mathbf{q}\partial \mathbf{q}}\bigg|_{\mathbf{q}=0} = \frac{\partial^2 \hat{C}^+(\mathbf{q},\mathbf{u},\mathbf{u}')}{\partial \mathbf{q}\partial \mathbf{q}}\bigg|_{\mathbf{q}=0} &+ \rho\left\langle \frac{\partial^2 \hat{C}^+(\mathbf{q},\mathbf{u},\mathbf{u}'')}{\partial \mathbf{q}\partial \mathbf{q}}\bigg|_{\mathbf{q}=0} \hat{g}^+(\mathbf{0},\mathbf{u}'',\mathbf{u}')\right\rangle'' \\ &+ \rho\left\langle \hat{C}^+(\mathbf{0},\mathbf{u},\mathbf{u}'')\,\frac{\partial^2 \hat{g}^+(\mathbf{q},\mathbf{u}'',\mathbf{u}')}{\partial \mathbf{q}\partial \mathbf{q}}\bigg|_{\mathbf{q}=0}\right\rangle''. \end{aligned} \tag{5.20}$$

Using the fact that $\frac{\partial^2 \hat{C}^+(\mathbf{q},\mathbf{u},\mathbf{u}')}{\partial \mathbf{q}\partial \mathbf{q}}\Big|_{\mathbf{q}=0} = -\frac{1}{6}(\lambda - D)L^4|\mathbf{u}\times\mathbf{u}'|(\mathbf{u}\,\mathbf{u} + \mathbf{u}'\mathbf{u}')$ we can formulate a closed equation for the coefficients that we need to calculate the correlation lengths[2],

$$\begin{aligned}\frac{\partial^2 \hat{g}^+(\mathbf{q},\mathbf{u},\mathbf{u}')}{\partial \mathbf{q}\partial \mathbf{q}}\bigg|_{\mathbf{q}=0} =& -\frac{1}{6}(\lambda - D)L^4|\mathbf{u}\times\mathbf{u}'|(\mathbf{u}\,\mathbf{u} + \mathbf{u}'\mathbf{u}') \\ &- \frac{1}{6}\rho(\lambda - D)L^4\left\langle |\mathbf{u}\times\mathbf{u}''|(\mathbf{u}\,\mathbf{u} + \mathbf{u}''\mathbf{u}'')\hat{g}^+(\mathbf{0},\mathbf{u}'',\mathbf{u}')\right\rangle'' \\ &+ 2\rho(\lambda - D)L^2\left\langle |\mathbf{u}\times\mathbf{u}''|\,\frac{\partial^2 \hat{g}^+(\mathbf{q},\mathbf{u}'',\mathbf{u}')}{\partial \mathbf{q}\partial \mathbf{q}}\bigg|_{\mathbf{q}=0}\right\rangle''. \end{aligned} \tag{5.21}$$

We can simplify the numerics by averaging this equation over $\mathbf{u}'$, and solving the result one matrix element at a time, since the elements are not coupled. The correlation lengths are now easily calculated using

$$\xi_\alpha^2 = -\frac{1}{2}\frac{\rho}{S^+(\mathbf{0}) - 1}\left\langle\left\langle \frac{\partial^2 \hat{g}^+(\mathbf{q},\mathbf{u},\mathbf{u}')}{\partial q_\alpha^2}\bigg|_{\mathbf{q}=0}\right\rangle\right\rangle', \tag{5.22}$$

where the Greek index α can denote any of the Cartesian coordinates. We numerically find that the off-diagonal elements vanish, as we predicted with symmetry arguments.

In Fig. 5.7, we plot the correlation lengths at different connectivity lengths and field strengths. For any orientational external field $K \geq 0$, we find as expected that the correlation lengths perpendicular to the field, ξ_x and ξ_y, are equal. The relative value of the parallel correlation length, ξ_z, is determined by the phase the dispersion is in. Naturally, in the isotropic phase ($K = 0$) it is equal to the perpendicular lengths, see Fig 5.7a. As a check of our numerical procedure, we verify that the correlation lengths in the isotropic phase in the low density limit are equal to $L/6$, which can also be calculated analytically, see App. D. Upon the entrance of the nematic phase, we see that the parallel correlation length is significantly larger than the perpendicular ones, indicating that clusters in the nematic phase are elongated. This was found in earlier work as well [111, 113, 125]. In the low density paranematic phase, the external field

[2]This identity was misprinted in our earlier work [111]. This error does not affect any of the results, or subsequent equations, of that work.

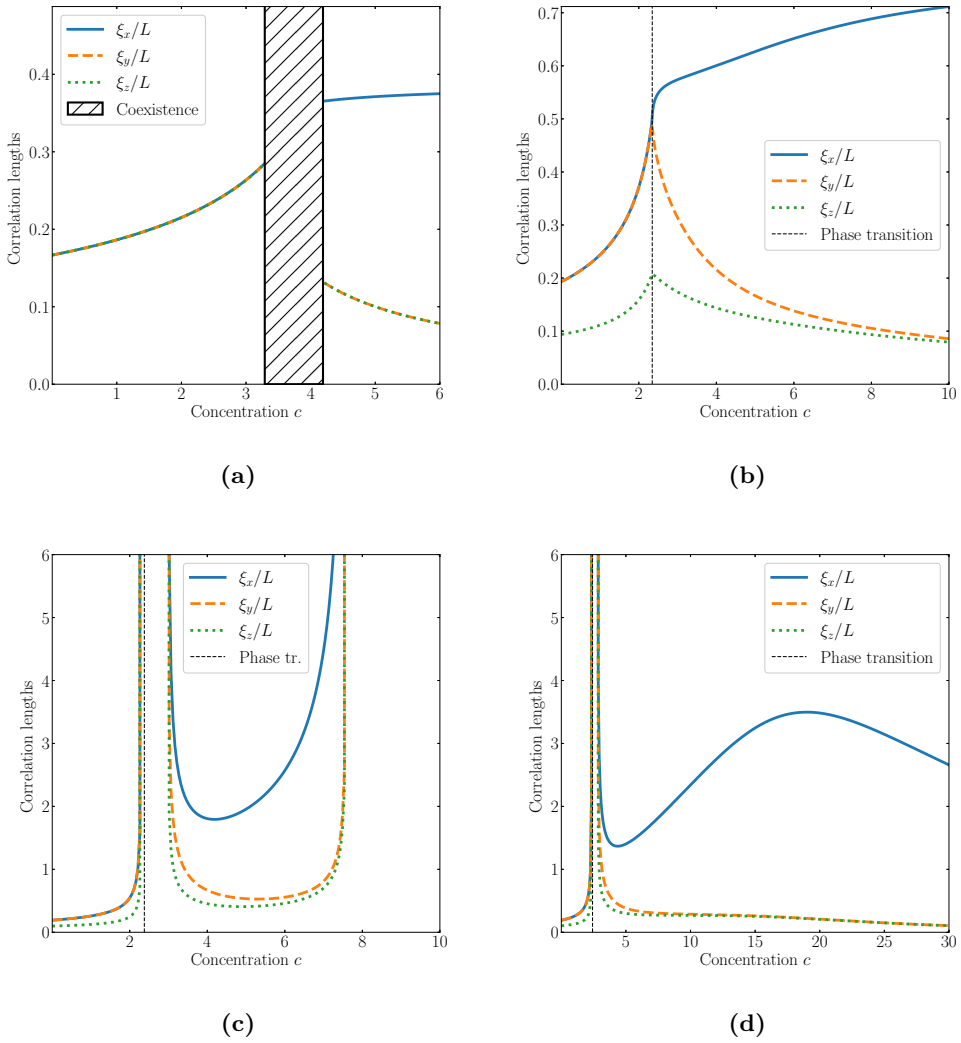

Figure 5.7: *Correlation lengths as function of the concentration along vertical slices in Fig. 5.6. The subfigures correspond to the slices across the isotropic-nematic transition at $K = 0$, $\lambda/D = 1.1$ (a), and across the antinematic-biaxial nematic transition at $K = -5$ (b), $\lambda/D = 1.2$; $K = -4.5$, $\lambda/D = 1.24$ (c), and $K = -4$, $\lambda/D = 1.23$ (d). We see a wide variety of behaviour across this transition, depending on the field strength and connectivity length.*

causes a slight alignment of the particles, which in turn causes a slight elongation of the clusters, mildly mimicking the behaviour in the nematic phase.

If we consider a negative field strength, we can clearly see the effects of biaxiality on the cluster shape. In the low density antinematic phase, the particles are oriented away from the z-axis slightly. This results in the fact that the correlation lengths in the direction perpendicular to the field axis are higher than the parallel one. We therefore expect that the clusters in this phase take the shape of oblate spheroids. When the antinematic-biaxial nematic continuous phase

transition is approached, the clusters become larger, increasing the correlation lengths. Dependent on the connectivity length this increase may or may not cause percolation, see Figs. 5.7b–5.7d. At the phase transition, indicated in the figures with black dashed lines, the correlation lengths ξ_z and ξ_y show a clear cusp, and start to decrease when the concentration is increased further. The correlation length along the director, which is defined to coincide with the x-axis in this phase, however does not show this nondifferentiability, and keeps increasing monotonically. The relative strength of the external field and the internal aligning field caused by excluded volume effects determines the ratio of the two correlation lengths perpendicular to the director ξ_z and ξ_y. In this phase therefore, we conclude that the ellipsoidal clusters are triaxial.

5.4 Finite aspect ratios

In the preceding sections, we looked at the phase behaviour and percolation of infinitely slender nanorods. The question arises in what way this behaviour changes when the particle aspect ratio decreases from infinity. In the context of Onsager theory, a few methods have been developed to account for particles with a finite length-diameter ratio. The best known one, produced by Lee and Parsons independently, is based on interpolating between the free energy of infinitely slender particles produced by Onsager and the Carnahan-Starling free energy of spheres. This approximation produces highly accurate phase diagrams, and has been widely used in literature [127–129]. An alternative method, called Scaled Particle Theory, is based on an interpolation of the work required to insert a very large and a very small particle into the dispersion [130, 131]. This estimation of the work is used to correct the free energy. Scaled Particle Theory has been shown to produce more accurate results when applied to percolation theory by Finner *et al.* [132]. For this reason, we choose to use this method. A detailed comparison between both methods and Monte Carlo simulation results is presented in by Finner *et al.*, who showed that Scaled Particle Theory predictions for the percolation threshold deviates less than 10%, even for rods with aspect ratios down to $L/D = 5$ [132]. Here, we give a quick overview of this theory before applying it to the percolation problem. We first use scaled particle theory to adjust the Onsager free energy to take into account the end-caps of the particles, and find the equilibrium orientational distribution function. Subsequently, we use the same adjustment for the direct connectedness function $\hat{C}^{+}$, in order to accurately find the percolation threshold.

5.4.1 Scaled Particle Theory

We model our N particles as spherocylinders with cylindrical length L, diameter D. This definition implies that the so-called 'full' aspect ratio equals $(L + D)/D$. However, in this work we refer the to aspect ratio as the simple ratio L/D. The volume fraction of this dispersion is given by

$$\varphi = \frac{N}{V}\left(\frac{\pi L D^2}{4} + \frac{\pi D^3}{6}\right) = c\left(\frac{D}{L} + \frac{2}{3}\frac{D^2}{L^2}\right), \tag{5.23}$$

where V is the volume available to the rods.

Cotter and Wacker derived an expression for the Scaled Particle Theory free energy of spherocylindrical particles, that incorporates an approximation of virial terms beyond the second. This free energy is given up to a constant by [130, 131, 133]

$$\frac{F}{N k_B T} = f = \ln\left(\frac{\varphi}{1-\varphi}\right) + \langle \ln \psi(\mathbf{u}) \rangle + A\left(\frac{\varphi}{1-\varphi}\right) + \frac{B}{2}\left(\frac{\varphi}{1-\varphi}\right)^2 - K\langle \cos^2\theta \rangle, \tag{5.24}$$

where

$$A = 3 + \frac{12}{\pi} \frac{\left(\frac{L}{D}\right)^2}{3\frac{L}{D} + 2} \left\langle \langle |\mathbf{u} \times \mathbf{u}'| \rangle \right\rangle', \tag{5.25}$$

and

$$B = \frac{12\left(\frac{L}{D} + 1\right)\left(2\frac{L}{D} + 1\right)}{\left(2 + 3\frac{L}{D}\right)^2} + \frac{48}{\pi} \frac{\frac{L^2}{D^2}\left(\frac{L}{D} + 1\right)}{\left(2 + 3\frac{L}{D}\right)^2} \left\langle \langle |\mathbf{u} \times \mathbf{u}'| \rangle \right\rangle', \tag{5.26}$$

where the new L/D-dependence is due to the Scaled Particle Theory approximation. It is not hard to show that this free energy reduces to expression (5.2) as $D/L \to 0$ and $\varphi \to 0$.

From this expression of the free energy, we find the equilibrium orientational distribution function by requiring that $\delta f / \delta \psi = 0$, and solving the resulting integral equation

$$\psi(\mathbf{u}) = \frac{1}{Z} \exp\left(K \cos^2\theta - \frac{8\Gamma c}{\pi} \left\langle |\mathbf{u} \times \mathbf{u}'| \right\rangle' \right), \tag{5.27}$$

where Z is a normalisation constant, and

$$\Gamma = \frac{1}{1-\varphi}\left(1 + \frac{\varphi}{1-\varphi}\frac{2 + 2\frac{L}{D}}{2 + 3\frac{L}{D}}\right). \tag{5.28}$$

is the Scaled Particle Theory correction factor. Note that Eq. (5.27) is identical to Eq. (5.4) for the infinite aspect ratio case if $\Gamma = 1$. Indeed, it is easy to see that $\Gamma \to 1$ as $L/D \to \infty$ at constant c.

Using the equilibrium orientational distribution function $\psi(\mathbf{u})$, we can calculate the dimensionless pressure p and chemical potential μ in the same way as described in Section 5.2. We find[3]

$$p = \frac{\Pi\varphi}{\rho k_B T} = c\left(\frac{\varphi}{1-\varphi}\right) + Ac\left(\frac{\varphi}{1-\varphi}\right)^2 + Bc\left(\frac{\varphi}{1-\varphi}\right)^3 \tag{5.29}$$

and

$$\begin{aligned} \mu = {} & \ln\left(\frac{\varphi}{1-\varphi}\right) + \langle \ln\psi(\mathbf{u}) \rangle + (1 + 2A)\left(\frac{\varphi}{1-\varphi}\right) \\ & + \left(A + \frac{3}{2}B\right)\left(\frac{\varphi}{1-\varphi}\right)^2 + B\left(\frac{\varphi}{1-\varphi}\right)^3 - K\langle \cos^2\theta \rangle. \end{aligned} \tag{5.30}$$

Using the pressure and chemical potential, we calculate the binodals and second order phase transition by the same method as described in Sec. 5.2. The resulting phase diagrams for $L/D = 100$ and $L/D = 20$ are plotted in Fig. 5.8.

From this figure, we conclude that the external field strengths at the critical and tricritical points are only weakly dependent on the aspect ratio. The critical and tricritical volume fractions, however, are proportional to D/L as $L/D \to \infty$. This could have also been concluded from Sect. 5.2. At aspect ratios below roughly one hundred, we find a clear deviation from this scaling behaviour, which is in excellent agreement with simulations and numerical work at $K = 0$ [133].

[3]Note: here, the dimensionless pressure is defined slightly differently than in Sec. 5.2.

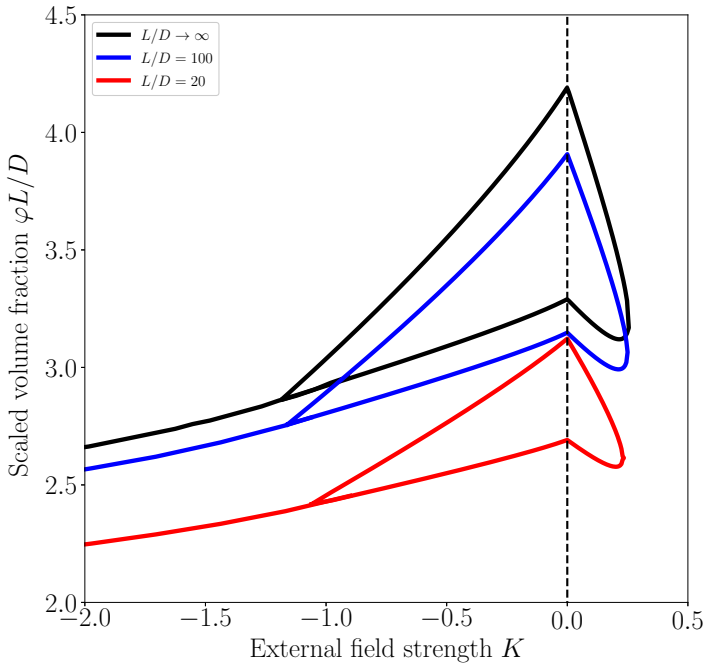

Figure 5.8: *Phase diagram of hard spherocylinders with aspect ratios $L/D \in \{\infty, 100, 20\}$ in terms of a scaled volume fraction as function of the external field strength K. Within the enclosed region, high and low density phases coexist. We calculated the location of the binodals using the Onsager free energy, with Scaled Particle Theory corrections for the finite aspect ratios. The terminology of the phases is shown in Fig 5.4.*

5.4.2 Percolation of spherocylinders

To apply the Scaled Particle Theory correction also to the calculation of the cluster size, we closely follow the procedure presented in Ref. [115]. We rescale our contact volume with the same parameter Γ that we used to rescale our excluded volume, given by Eq. (5.28), such that the closure of the Connectedness Ornstein-Zernike equation (5.10) reads,

$$\hat{C}^{+}(\mathbf{0}, \mathbf{u}, \mathbf{u}') = \Gamma \hat{f}^{+}(\mathbf{0}, \mathbf{u}, \mathbf{u}'). \tag{5.31}$$

In this equation, the contact volume, including the contributions by the hemispherical end-caps is given by

$$\hat{f}^{+}(\mathbf{0}, \mathbf{u}, \mathbf{u}') = 2L^2(\lambda - D)|\mathbf{u} \times \mathbf{u}'| + 2\pi L D^2 \left(\left(\frac{\lambda}{D} \right)^2 - 1 \right) + \frac{4\pi D^3}{3} \left(\left(\frac{\lambda}{D} \right)^3 - 1 \right), \tag{5.32}$$

where λ is the connectivity length. The new second and third terms account for the effects of the hemispherical end-caps. We note that the form of closure (5.31) is not based on physical arguments, but rather on considerations of convenience. However, in our view it makes sense to

use the same renormalisation in the excess free energy as in the direct connectedness function because there is a strong physical connection between the two. Additionally, it can be shown that this approximation yields very accurate results for aspect ratios $L/D > 10$ [115]. By the same methods described in Sec. 5.3.2, we now solve the connectedness Ornstein-Zernike equation and find the cluster size as function of the volume fraction, aspect ratio, connectedness criterion, and external field strength.

The percolation threshold can again be found by the requirement that the cluster size diverges. This procedure results in the percolation diagrams shown in Fig 5.9. Here we plot for aspect ratios $L/D = 100$ and $L/D = 20$ the percolation thresholds for several different connectedness criteria as function of the external field. The diagram for $L/D \to \infty$ is given in Fig 5.6. The percolation thresholds are expressed in terms of the product of the volume fraction and the aspect ratio $\varphi L/D$, which in the slender particle limit is the exact definition of our parameter c.

We find in full agreement with our earlier numerical work that the finite particle slenderness introduces a high concentration percolation transition. After all, a finite dispersion with sufficiently many particles always percolates. The location of this high concentration percolation threshold is strongly dependent on the aspect ratio. Apart from this additional percolation threshold, our results show that the diagram does not change qualitatively as the aspect ratio decreases to $L/D = 20$. However, if the particle anisometry is decreased further, the percolation islands and peninsulas disappears entirely. For spherical particles, at $L/D = 0$, the diagram has lost its dependence on the external field, as the orientation of spheres has no influence on percolation within our model. In this regime, the concentration at which percolating clusters appear is only dependent on the ratio between the connectivity criterion and the particle diameter.

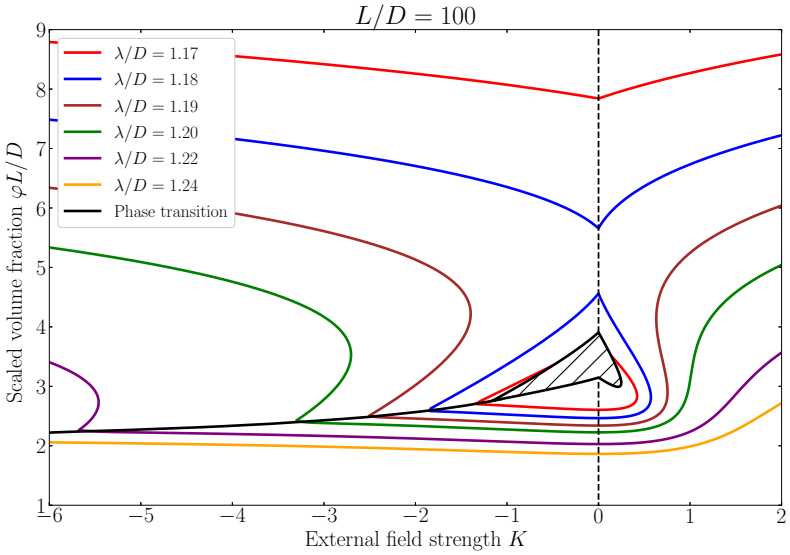

(a)

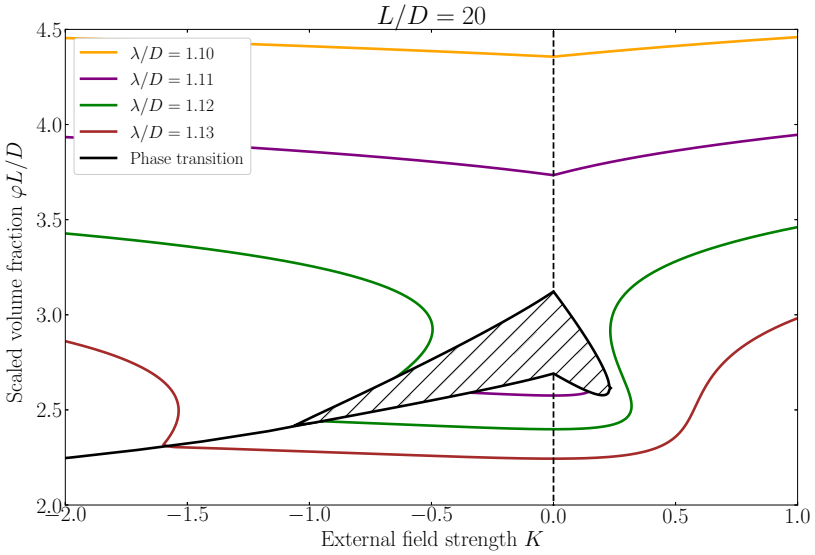

(b)

Figure 5.9: *Percolation threshold for spherocylinders with aspect ratio $L/D = 100$ (a) and $L/D = 20$ (b) as function of the external field strength K for different connectedness criterion λ/D. The hatched region is the region of phase coexistence.*

5.5 Discussion and conclusion

We have numerically investigated the effect of external field induced antinematic order on the percolation threshold and cluster shape in dispersions of spherocylindrical particles. This was performed in the context of a self-consistent combination between Onsager theory of the isotropic-nematic phase transition and the connectedness Ornstein-Zernike equation by Coniglio and coworkers [40, 116]. We applied Scaled Particle Theory corrections to incorporate approximations of the higher order virial terms in the Onsager free energy and used a similar approximation for the direct connectedness function. This allowed us to generalise our findings to rods with aspect ratios of down to approximately $L/D = 10$.

For small connectivity lengths, we find that percolation islands form in the concentration/external field plane, meaning that upon an increase of concentration, percolating clusters can form and break down subsequently. For particles with finite aspect ratios, as we usually encounter in real materials, a high density percolation threshold always exists. If the connectivity length increases, the percolation islands grow, and eventually fan out, connecting to this high density threshold. On the other hand, when the connectivity length is large enough, the low density percolation can never be broken down by the induced order due to the external field or excluded-volume effects, and it always precedes the abovementioned high density percolation threshold. To the best knowledge of the authors, no simulations have been conducted of percolation of nanorods subject to externally applied quadrupolar fields. However, our results in the disorientational regime show surprising qualitative resemblance with the percolation diagrams of simulations of nanorods in shear flow [134]. However, we expect this similarity to be coincidence because the authors show that this re-entrant perclation behaviour is due to rod aggregation instead of alignment.

As the aspect ratio decreases, and the rods increasingly resemble spheres, the effects described above disappear. For spherical particles, indeed, the influence of the external field vanishes, because the average surface to surface distance cannot any longer be influenced by the rotational degrees of freedom. For homogeneously dispersed spherical particles, the percolation threshold is uniquely determined by the ratio λ/D as we have seen in previous chapters.

It is a major challenge to disperse carbon nanotubes isotropically in polymer composites, not only due to the intrinsically occurring phase transitions, but also due to the used manufacturing processes such as spin coating and shear mixing [135]. Even in controlled laboratory experiments, external electric, magnetic or flow fields are omnipresent and our results show that the effects of such weak external fields on the percolation threshold can be rather significant. We believe that this fact can explain a part of the scatter in the experimental data of the conductivity of nanocomposite materials.

Additionally, we calculated correlation lengths to get insight into the shape of nonpercolating clusters. Our results confirm earlier findings that from the isotropic to nematic phase cluster go from spherical to elongated. Moreover, across the continuous antinematic-biaxial nematic phase transition, we find that the clusters transition from being oblate spheroids to triaxial prolate ellipsoids. The highly anisometric shape of clusters in these phases can be exploited to generate materials that have anisotropic conductivity properties [136].

Chapter 6

Conclusions and outlook

The aim of this work has been to investigate the behaviour of the percolation threshold of particle dispersions. We considered two different models:

- a non-equilibrium dispersion of hard spherical particles subject to a simple shear flow, and,
- an equilibrium dispersion of hard rodlike particles subject to external quadrupolar fields.

The common denominator of these two distinct dispersions is that they are both meant to model the influence of experimentally induced external influences on the percolation threshold in polymer composites.

With the first model, we have found that the influence of shear flow on the percolation threshold of a dispersion of spherical particles can be captured by a simple heuristic model semi-quantitatively. The model predicts that the percolation threshold is slightly increased if the connectivity length is large with respect to the particle diameter, and decreased up to roughly 10% if the particle diameter is close to the connectivity range. We postulate that this decrease is caused by the emergence of linear contact clusters that have been experimentally observed in sheared dispersions [78]. To provide a further indication for this conjecture, we show that subpercolating clusters elongate due to the shear flow for a certain choice of parameters. We, however, do not provide conclusive evidence for our claim.

The theoretical model slightly overestimates the influence of the shear flow on the percolation threshold when compared with molecular dynamics simulations. This discrepancy might be caused by a variety of factors, but is probably due to the heuristic nature of the used criterion or the fact that we neglected all shear-induced many-body correlations.

The second model shows the highly complex physics that arise when the particles are non-spherical and hard. Such particles are known to self-organise entropically into liquid-crystalline phases. The combination of this internally driven alignment with externally applied aligning or disaligning fields leads to a variety of symmetry-broken phases. We show that the percolation threshold is highly sensitive to the degree of alignment in a dispersion of rodlike particles. This sensitivity is manifested by the fact that material-spanning clusters can form and break down multiple times with increasing particle density, while keeping all other relevant parameters constant. We also show that this behaviour is present over a wide range of particle aspect ratios, and causes the cluster shape to become bi- or tri-axial depending on the underlying thermodynamic phase.

Outlook

Due to the heuristic nature of the percolation criterion we applied to find the percolation threshold in the first model, we do not have a way of analytically investigating the degree of anisometry of the particle clusters. To provide further evidence for our conjecture that the decrease in the percolation threshold is due to the emergence of linear clusters, it would be interesting to investigate the cluster shape more comprehensively and to measure the percolating cluster statistics depending on the shear rate with molecular dynamics simulations. Unfortunately, we have not found the opportunity to conduct such an analysis with a sufficiently satisfactory degree of comprehensiveness. Therefore, we leave this problem to further research.

Additionally, to make our model more quantitative, several improvements could be made. First of all, shear-induced many-body correlations could be taken into account. This can be done, for example, by including three-body correlations explicitly in the Smoluchowski theory and close the theory by approximating the three-body correlations in terms of the two-body correlations. Alternatively, one could leverage our knowledge of the equilibrium material to use the Percus-Yevick pair correlation function as the equilibrium structure directly in Eq. (A.14), effectively including many-body correlations implicitly.

In addition to many-body interactions, we have neglected hydrodynamic interactions entirely throughout this analysis. To include them, one must incorporate the tensorial mobility of the particles explicitly. For example, this can be achieved by including hydrodynamic interactions in the form of pairwise lubrication forces as is done in Ref. [91]. Such a procedure is especially applicable if the shear flow is strong relative to thermal diffusion and the the particle volume fraction is high.

To do away with the heuristic nature of the theory altogether, it might be possible to formulate a dynamic percolation theory from dynamic density functional theory or power functional theory similar to how connectedness Ornstein-Zernike theory is derived from liquid state Ornstein-Zernike theory [137]. However, as far as is known to the authors, no such formulation exists in the literature. Alternatively, Fortuin and Kasteleyn have shown that the percolation can also be considered in terms of generalised Ising, or Potts models [138, 139]. Since methods exist to study the dynamics of Ising models in external fields, see for example Ref. [140], it is imaginable that such methods could also be applied to the percolation problem. However, even if dynamical percolation could be studied this way, it is not entirely straightforward to apply such lattice models to continuum systems, although the formalism exists [141].

To extend our model to non-spherical particles also, it is necessary to adapt the Smoluchowski theory to account to include the resulting anisometric structures as well. For particles with very high aspect ratios, the percolation criterion that we have used, has been shown to fail, and must be adapted to retain its predictive power.

Although simulations of Kwon *et al.* show that dispersions of rodlike particles in shear flow have strikingly similar re-entrant percolation behaviour to that we observed for rods in external quadrupolar fields [134], the underlying cause is probably different. Indeed, in the case of our work, percolation is suppressed by external-field-induced particle alignment, whereas Kwon and coworkers show that hydrodynamic agglomeration of rods is the origin. To properly theoretically model percolation in sheared suspensions of hard rods, therefore, a dynamical percolation theory needs to be set up that can incorporate not only the entropically driven particle alignment, but also the shear-induced particle aggregation.

Acknowledgements

I would like to express my special thanks of gratitude to my supervisors Paul van der Schoot and René de Bruijn for their continual encouragement, participation and support, and without whom this document would not be lying before you. Additionally, I thank Shari Finner and Mark Miller for their very useful and enlightening discussions. Lastly, I would like to thank all members of the Soft Matter and Biological physics group for their action-packed coffee breaks, captivating conversations, and—especially during the world-wide pandemic—much-needed company.

Bibliography

[1] C.Y. Li, L. Li, W. Cai, S.L. Kodjie, and K.K. Tenneti. Nanohybrid shish-kebabs: Periodically functionalized carbon nanotubes. *Advanced Materials*, 17:1198–1202, 2005.

[2] M. Moniruzzaman and K.I. Winey. Polymer nanocomposites containing carbon nanotubes. *Macromolecules*, 39:5194–5205, 2006.

[3] T. Wu, E. Chen, Y. Lin, M. Chiang, and G. Chang. Preparation and characterization of melt-processed polycarbonate/multiwalled carbon nanotube composites. *Polymer Engineering & Science*, 48:1369–1375, 2008.

[4] K.H. Kim and W.H. Jo. A strategy for enhancement of mechanical and electrical properties of polycarbonate/multi-walled carbon nanotube composites. *Carbon*, 47:1126–1134, 2009.

[5] J.A. King, M.D. Via, J.A. Caspary, M.M. Jubinski, I. Miskioglu, O.P. Mills, and G.R. Bogucki. Electrical and thermal conductivity and tensile and flexural properties of carbon nanotube/polycarbonate resins. *Journal of Applied Polymer Science*, 118:2512–2520, 2010.

[6] B. Hornbostel, P. Pötschke, J. Kotz, and S. Roth. Single-walled carbon nanotubes/polycarbonate composites: Basic electrical and mechanical properties. *physica status solidi (b)*, 243:3445–3451, 2006.

[7] B.K. Satapathy, R. Weidisch, P. Pötschke, and A. Janke. Tough-to-brittle transition in multiwalled carbon nanotube (mwnt)/polycarbonate nanocomposites. *Composites Science and Technology*, 67:867–879, 2007.

[8] S. Abbasi, P.J. Carreau, A. Derdouri, and M. Moan. Rheological properties and percolation in suspensions of multiwalled carbon nanotubes in polycarbonate. *Rheologica Acta*, 48:943, 2009.

[9] E. Kymakis and G.A.J. Amaratunga. Single-wall carbon nanotube/conjugated polymer photovoltaic devices. *Applied Physics Letters*, 80:112–114, 2002.

[10] E. Kymakis, I. Alexandrou, and G.A.J Amaratunga. High open-circuit voltage photovoltaic devices from carbon-nanotube-polymer composites. *Journal of Applied Physics*, 93:1764–1768, 2003.

[11] P. Avouris, M. Freitag, and V. Perebeinos. Carbon-nanotube photonics and optoelectronics. *Nature Photonics*, 2:341–350, 2008.

[12] B. Philip, J.K. Abraham, A. Chandrasekhar, and V.K. Varadan. Carbon nanotube/pmma composite thin films for gas-sensing applications. *Smart Materials and Structures*, 12:935, 2003.

[13] W. Fu, L. Liu, K. Jiang, Q. Li, and S. Fan. Super-aligned carbon nanotube films as aligning layers and transparent electrodes for liquid crystal displays. *Carbon*, 48:1876–1879, 2010.

[14] C. Baughman, R.H.and Cui, A.A. Zakhidov, Z. Iqbal, J.N. Barisci, G.M. Spinks, G.G. Wallace, A. Mazzoldi, D. De Rossi, A.G. Rinzler, et al. Carbon nanotube actuators. *Science*, 284:1340–1344, 1999.

[15] B.J. Landi, R.P. Raffaelle, M.J. Heben, J.L. Alleman, W. VanDerveer, and T. Gennett. Single wall carbon nanotube- nafion composite actuators. *Nano Letters*, 2:1329–1332, 2002.

[16] I. Kang, Y.Y. Heung, J.H. Kim, J.W Lee, R. Gollapudi, S. Subramaniam, S. Narasimhadevara, D. Hurd, G.R. Kirikera, V. Shanov, et al. Introduction to carbon nanotube and nanofiber smart materials. *Composites Part B: Engineering*, 37:382–394, 2006.

[17] J. Di, X. Zhang, Z. Yong, Y. Zhang, D. Li, R. Li, and Q. Li. Carbon-nanotube fibers for wearable devices and smart textiles. *Advanced Materials*, 28:10529–10538, 2016.

[18] Z. Zeng, M. Chen, H. Jin, W. Li, X. Xue, L. Zhou, Y. Pei, H. Zhang, and Z. Zhang. Thin and flexible multi-walled carbon nanotube/waterborne polyurethane composites with high-performance electromagnetic interference shielding. *Carbon*, 96:768–777, 2016.

[19] Z. Wu, Z. Chen, X. Du, J.M. Logan, J. Sippel, M. Nikolou, K. Kamaras, J.R. Reynolds, D.B. Tanner, A.F. Hebard, et al. Transparent, conductive carbon nanotube films. *Science*, 305:1273–1276, 2004.

[20] C.A. Martin, J.K.W. Sandler, M.S.P. Shaffer, M.K. Schwarz, W. Bauhofer, K. Schulte, and A.H. Windle. Formation of percolating networks in multi-wall carbon-nanotube–epoxy composites. *Composites Science and Technology*, 64:2309–2316, 2004.

[21] J.K.W. Sandler, J.E. Kirk, I.A. Kinloch, M.S.P. Shaffer, and A.H. Windle. Ultra-low electrical percolation threshold in carbon-nanotube-epoxy composites. *Polymer*, 44:5893–5899, 2003.

[22] A.V. Kyrylyuk and P. van der Schoot. Continuum percolation of carbon nanotubes in polymeric and colloidal media. *Proceedings of the National Academy of Sciences*, 105: 8221–8226, 2008.

[23] G. Hu, C. Zhao, S. Zhang, M. Yang, and Z. Wang. Low percolation thresholds of electrical conductivity and rheology in poly (ethylene terephthalate) through the networks of multi-walled carbon nanotubes. *Polymer*, 47:480–488, 2006.

[24] T. Ackermann, R. Neuhaus, and S. Roth. The effect of rod orientation on electrical anisotropy in silver nanowire networks for ultra-transparent electrodes. *Scientific Reports*, 6:34289, 2016.

[25] Q. Xue. The influence of particle shape and size on electric conductivity of metal–polymer composites. *European Polymer Journal*, 40:323–327, 2004.

[26] E.J. Garboczi, K.A. Snyder, J.F. Douglas, and M.F. Thorpe. Geometrical percolation threshold of overlapping ellipsoids. *Physical Review E*, 52:819, 1995.

[27] A.L.R. Bug, S.A. Safran, and I. Webman. Continuum percolation of rods. *Physical Review Letters*, 54:1412, 1985.

[28] O. Breuer and U. Sundararaj. Big returns from small fibers: a review of polymer/carbon nanotube composites. *Polymer Composites*, 25:630–645, 2004.

[29] R.M. Mutiso, M.C. Sherrott, J. Li, and K.I. Winey. Simulations and generalized model of the effect of filler size dispersity on electrical percolation in rod networks. *Physical Review B*, 86:214306, 2012.

[30] K. Shehzad, T. Hussain, A.T. Shah, A. Mujahid, M.N. Ahmad, T. Anwar, S. Nasir, A. Ali, et al. Effect of the carbon nanotube size dispersity on the electrical properties and pressure sensing of the polymer composites. *Journal of Materials Science*, 51:11014–11020, 2016.

[31] R.H.J. Otten and P. van der Schoot. Continuum percolation of polydisperse nanofillers. *Physical Review Letters*, 103:225704, 2009.

[32] M.C. Hermant. *Manipulating the Percolation Threshold of Carbon Nanotubes in Polymeric Composites*. PhD-Thesis, Eindhoven University of Technology, Eindhoven, 2009.

[33] B. Vigolo, C. Coulon, M. Maugey, C. Zakri, and P. Poulin. An experimental approach to the percolation of sticky nanotubes. *Science*, 309:920–923, 2005.

[34] J. Li, P.C. Ma, W.S. Chow, C.K. To, B.Z. Tang, and J.-K. Kim. Correlations between percolation threshold, dispersion state, and aspect ratio of carbon nanotubes. *Advanced Functional Materials*, 17:3207–3215, 2007.

[35] F. Du, J.E. Fischer, and K.I. Winey. Effect of nanotube alignment on percolation conductivity in carbon nanotube/polymer composites. *Physical Review B*, 72:121404, 2005.

[36] W. Bauhofer and J.Z. Kovacs. A review and analysis of electrical percolation in carbon nanotube polymer composites. *Composites Science and Technology*, 69:1486–1498, 2009.

[37] S. Kwon, H.W. Cho, G. Gwon, H. Kim, and B.J. Sung. Effects of shape and flexibility of conductive fillers in nanocomposites on percolating network formation and electrical conductivity. *Physical Review E*, 93:032501, 2016.

[38] T. Hu and B.I. Shklovskii. Hopping conductivity of a suspension of flexible wires in an insulator. *Physical Review B*, 74:174201, 2006.

[39] J.-P. Hansen and I.R. McDonald. *Theory of simple liquids*. Elsevier, Amsterdam, 1990.

[40] A. Coniglio, U. De Angelis, and A. Forlani. Pair connectedness and cluster size. *Journal of Physics A: Mathematical and General*, 10:1123, 1977.

[41] L.S. Ornstein and F. Zernike. Accidental deviations of density and opalescence at the critical point of a single substance. In *Proceedings of the Royal Netherlands Academy of Arts and Sciences*, volume 17, pages 793–806, 1914.

[42] J.K. Percus and G.J. Yevick. Analysis of classical statistical mechanics by means of collective coordinates. *Physical Review*, 110:1, 1958.

[43] E.G. Noya, C. Vega, and E. de Miguel. Determination of the melting point of hard spheres from direct coexistence simulation methods. *The Journal of Chemical Physics*, 128:154507, 2008.

[44] T. DeSimone, S. Demoulini, and R.M. Stratt. A theory of percolation in liquids. *The Journal of Chemical Physics*, 85:391–400, 1986.

[45] D.C. Rapaport. *The art of molecular dynamics simulation*. Cambridge university press, Cambridge, 2004.

[46] C. Zhang, S. Liu, H. Zhou, and Y. Zhou. An accurate, residue-level, pair potential of mean force for folding and binding based on the distance-scaled, ideal-gas reference state. *Protein Science*, 13:400–411, 2004.

[47] E. Paquet and H.L. Viktor. Molecular dynamics, monte carlo simulations, and langevin dynamics: a computational review. *BioMed Research International*, 2015, 2015.

[48] R.W. Pastor. Techniques and applications of langevin dynamics simulations. In *The Molecular Dynamics of Liquid Crystals*, pages 85–138. Springer, 1994.

[49] A. Scala. Event-driven langevin simulations of hard spheres. *Physical Review E*, 86:026709, 2012.

[50] J.E. Jones. On the determination of molecular fields.—i. from the variation of the viscosity of a gas with temperature. *Proceedings of the Royal Society of London. Series A, Containing Papers of a Mathematical and Physical Character*, 106:441–462, 1924.

[51] S.-J. Park and M.-K. S. Intermolecular force. *Interface Science and Technology*, 18:1–57, 2011.

[52] J.D. Weeks, D. Chandler, and H.C. Andersen. Role of repulsive forces in determining the equilibrium structure of simple liquids. *The Journal of Chemical Physics*, 54:5237–5247, 1971.

[53] N.A. Seaton and E.D. Glandt. Aggregation and percolation in a system of adhesive spheres. *The Journal of Chemical Physics*, 86:4668–4677, 1987.

[54] H.J.C. Berendsen and W.F. Van Gunsteren. Practical algorithms for dynamic simulations. In *Molecular-dynamics simulation of statistical-mechanical systems*, pages 43–65. Elsevier, Amsterdam, 1986.

[55] T. Pang. An introduction to computational physics, 2012.

[56] J. Jung, W. Nishima, M. Daniels, G. Bascom, C. Kobayashi, A. Adedoyin, M. Wall, A. Lappala, D. Phillips, W. Fischer, et al. Scaling molecular dynamics beyond 100,000 processor cores for large-scale biophysical simulations. *Journal of Computational Chemistry*, 40:1919–1930, 2019.

[57] P.P. Ewald. Die Berechnung optischer und elektrostatischer Gitterpotentiale. *Annalen der Physik*, 369:253–287, 1921.

[58] S. Plimpton. Fast parallel algorithms for short-range molecular dynamics. *Journal of Computational Physics*, 117:1–19, 1995.

[59] A.W. Lees and S.F. Edwards. The computer study of transport processes under extreme conditions. *Journal of Physics C: Solid State Physics*, 5:1921, 1972.

[60] J.F. Morris. A review of microstructure in concentrated suspensions and its implications for rheology and bulk flow. *Rheologica Acta*, 48:909–923, 2009.

[61] D. Müllner et al. fastcluster: Fast hierarchical, agglomerative clustering routines for R and Python. *Journal of Statistical Software*, 53:1–18, 2013.

[62] C.D. Lorenz and R.M. Ziff. Precise determination of the critical percolation threshold for the three-dimensional "swiss cheese" model using a growth algorithm. *The Journal of Chemical Physics*, 114:3659–3661, 2001.

[63] J. Škvor, I. Nezbeda, I. Brovchenko, and A. Oleinikova. Percolation transition in fluids: Scaling behavior of the spanning probability functions. *Physical Review Letters*, 99:127801, 2007.

[64] A. Geiger and H.E. Stanley. Tests of universality of percolation exponents for a three-dimensional continuum system of interacting waterlike particles. *Physical Review Letters*, 49:1895, 1982.

[65] S.A. Safran, I. Webman, and G.S. Grest. Percolation in interacting colloids. *Physical Review A*, 32:506, 1985.

[66] N. Johner, C. Grimaldi, I. Balberg, and P. Ryser. Transport exponent in a three-dimensional continuum tunneling-percolation model. *Physical Review B*, 77:174204, 2008.

[67] J.-F. Thovert, V.V. Mourzenko, and P.M. Adler. Percolation in three-dimensional fracture networks for arbitrary size and shape distributions. *Physical Review E*, 95:042112, 2017.

[68] M.D. Rintoul and S. Torquato. Precise determination of the critical threshold and exponents in a three-dimensional continuum percolation model. *Journal of Physics A: Mathematical and General*, 30:L585, 1997.

[69] M.E.J. Newman and R.M. Ziff. Efficient monte carlo algorithm and high-precision results for percolation. *Physical Review Letters*, 85:4104, 2000.

[70] B. Nigro, D. Ambrosetti, C. Grimaldi, T. Maeder, and P. Ryser. Transport properties of nonhomogeneous segregated composites. *Physical Review B*, 83:064203, 2011.

[71] D.C. Kozen. Depth-first and breadth-first search. In *The Design and Analysis of Algorithms*, pages 19–24. Springer, New York, 1992.

[72] M.A. Miller. On structural correlations in the percolation of hard-core particles. *The Journal of Chemical Physics*, 131:066101, 2009.

[73] F. Coupette, A. Härtel, and T. Schilling. Continuum percolation expressed in terms of density distributions. *Physical Review E*, 101:062126, 2020.

[74] U. Alon, I. Balberg, and A. Drory. New, heuristic, percolation criterion for continuum systems. *Physical Review Letters*, 66:2879, 1991.

[75] J. Bławzdziewicz and G. Szamel. Structure and rheology of semidilute suspension under shear. *Physical Review E*, 48:4632, 1993.

[76] V. Choudhary and A. Gupta. Polymer/carbon nanotube nanocomposites. *Carbon nanotubes-polymer nanocomposites*, 2011:65–90, 2011.

[77] Z. Spitalsky, D. Tasis, K. Papagelis, and C. Galiotis. Carbon nanotube–polymer composites: chemistry, processing, mechanical and electrical properties. *Progress in Polymer Science*, 35:357–401, 2010.

[78] M.K. Lyon, D.W. Mead, R.E. Elliott, and L.G. Leal. Structure formation in moderately concentrated viscoelastic suspensions in simple shear flow. *Journal of Rheology*, 45:881–890, 2001.

[79] D. Won and C. Kim. Alignment and aggregation of spherical particles in viscoelastic fluid under shear flow. *Journal of Non-Newtonian Fluid Mechanics*, 117:141–146, 2004.

[80] J.M. Brader and M. Krüger. Density profiles of a colloidal liquid at a wall under shear flow. *Molecular Physics*, 109:1029–1041, 2011.

[81] J.J. Gray and R.T. Bonnecaze. Rheology and dynamics of sheared arrays of colloidal particles. *Journal of Rheology*, 42(5):1121–1151, 1998.

[82] P.G. de Gennes. Conjectures on the transition from poiseuille to plug flow in suspensions. *Journal de Physique*, 40:783–787, 1979.

[83] S. Gallier, E. Lemaire, F. Peters, and L. Lobry. Percolation in suspensions and de gennes conjectures. *Physical Review E*, 92:020301, 2015.

[84] K. Thøgersen, M. Dabrowski, and A. Malthe-Sørenssen. Transient cluster formation in sheared non-brownian suspensions. *Physical Review E*, 93:022611, 2016.

[85] J.K.G. Dhont. *An introduction to dynamics of colloids*. Elsevier, Amsterdam, 1996.

[86] N.J. Wagner. The smoluchowski equation for colloidal suspensions developed and analyzed through the generic formalism. *Journal of Non-Newtonian Fluid Mechanics*, 96:177–201, 2001.

[87] R. Abe. On the kirkwood superposition approximation. *Progress of Theoretical Physics*, 21: 421–430, 1959.

[88] J.K.G Dhont and H. Verduin. The effect of shear-flow on critical correlations in colloidal systems: Microstructure, turbidity, and dichroism. *The Journal of Chemical Physics*, 101: 6193–6205, 1994.

[89] T. Ohtsuki. Dynamical properties of strongly interacting brownian particles: 1. dynamic shear viscosity. *Physica A: Statistical Mechanics and its Applications*, (2-3):441–458, 1981.

[90] S.A. Rice and J. Lekner. On the equation of state of the rigid-sphere fluid. *The Journal of Chemical Physics*, 42:3559–3565, 1965.

[91] E. Nazockdast and J.F. Morris. Microstructural theory and the rheology of concentrated colloidal suspensions. *Journal of Fluid Mechanics*, 713:420, 2012.

[92] J.F. Schwarzl and S. Hess. Shear-flow-induced distortion of the structure of a fluid: Application of a simple kinetic equation. *Physical Review A*, 33:4277, 1986.

[93] G. Szamel. Nonequilibrium structure and rheology of concentrated colloidal suspensions: Linear response. *The Journal of Chemical Physics*, 114:8708–8717, 2001.

[94] L. Banetta and A. Zaccone. Radial distribution function of lennard-jones fluids in shear flows from intermediate asymptotics. *Physical Review E*, 99:052606, 2019.

[95] J.K.G. Dhont. On the distortion of the static structure factor of colloidal fluids in shear flow. *Journal of Fluid Mechanics*, 204:421–431, 1989.

[96] W.B. Russel and A.P. Gast. Nonequilibrium statistical mechanics of concentrated colloidal dispersions: Hard spheres in weak flows. *The Journal of Chemical Physics*, 84:1815–1826, 1986.

[97] N.J. Wagner and W.B. Russel. Nonequilibrium statistical mechanics of concentrated colloidal dispersions: hard spheres in weak flows with many-body thermodynamic interactions. *Physica A: Statistical Mechanics and its Applications*, 155:475–518, 1989.

[98] N. Wax. *Selected papers on noise and stochastic processes.* Courier Dover Publications, Mineola, 1954.

[99] L.E. Reichl. *A modern course in statistical physics.* American Association of Physics Teachers, Maryland, 1999.

[100] R.P. Brent. *Algorithms for minimization without derivatives.* Courier Corporation, Mineola, 2013.

[101] M. Doi. *Soft matter physics.* Oxford University Press, Oxford, 2013.

[102] DE Elrick. Source functions for diffusion in uniform shear flow. *Australian Journal of Physics*, 15:283–288, 1962.

[103] J.F. Brady. Computer simulation of viscous suspensions. *Chemical Engineering Science*, 56: 2921–2926, 2001.

[104] J. Vermant and M.J. Solomon. Flow-induced structure in colloidal suspensions. *Journal of Physics: Condensed Matter*, 17:187, 2005.

[105] V.I. Lebedev. Quadratures on a sphere. *USSR Computational Mathematics and Mathematical Physics*, 16:10–24, 1976.

[106] D. Ronis. Theory of fluctuations in colloidal suspensions undergoing steady shear flow. *Physical Review A*, 29:1453, 1984.

[107] H.C. Andersen, J.D. Weeks, and D. Chandler. Relationship between the hard-sphere fluid and fluids with realistic repulsive forces. *Physical Review A*, 4:1597, 1971.

[108] H. Arkın and W. Janke. Gyration tensor based analysis of the shapes of polymer chains in an attractive spherical cage. *The Journal of Chemical Physics*, 138:054904, 2013.

[109] R. Schueler, J. Petermann, K. Schulte, and H.-P. Wentzel. Agglomeration and electrical percolation behavior of carbon black dispersed in epoxy resin. *Journal of Applied Polymer Science*, 63:1741–1746, 1997.

[110] J. Yuan, A. Luna, W. Neri, C. Zakri, T. Schilling, A. Colin, and P. Poulin. Graphene liquid crystal retarded percolation for new high-k materials. *Nature Communications*, 6:1–8, 2015.

[111] S.P. Finner, I. Pihlajamaa, and P. van der Schoot. Geometric percolation of hard nanorods: The interplay of spontaneous and externally induced uniaxial particle alignment. *The Journal of Chemical Physics*, 152:064902, 2020.

[112] A.R. Khokhlov and A.N. Semenov. Influence of external field on the liquid-crystalline ordering in the solutions of stiff-chain macromolecules. *Macromolecules*, 15:1272–1277, 1982.

[113] R.H.J. Otten and P. van der Schoot. Connectedness percolation of elongated hard particles in an external field. *Physical Review Letters*, 108:088301, 2012.

[114] A.P. Chatterjee. Percolation in polydisperse systems of aligned rods: A lattice-based analysis. *The Journal of Chemical Physics*, 140:204911, 2014.

[115] S.P. Finner, M.I. Kotsev, M.A. Miller, and P. van der Schoot. Continuum percolation of polydisperse rods in quadrupole fields: Theory and simulations. *The Journal of Chemical Physics*, 148:034903, 2018.

[116] L. Onsager. The effects of shape on the interaction of colloidal particles. *Annals of the New York Academy of Sciences*, 51:627–659, 1949.

[117] D. Frenkel. Onsager's spherocylinders revisited. *Journal of Physical Chemistry*, 91:4912–4916, 1987.

[118] S. Varga, G. Kronome, and I. Szalai. External field induced tricritical phenomenon in the isotropicnematic phase transition of hard non-spherical particle systems. *Molecular Physics*, 98:911–915, 2000.

[119] S. Szalai, G. Varga, and I. Jackson. External field induced paranematic–nematic phase transitions in rod-like systems. *Molecular Physics*, 93:377–387, 1998.

[120] J. Herzfeld, A.E. Berger, and J.W. Wingate. A highly convergent algorithm for computing the orientation distribution functions of rodlike particles. *Macromolecules*, 17:1718–1723, 1984.

[121] G.J. Vroege and H.N.W. Lekkerkerker. Phase transitions in lyotropic colloidal and polymer liquid crystals. *Reports on Progress in Physics*, 55:1241, 1992.

[122] T. Drwenski, S. Dussi, M. Dijkstra, R. van Roij, and P. van der Schoot. Connectedness percolation of hard deformed rods. *The Journal of Chemical Physics*, 147:224904, 2017.

[123] T. Schilling, M.A. Miller, and P. van der Schoot. Percolation in suspensions of hard nanoparticles: From spheres to needles. *Europhysics Letters*, 111:56004, 2015.

[124] R.F. Kayser Jr. and H.J. Raveché. Bifurcation in onsager's model of the isotropic-nematic transition. *Physical Review A*, 17:2067, 1978.

[125] S.P. Finner, T. Schilling, and P. van der Schoot. Connectivity, not density, dictates percolation in nematic liquid crystals of slender nanoparticles. *Physical Review Letters*, 122: 097801, 2019.

[126] J.P. Straley. Frank elastic constants of the hard-rod liquid crystal. *Physical Review A*, 8: 2181, 1973.

[127] J.D. Parsons. Nematic ordering in a system of rods. *Physical Review A*, 19:1225, 1979.

[128] S.-D. Lee. The onsager-type theory for nematic ordering of finite-length hard ellipsoids. *The Journal of Chemical Physics*, 89:7036–7037, 1988.

[129] D.C. Williamson. The isotropic-nematic phase transition: the onsager theory revisited. *Physica A: Statistical Mechanics and its Applications*, 220:139–164, 1995.

[130] M.A. Cotter. Hard-rod fluid: scaled particle theory revisited. *Physical Review A*, 10:625, 1974.

[131] H.N.W. Lekkerkerker and R. Tuinier. Depletion interaction. In *Colloids and the Depletion Interaction*, pages 197–205. Springer, Dordrecht, 2011.

[132] S.P. Finner, A. Atashpendar, T. Schilling, and P. van der Schoot. Unusual geometric percolation of hard nanorods in the uniaxial nematic liquid crystalline phase. *Physical Review E*, 100:062129, 2019.

[133] R. Tuinier, T. Taniguchi, and H.H. Wensink. Phase behavior of a suspension of hard spherocylinders plus ideal polymer chains. *The European Physical Journal E*, 23:355–365, 2007.

[134] G. Kwon, Y. Heo, K. Shin, and B. J. Sung. Electrical percolation networks of carbon nanotubes in a shear flow. *Physical Review E*, 85:011143, 2012.

[135] C. Koning, M.-C. Hermant, and N. Grossiord. *Polymer carbon nanotube composites: the polymer latex concept*. CRC Press, Boca Raton, 2012.

[136] I.T. Kim, A. Tannenbaum, and R. Tannenbaum. Anisotropic conductivity of magnetic carbon nanotubes embedded in epoxy matrices. *Carbon*, 49:54–61, 2011.

[137] J.M. Brader and M. Schmidt. Nonequilibrium ornstein-zernike relation for brownian many-body dynamics. *The Journal of Chemical Physics*, 139:104108, 2013.

[138] C.M. Fortuin and P.W. Kasteleyn. On the random-cluster model: I. introduction and relation to other models. *Physica*, 57(4):536–564, 1972.

[139] A. Drory. Theory of continuum percolation. i. general formalism. *Physical Review E*, 54: 5992, 1996.

[140] T. Tomé and M.J. de Oliveira. Dynamic phase transition in the kinetic ising model under a time-dependent oscillating field. *Physical Review A*, 41:4251, 1990.

[141] W. Klein. Potts-model formulation of continuum percolation. *Physical Review B*, 26:2677, 1982.

[142] Kevin Cole, James Beck, A Haji-Sheikh, and Bahman Litkouhi. *Heat conduction using Greens functions*. Taylor & Francis, New York, 2010.

[143] D.G. Duffy. *Green's functions with applications*. CRC Press, Boca Raton, 2015.

[144] A. Celzard, E. McRae, C. Deleuze, M. Dufort, G. Furdin, and J.F. Marêché. Critical concentration in percolating systems containing a high-aspect-ratio filler. *Physical Review B*, 53:6209, 1996.

[145] I. Balberg, N. Binenbaum, and N. Wagner. Percolation thresholds in the three-dimensional sticks system. *Physical Review Letters*, 52:1465, 1984.

[146] V.I. Lebedev and D.N. Laikov. A quadrature formula for the sphere of the 131st algebraic order of accuracy. In *Doklady Mathematics*, volume 59, pages 477–481, 1999.

[147] H.H.H. Homeier, S. Rast, and H. Krienke. Iterative solution of the ornstein-zernike equation with various closures using vector extrapolation. *Computer Physics Communications*, 92: 188–202, 1995.

Appendix A

Derivation of equation 4.10

To derive Eq. (4.10), and the boundary condition (4.11), we start with the many body Smoluchowski equation. As in the main text, we define $P_N(\mathbf{r}_1, \ldots, \mathbf{r}_N, t)$ to be the probability density function of N particles at time t. Ignoring all hydrodynamic interactions between the particles, we can write down the many-body Smoluchowski equation [85]

$$\frac{\partial P_N}{\partial t} = \sum_{i=1}^{N} \nabla_i \cdot \left(D_0 \nabla_i P_N + D_0 \beta P_N \nabla_i \Psi - \Gamma \cdot \mathbf{r}_i P_N \right), \tag{A.1}$$

where $D_0 = k_B T / 3\pi D\eta$ is the self-diffusion constant of the particles, $\beta = (k_B T)^{-1}$ is the inverse thermal energy, ∇_i is the gradient operator with respect to $\mathbf{r}_i$, and Ψ is the potential energy, which we assume to be pair-wise additive

$$\Psi(\mathbf{r}_1, \ldots, \mathbf{r}_N) = \sum_{i=1}^{N} \sum_{j>i}^{N} U(\mathbf{r}_i, \mathbf{r}_j), \tag{A.2}$$

where $U(\mathbf{r}_i, \mathbf{r}_j)$ is the pair potential between particles i and j. As mentioned in the main text, the Smoluchowski equation (A.1) describes the time-dependent N-body probability density function $P_N(\mathbf{r}_1, \ldots, \mathbf{r}_N, t)$ of interacting particles on Brownian time scales. In the context of percolation criterion described in the previous section, we are interested in finding the pair correlation function, which relates the 1-body with the 2-body probability density functions.

$$g(\mathbf{r}_1, \mathbf{r}_2, t) = \frac{P_2(\mathbf{r}_1, \mathbf{r}_2, t)}{P_1(\mathbf{r}_1, t) P_1(\mathbf{r}_2, t)} \tag{A.3}$$

It essentially measures to what extend pairs of particle positions are correlated, hence its name. The 1- and 2-body functions can be reduced from their N-body counterpart as

$$P_1(\mathbf{r}_1, t) = \int \mathrm{d}\mathbf{r}_2 \ldots \mathrm{d}\mathbf{r}_N P_N(\mathbf{r}_1, \ldots, \mathbf{r}_N, t), \tag{A.4}$$

$$P_2(\mathbf{r}_1, \mathbf{r}_2, t) = \int \mathrm{d}\mathbf{r}_3 \ldots \mathrm{d}\mathbf{r}_N P_N(\mathbf{r}_1, \ldots, \mathbf{r}_N, t), \tag{A.5}$$

where we integrate over all of three-dimensional space for each particle position. Now, to obtain an equation for the two particle probability function, we integrate the full Smoluchowski equation

(A.1) over the positions of particles $3, \ldots, N$, of which we present the result term by term.

Firstly, the time derivative part simplifies to

$$\int \mathrm{d}\mathbf{r}_3 \ldots \mathrm{d}\mathbf{r}_N \frac{\partial P_N}{\partial t} = \frac{\partial P_2}{\partial t}. \tag{A.6}$$

Secondly, we have

$$\int \mathrm{d}\mathbf{r}_3 \ldots \mathrm{d}\mathbf{r}_N \sum_{i=1}^{N} \nabla_i \cdot (D_0 \nabla_i P_N) = D_0 \nabla_1^2 P_2 + D_0 \nabla_2^2 P_2, \tag{A.7}$$

for the diffusion term, since we assumed that D_0 is a positionally independent scalar. Thirdly, we have

$$\int \mathrm{d}\mathbf{r}_3 \ldots \mathrm{d}\mathbf{r}_N \sum_{i=1}^{N} \nabla_i \cdot (D_0 \beta P_N \nabla_i \Psi) \tag{A.8}$$

$$= \beta D_0 \nabla_1 \cdot (P_2 \nabla_1 U(\mathbf{r}_1, \mathbf{r}_2)) + \beta D_0 \nabla_2 \cdot (P_2 \nabla_2 U(\mathbf{r}_1, \mathbf{r}_2)) \tag{A.9}$$

$$+ \beta D_0 (N-2) \left(\nabla_1 \cdot \int \mathrm{d}\mathbf{r}_3 P_3 \nabla_1 U(\mathbf{r}_1, \mathbf{r}_3) + \nabla_2 \cdot \int \mathrm{d}\mathbf{r}_3 P_3 \nabla_2 U(\mathbf{r}_2, \mathbf{r}_3) \right), \tag{A.10}$$

for the interaction term, and lastly,

$$\int \mathrm{d}\mathbf{r}_3 \ldots \mathrm{d}\mathbf{r}_N \sum_{i=1}^{N} \nabla_i \cdot (\Gamma \cdot \mathbf{r}_i P_N) = \nabla_1 \cdot (\Gamma \cdot \mathbf{r}_1 P_2) + \nabla_2 \cdot (\Gamma \cdot \mathbf{r}_2 P_2), \tag{A.11}$$

for the flow term.

We can proceed by assuming that we have a homogeneous system such that a global translation leaves all functions invariant. It is now easy to show that $P_1(\mathbf{r}_1, t) = 1/V$, since $\int \mathrm{d}\mathbf{r}_1 P_1(\mathbf{r}_1, t) = 1$. We perform a global translation such that $\mathbf{r}_2$ lies at the origin. In order to simplify the equations, we also define two relative coordinates $\mathbf{r} = \mathbf{r}_1 - \mathbf{r}_2$ and $\mathbf{r}' = \mathbf{r}_3 - \mathbf{r}_2$, such that $\nabla_1 = \nabla$ and $\nabla_2 = -\nabla - \nabla'$. Additionally, we assume that all three-body interactions and correlations are negligible by letting the density $\rho \to 0$. We now find the more simple equation for the pair correlation function $g(\mathbf{r}_1, \mathbf{r}_2, t) = g(\mathbf{r}, \mathbf{0}, t) \equiv g(\mathbf{r}, t)$

$$\frac{\partial g}{\partial t} = 2D_0 \nabla^2 g + 2D_0 \beta \nabla \cdot (g \nabla U) - \nabla \cdot (\Gamma \cdot \mathbf{r}\, g). \tag{A.12}$$

We are primarily interested in the shear-induced distortion of the equilibrium pair correlations function, since we have a successful theory of the latter. To that end, we divide the pair correlation function in an equilibrium part and a distortion $g(\mathbf{r}, t) = g_0(\mathbf{r}, t) + \delta g(\mathbf{r}, t)$. The equilibrium pair correlation function is the solution to Eq. (A.12) in the absence of a flow field

$$\frac{\partial g_0}{\partial t} = 2D_0 \nabla^2 g_0 + 2D_0 \beta \nabla \cdot (g_0 \nabla U). \tag{A.13}$$

By substitution, we find an equation for δg

$$\frac{\partial \delta g}{\partial t} = 2D_0 \nabla^2 \delta g + 2D_0 \beta \nabla \cdot (\delta g \nabla U) - \nabla \cdot (\Gamma \cdot \mathbf{r}\, g_0) - \nabla \cdot (\Gamma \cdot \mathbf{r}\, \delta g). \tag{A.14}$$

To simplify this further, we note that $g_0 = \exp(-\beta U)$ is a the steady state solution of Eq. (A.13), which we can use to close Eq. (A.14). This sets the equilibrium pair distribution function to equal a step function in the case of hard-core interactions. The fact that this is a solution of the equation for the equilibrium distribution function stems from the fact that we threw away all 3+ body interactions. In a real system, this is an approximation that becomes exact in the dilute limit, as $\rho \to 0$. However, at higher densities, it introduces an error in our predictions. A higher order approximation could in principle be used to close the equations, but we do not pursue this in the present work.

Since we are considering hard core particles, we can now write Eq. (A.14) as a boundary value problem, with a no-flux boundary condition given by

$$\begin{aligned} \frac{\partial \delta g}{\partial t} &= 2D_0 \nabla^2 \delta g - \dot{\gamma} y \frac{\partial \delta g}{\partial x} && r > D, \\ 2D_0 \frac{\partial \delta g}{\partial r} &= \dot{\gamma} \frac{xy}{r} (\delta g + 1) && r = D, \end{aligned} \tag{A.15}$$

where we used $\nabla \cdot (\Gamma \cdot \mathbf{r} g) = \dot{\gamma} y \frac{\partial g}{\partial x}$. The equation we are left with is a diffusion equation with an extra convective term that captures the effect of the flow field. The boundary condition arises from requirement that there be no mass flux at contact of two particles

$$\hat{\mathbf{r}} \cdot [2D_0 \nabla \delta g + 2D_0 \beta \nabla \cdot (\delta g \nabla U) - \dot{\gamma} y \hat{\mathbf{x}} (g_0 + \delta g)] = 0 \qquad r = D^+, \tag{A.16}$$

where the second term vanishes due to the fact that $\nabla U = 0$ for all $\mathbf{r}$, except at $\mathbf{r} = D$, in the case of hard spheres. We find Eq. (4.10) by taking the stationary variant of Eq. (A.15), by setting $\partial / \partial t = 0$.

Appendix B

Solution of equation 4.12

We dedicate this appendix to finding the solution of the dimensionless equation (4.12), and the accompanying boundary condition (4.13). However, instead of starting with the steady-state equation, it turns out to be easier to start with the time dependent equation, and taking the steady state limit later. Therefore, we start with

$$\begin{aligned} \frac{\partial \delta g'}{\partial t'} - \nabla'^2 \delta g' + y' \frac{\partial \delta g'}{\partial x'} = 0 \qquad & r' > \sqrt{2\mathrm{Pe}}, \\ \frac{\partial \delta g'}{\partial r'} - \frac{x'y'}{r'}(\delta g' + 1) = 0 \qquad & r' = \sqrt{2\mathrm{Pe}}, \end{aligned} \tag{B.1}$$

where we have defined the Peclet number $\mathrm{Pe} = \dot{\gamma} D^2 / 4D_0$. We can make the convective term in the equation simpler to deal with using another change of variables

$$\begin{aligned} & u = x' - y't' \qquad v = y' \qquad w = z' \qquad s = t' \\ & \theta(u, v, w, s) = \delta g'(x' - y't', y', z', t'), \end{aligned} \tag{B.2}$$

such that

$$\nabla'^2 = (1 - s^2)\frac{\partial^2}{\partial u^2} - 2s\frac{\partial^2}{\partial u \partial v} + \frac{\partial^2}{\partial v^2} + \frac{\partial^2}{\partial w^2}, \qquad \text{and} \qquad \frac{\partial}{\partial t'} = \frac{\partial}{\partial s} - v\frac{\partial}{\partial u}. \tag{B.3}$$

Eq. (B.1) now simplifies to

$$\frac{\partial \theta}{\partial s} = (1 + s^2)\frac{\partial^2 \theta}{\partial^2 u} + \frac{\partial^2 \theta}{\partial v^2} + \frac{\partial^2 \theta}{\partial w^2} - 2s\frac{\partial^2 \theta}{\partial v \partial u}. \tag{B.4}$$

We deal with the boundary conditions when we transform the solution back to our original dimensionless coordinates. This new equation is most easily solved in the Fourier domain. Therefore, we define the spatial Fourier transform and its inverse

$$\hat{\theta}(\xi, \eta, \zeta, s) = \iiint \mathrm{d}u\mathrm{d}v\mathrm{d}w\, \theta(u, v, w, s) e^{i(\xi u + \eta v + \zeta w)} \tag{B.5}$$

$$\theta(u, v, w, s) = \frac{1}{(2\pi)^3} \iiint \mathrm{d}\xi\mathrm{d}\eta\mathrm{d}\zeta\, \hat{\theta}(\xi, \eta, \zeta, s) e^{-i(\xi u + \eta v + \zeta w)}, \tag{B.6}$$

where all integrals range from $-\infty$ to ∞, such that equation (B.4) reads in the Fourier domain

$$\frac{\partial \hat{\theta}}{\partial s} = -\left(\xi^2+\eta^2+\zeta^2\right)\hat{\theta} + 2\xi\eta s\hat{\theta} - \xi^2 s^2\hat{\theta}, \tag{B.7}$$

which can be readily solved:

$$\hat{\theta}(\xi,\eta,\zeta,s) = \hat{\theta}(\xi,\eta,\zeta,0)\exp\left[-\left(\xi^2+\eta^2+\zeta^2\right)s + \xi\eta s^2 - \frac{1}{3}\xi^2 s^3\right]. \tag{B.8}$$

Here, $\hat{\theta}(\xi,\eta,\zeta,0)$ is given by the Fourier Transform of the initial configuration. To simplify notation, we introduce the function

$$\hat{G}(\xi,\eta,\zeta,s) = \exp\left[-\left(\xi^2+\eta^2+\zeta^2\right)s + \xi\eta s^2 - \frac{1}{3}\xi^2 s^3\right], \tag{B.9}$$

such that real space solution of (B.4) is given by the convolution product of $\theta(u,v,w,0)$ and $\theta(u,v,w,s)$

$$\theta(u,v,w,s) = \theta(u,v,w,0) * G(u,v,w,s) \tag{B.10}$$

$$= \iiint G(u-u',v-v',w-w',s)\theta(u',v',w',0)\mathrm{d}u'\mathrm{d}v'\mathrm{d}w'\mathrm{d}s', \tag{B.11}$$

where $*$ denotes the convolution operation and $G(u,v,w,s)$ is determined with the inverse Fourier transform of $\hat{G}$ to be

$$G(u,v,w,s) = \frac{1}{4}\left(\frac{1}{s\pi}\right)^{3/2}\sqrt{\frac{3}{s^2+12}}\exp\left(-\frac{v^2}{4s} - \frac{w^2}{4s} - \frac{3(2u+vs)^2}{4s(s^2+12)}\right). \tag{B.12}$$

The function $G(u,w,v,s)$ satisfies Eq. (B.4) without boundary conditions and subject to the initial condition $\theta(u,v,w,0) = \delta(u)\delta(v)\delta(w)$, which is equivalent to saying that it satisfies Eq. (B.4) with delta peak centred at $u=v=w=s=0$ as source term

$$\frac{\partial G}{\partial s} - (1+s^2)\frac{\partial^2 G}{\partial^2 u} - \frac{\partial^2 G}{\partial v^2} - \frac{\partial^2 G}{\partial w^2} + 2s\frac{\partial^2 G}{\partial v \partial u} = \delta(0,0,0,0) \qquad t \geq 0. \tag{B.13}$$

Therefore, we identify $G(u-u',v-v',w-w',s)$ as a free-space Green's function of Eq. (B.4) [142]. Using the method of images, we can in principle satisfy the boundary condition belonging to Eq. (B.4) by extending the domain of the function θ to all of space and placing source terms inside the region that was not part of its original domain. If we place these source terms such that the linear combination of the solutions that correspond to those sources also satisfies the boundary condition, we have found the solution of the original Eq. (B.4) in its original domain. We note that due to the linearity of the differential operator, any linear combination of solutions must still be a solution to Eq. (B.4).

To solve this equation, we use a variant of the method of images that we call the method of multipole sources [143], which relies on the fact that we can create multipoles by placing several source terms in very close proximity to each other. Using this technique, we place multipole sources in that region to satisfy the boundary conditions. To simplify, we choose to place them all at the origin, which is part of this excluded region. Since a multipole is made of delta sources placed infinitesimally close together with different signs, the solution corresponding to that multipole is equal to the superposition of the Green's functions at the corresponding locations.

This superposition is proportional to a high-order partial derivative of the Green's function in the limit that the sources approach each other. Take a dipole for example, if we place two point sources of strength $\pm 1/h$ at $(u, v, w, s) = (-h, 0, 0, 0)$ and $(0, 0, 0, 0)$, and let $h \to 0$, the solution corresponding to this dipole source becomes

$$\theta(u, v, w, s) = \lim_{h \to 0}(G(u + h, v, w, s) - G(u, v, w, s)/h = \frac{\partial G(u, v, w, s)}{\partial u} . \tag{B.14}$$

Because of the fact that higher order multipoles are created in the same way by superimposing lower order multipole sources, the solutions corresponding to them are all higher order derivatives of the Green's function.

We can thus write the solution of Eq. (B.4) as a linear combination of the functions

$$\theta_{\alpha\beta}(u, v, w, s) = \iiint \delta(u', v', w', s') \left(\frac{\partial}{\partial u'}\right)^{\alpha} \left(\frac{\partial}{\partial v'}\right)^{\beta} \tag{B.15}$$
$$G(u - u', v - v', w - w', s - s')\mathrm{d}u'\mathrm{d}v'\mathrm{d}w'$$
$$= \left(\frac{\partial}{\partial u}\right)^{\alpha} \left(\frac{\partial}{\partial v}\right)^{\beta} G(u, v, w, s), \tag{B.16}$$

where we leave out the multipoles in the w-direction for symmetry reasons (the boundary conditions of (A.15) are independent of z). We can now perform the inverse transformation of Eq. (B.2), and we find that the solution of Eq. (B.1) is given by a linear combination of the functions

$$\delta g'_{\alpha\beta}(x', y', z', t') = \left(\frac{\partial}{\partial x'}\right)^{\alpha} \left(\frac{\partial}{\partial y'} + t' \frac{\partial}{\partial x'}\right)^{\beta} G(x' - t'y', y', z', t'). \tag{B.17}$$

We have now in principle found the solution to the transient boundary value problem (except that we still have to find the values of the coefficients of the linear combination). However, we are interested mainly in the pair correlation function of the fully developed flow, *i.e.* the steady state solution. Using the limit method, we can transform these Green's functions of the transient equations to those of the steady state equations [142]. The result is given by

$$T'_{\alpha\beta}(x', y', z') = \lim_{\tau \to \infty} \int_0^{\tau} \left(\frac{\partial}{\partial x'}\right)^{\alpha} \left(\frac{\partial}{\partial y'} + t' \frac{\partial}{\partial x'}\right)^{\beta} G(x' - t'y', y', z', t')\mathrm{d}t'. \tag{B.18}$$

Summarising, the solution of our dimensionless steady state equation

$$y' \frac{\partial \delta g'}{\partial x'} - \nabla'^2 \delta g' = 0, \tag{B.19}$$

is given by

$$\delta g'(\mathbf{r}') = \sum_{\alpha,\beta=0}^{\infty} C^{\alpha\beta} T'_{\alpha\beta}(\mathbf{r}') \qquad r' > \sqrt{2\mathrm{Pe}}, \tag{B.20}$$

where the coefficients $C^{\alpha\beta}$ are determined by the boundary equation

$$\frac{\partial \delta g'}{\partial r'} - \frac{x'y'}{r'} \delta g' = \sqrt{2\mathrm{Pe}}\, \frac{x'y'}{r'^2} \qquad r' = \sqrt{2\mathrm{Pe}}, \tag{B.21}$$

where $\mathrm{Pe} = \dot{\gamma} D^2 / 4D_0$ is a dimensionless number quantifying the strength of the shear flow with

respect to the diffusivity of the particles.

To determine the coefficients $C^{\alpha\beta}$, we insert Eq. (B.20) into Eq. (B.21), and find

$$\sum_{\alpha,\beta=0}^{\infty} C^{\alpha\beta}\left(\frac{\partial T'_{\alpha\beta}}{\partial r'} - \frac{x'y'}{r'}T'_{\alpha\beta}\right) = \sqrt{2\mathrm{Pe}}\,\frac{x'y'}{r'^2} \qquad r' = \sqrt{2\mathrm{Pe}}. \tag{B.22}$$

We can now expand the term within the brackets in real (valued) spherical harmonics $Y_{lm}(\hat{\mathbf{r}}')$ with coefficients $j^{lm}_{\alpha\beta}$

$$\frac{\partial T'_{\alpha\beta}}{\partial r'} - \frac{x'y'}{r'}T'_{\alpha\beta} = \sum_{l=0}^{\infty}\sum_{m=-l}^{l} j^{lm}_{\alpha\beta}Y_{lm}(\hat{\mathbf{r}}'), \tag{B.23}$$

where the real spherical harmonics are defined in terms of the regular spherical harmonics $\hat{Y}^m_l(\hat{\mathbf{r}}')$ as

$$Y_{lm} = \begin{cases} \frac{i}{\sqrt{2}}\left(\hat{Y}^m_l - (-1)^m\hat{Y}^{-m}_l\right) = \sqrt{2}(-1)^m\Im\left(\hat{Y}^{|m|}_l\right) & m<0 \\ Y^0_l & m=0 \\ \frac{1}{\sqrt{2}}\left(\hat{Y}^{-m}_l + (-1)^m\hat{Y}^m_l\right) = \sqrt{2}(-1)^m\Re\left(\hat{Y}^{|m|}_l\right) & m>0. \end{cases} \tag{B.24}$$

The coefficients $j^{lm}_{\alpha\beta}$ can be determined by multiplying both sides of Eq. (B.23) with the corresponding real spherical harmonic and integrating over all orientations. Due to the orthogonality of the real spherical harmonics, this yields the expansion coefficients

$$j^{lm}_{\alpha\beta} = \int_0^{2\pi}\mathrm{d}\phi\int_0^{\pi}\mathrm{d}\theta\sin(\theta)Y^{lm}(\theta,\phi)\left(\frac{\partial T'_{\alpha\beta}}{\partial r'} - \frac{x'y'}{r'}T'_{\alpha\beta}\right). \tag{B.25}$$

Using the fact that $x'y'/r'^2 = \sqrt{4\pi/15}\,Y_{2,\text{-}2}(\hat{\mathbf{r}}')$, we now find the coefficients $C^{\alpha\beta}$, by writing

$$\sum_{\alpha,\beta=0}^{\infty} C^{\alpha\beta}\sum_{l=0}^{\infty}\sum_{m=-l}^{l} j^{lm}_{\alpha\beta}Y_{lm}(\hat{\mathbf{r}}') = \sqrt{8\pi\mathrm{Pe}/15}\,Y_{2,\text{-}2}(\hat{\mathbf{r}}') \qquad r' = \sqrt{2\mathrm{Pe}}, \tag{B.26}$$

or, more compactly,

$$\sum_{\alpha,\beta=0}^{\infty} C^{\alpha\beta}j^{lm}_{\alpha\beta} = \sqrt{\frac{8\pi\mathrm{Pe}}{15}}\delta_{l,2}\delta_{m,\text{-}2}, \tag{B.27}$$

for all integers $0 \le l < \infty$ and $-l \le m \le l$. Eq. (B.27) is a system of infinitely many linear equations in the coefficients $C^{\alpha\beta}$.

Appendix C

The excluded-volume approximation

In the present work, we use accurate numerical methods to integrate the connectedness Ornstein-Zernike equation. However, in more analytical treatments one has to rely on various approximations to estimate the cluster size. A widely used example is the excluded-volume approximation, where the percolation threshold is given by the inverse of the mean excluded volume [122, 144, 145]. This approximation assumes that the angular averaging of the pair connectedness function g^+ and the direct connectedness function C^+ can be factorised. It reads that the percolation threshold is given by:

$$\rho = \frac{1}{\left\langle\left\langle \hat{C}(0, \mathbf{u}, \mathbf{u}')\right\rangle\right\rangle'}. \tag{C.1}$$

The aim of this section is to evaluate the validity of this approximation by numerically solving Eq. (C.1), and comparing to the full solutions of the Ornstein-Zernike equations. Due to the implicit density dependence of the mean excluded volume, we solve this equation by finding the root numerically. To do this, we use Brent's method [100], which essentially attempts to repeatedly find a better approximation of the root of the equation using quadratic interpolation. We show the results in Fig. C.1. Comparing with the exact results which are presented in Fig. 5.6 and reprinted here, we see that the excluded-volume approximation yields qualitatively very accurate results. It shows the same role of particle alignment on the percolation threshold. Quantitatively however, the approximation underestimates the percolation threshold significantly in the ordered phases. In the isotropic phase, of course the percolation threshold matches the exact values.

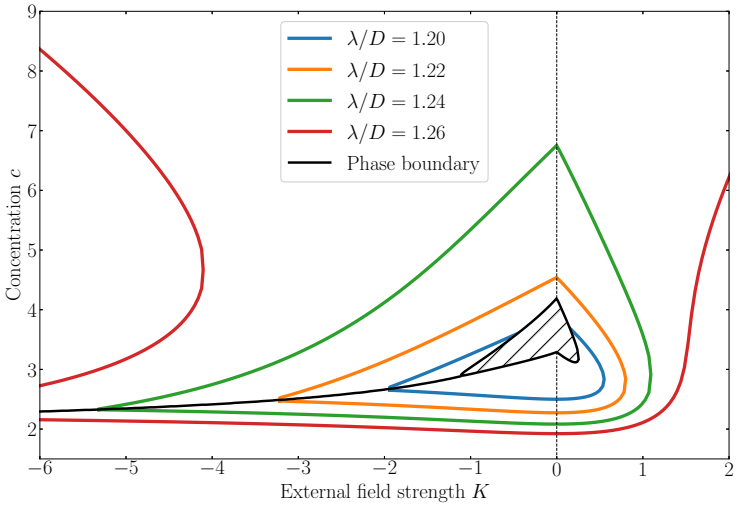

(a)

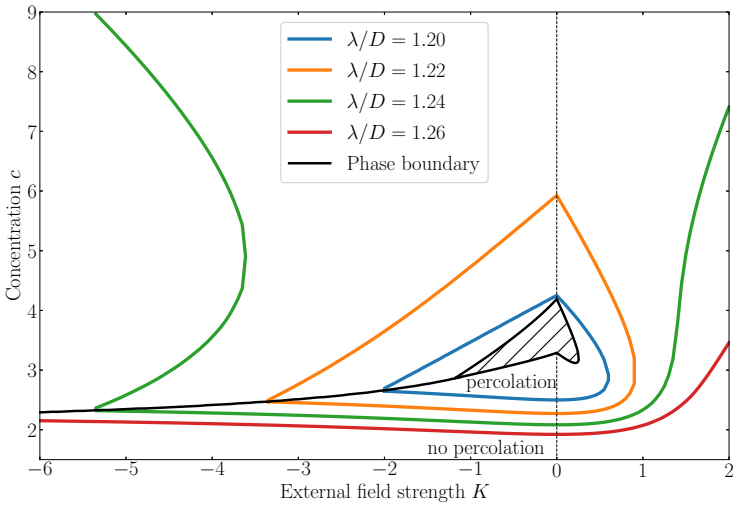

(b)

Figure C.1: *The occurrence of percolation for varying concentration c, external field strength K and connectedness shell thickness λ/D as calculated from (a) the excluded-volume approximation and (b) the full connectedness Ornstein-Zernike equation. Also indicated are the binodals and second order phase transition computed from Onsager theory, see Fig. 5.4.*

Appendix D

Isotropic correlation lengths

In this Appendix, we show that the correlation lengths in the isotropic phase in the limit that $N/V \to 0$ are equal to $L/6$. We start at Eq. (5.21), which in the dilute limit reads

$$\left.\frac{\partial^2 \hat{g}^+(\mathbf{q},\mathbf{u},\mathbf{u}')}{\partial \mathbf{q}\partial \mathbf{q}}\right|_{\mathbf{q}=0} = -\frac{1}{6}(\lambda - D)L^4|\mathbf{u}\times\mathbf{u}'|(\mathbf{u}\,\mathbf{u}+\mathbf{u}'\mathbf{u}') \tag{D.1}$$

where the correlation lengths are now given by

$$\xi^2_{\alpha\beta} = \frac{L^2}{24}\frac{\left\langle\left\langle|\mathbf{u}\times\mathbf{u}'|(\mathbf{u}_\alpha\mathbf{u}_\beta+\mathbf{u}'_\alpha\mathbf{u}'_\beta)\right\rangle\right\rangle'}{\langle\langle|\mathbf{u}\times\mathbf{u}'|\rangle\rangle'}, \tag{D.2}$$

where we predicted in the main text that the cross-correlations vanish. As we know that $\xi_{xx} = \xi_{yy} = \xi_{zz}$, in the isotropic case, we can focus ourselves on the z-component. Therefore, we have

$$\xi^2_{zz} = \frac{L^2}{12}\frac{\iiint \mathrm{d}\phi\mathrm{d}\theta\mathrm{d}\theta' \sin\theta\cos^2\theta|\sin\gamma|}{\iiint \mathrm{d}\phi\mathrm{d}\theta\mathrm{d}\theta' \sin\theta|\sin\gamma|}, \tag{D.3}$$

where the θ-integrations run from 0 to π and the ϕ integration runs from 0 to 2π and

$$|\sin\gamma| = \sqrt{1-(\cos\theta\cos\theta'+\sin\theta\sin\theta'\cos\phi)^2}. \tag{D.4}$$

The two remaining integrals can be evaluated explicitly. We expand the function $|\sin\gamma|$ in terms of Legendre functions $P(\cos\gamma)$ and apply the addition theorem to find,

$$|\sin\gamma| = \sum_{n=1}^{\infty} d_n P_n(\cos\gamma) \tag{D.5}$$

$$= \sum_{n=1}^{\infty} d_n \Bigg(P_n(\cos\theta)P_n(\cos\theta') \tag{D.6}$$

$$+ 2\sum_{m=1}^{n}\frac{(n-1)!}{(m-1)!}P_n^m(\cos\theta)P_n^m(\cos\theta')\cos(m\phi)\Bigg), \tag{D.7}$$

if we integrate our expression of $|\sin\gamma|$ over the domain $0 < \phi < 2\pi$, we see that the last term vanishes due to the presence of the $\cos(m\phi)$, and we find

$$\frac{1}{2\pi}\int_0^{2\pi} \mathrm{d}\phi |\sin\gamma| = \sum_{n=1}^{\infty} d_n P_n(\cos\theta) P_n(\cos\theta'), \tag{D.8}$$

where the first few values of the coefficients d_n were determined by Kayser *et.al.* [124]. In this Appendix, we only need their first value $d_0 = \pi/4$. Using this first term in the expansion of the function $|\sin\gamma|$, we can now write

$$\begin{aligned}\int_0^{\pi} \mathrm{d}\theta \int_0^{\pi} \mathrm{d}\theta' \int_0^{2\pi} \mathrm{d}\phi \sin\theta \sin\theta' |\sin\gamma| \\ = 2\pi \sum_{n=1}^{\infty} d_n \int_0^{\pi} \mathrm{d}\theta \int_0^{\pi} \mathrm{d}\theta' \sin\theta \sin\theta' P_n(\cos\theta) P_n(\cos\theta').\end{aligned} \tag{D.9}$$

Since

$$\int_0^{\pi} \mathrm{d}\theta \sin\theta P_n(\cos\theta) = \begin{cases} 2 & n = 0 \\ 0 & n = 1, 2, 3, \ldots, \end{cases} \tag{D.10}$$

which follows from the orthogonality relations of Legendre polynomials with $P_0(x) = 1$, we find[1]

$$\int_0^{\pi} \mathrm{d}\theta \int_0^{\pi} \mathrm{d}\theta' \int_0^{2\pi} \mathrm{d}\phi \sin\theta \sin\theta' |\sin\gamma| = 2\pi^2. \tag{D.11}$$

Similarly, we have

$$\begin{aligned}\int_0^{\pi} \mathrm{d}\theta \int_0^{\pi} \mathrm{d}\theta' \int_0^{2\pi} \mathrm{d}\phi \sin\theta \sin\theta' \cos^2\theta |\sin\gamma| \\ = 2\pi \sum_{n=1}^{\infty} d_n \int_0^{\pi} \mathrm{d}\theta \int_0^{\pi} \mathrm{d}\theta' \sin\theta \sin\theta' \cos^2\theta P_n(\cos\theta) P_n(\cos\theta').\end{aligned} \tag{D.12}$$

Since

$$\int_0^{\pi} \mathrm{d}\theta \sin\theta \cos^2\theta P_0(\cos\theta) = \frac{2}{3}, \tag{D.13}$$

we find

$$\int_0^{\pi} \mathrm{d}\theta \int_0^{\pi} \mathrm{d}\theta' \int_0^{2\pi} \mathrm{d}\phi \sin\theta \sin\theta' \cos^2\theta |\sin\gamma| = 2\pi \cdot 2 \cdot \frac{2}{3}\frac{\pi}{4} = \frac{2\pi^2}{3}. \tag{D.14}$$

Therefore,

$$\xi_{zz}^2 = \frac{L^2}{12}\frac{\frac{2\pi^2}{3}}{2\pi^2} = \frac{L^2}{36}, \tag{D.15}$$

and thus

$$\xi_{xx} = \xi_{yy} = \xi_{zz} = L/6 \tag{D.16}$$

in the absence of an external field, in the limit that $\rho \to 0$ for any finite connectivity length λ/D.

[1] Of course, this integral is much easier when evaluated directly over the angle γ...

Appendix E

Particle correlations

At this moment in time, a quantitative method of predicting the percolation threshold of (hard) spheres remains elusive, and the pursuit of a good percolation theory is a matter of active research. In contrast to the case of rodlike particles, as described in Chapter 5, closures for connectedness Ornstein-Zernike equation generally do not give accurate agreement with simulations, despite being very accurate for in the structural case. In this appendix, we provide the pair correlation-, connectedness- and blocking functions slightly above and below the percolation threshold for various values of the hard sphere volume fraction for comparison with theory. Additionally, since a fully dynamical percolation theory is also still lacking, we provide the Van Hove function, and its connectedness and blocking part close to the percolation threshold.

In Fig. E.1, we show the pair correlation function $g(r)$, the pair connectedness function g^+ and pair blocking function g^*. We provide these functions slightly below and above the percolation threshold for simulations of $N = 1000$ particles. The particles interact with a standard Weeks-Chandler-Andersen potential (4.22) with $\epsilon_0 = 1$. The rows in Fig. E.1 respectively correspond to number densities $\rho\sigma^3 = (0.0, 0.5, 0.9)$. We see in the case for ideal particles ($\rho\sigma^3 = 0$), that the radial distribution function is always equal to unity. At $r < \lambda$, the connectedness and blocking parts are equal to one and zero respectively. When the radial coordinate is increased to $r = \lambda$, they discontinuously jump to a finite value. When r is increased further, they seem to respectively converge to either zero and one below the percolation threshold or to some finite values above it.

In the second and third rows of Fig. E.1, we show the effect that structural correlations have on this behaviour. At $\rho\sigma^3 = 0.5$, we see that the correlations visible in the radial distribution function are also visible in the connectedness and blocking functions. Pair that have a mutual distance $r < \sigma$ receive a large energy penalty. In this region, we see that $g = g^+ = g^* \approx 0$. If $\sigma < r < \lambda$, the pairs of particle are always connected, and thus we see that $g^+ = g$ and $g^* = 0$. For $r > \lambda$, the functions all depend nontrivially on the radial coordinate and on the density. Similar to the dilute case, it again seems that the connectedness and blocking functions tend to zero and one below the percolation threshold and some finite values above it, when $r/\sigma \to \infty$.

If we are interested not only in instantaneous structural information but also in how structural information is correlated in time, a good quantity to look at is the so-called Van Hove function $G(\mathbf{r}, \Delta t)$. It quantifies the probability one particle found with at position $\mathbf{r}$ at time $t = \Delta t$, given that another particle was located at the origin at time $t = 0$. In the case that the time difference $\Delta t = 0$, the definition of the Van Hove function $G(\mathbf{r}, 0)$ is equivalent to that of the pair correlation function.

Similar to how the pair correlation function can be divided in a connectivity and a blocking

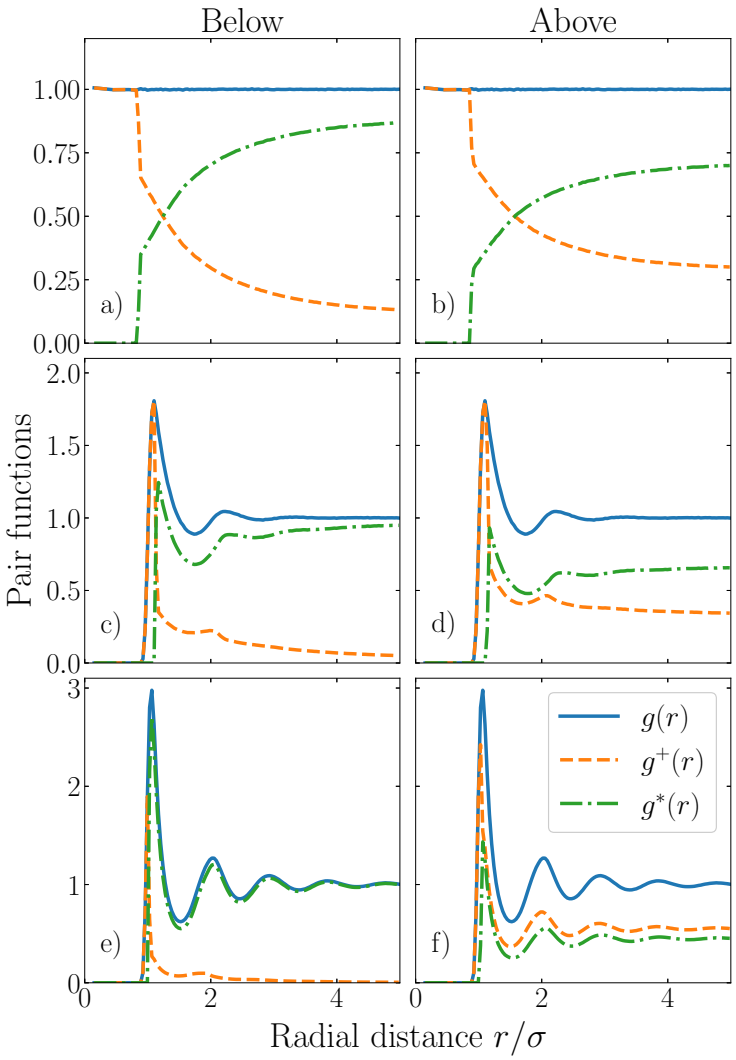

Figure E.1: *The pair correlation function $g(r)$, the pair connectedness function g^+ and pair blocking function g^*, from a simulation with $N = 1000$ particles interacting with the Weeks-Chandler-Andersen potential at number density (a, b) $\rho\sigma^3 = 0$, (c,d) $\rho\sigma^3 = 0.5$, (e,f) $\rho\sigma^3 = 0.9$. The columns correspond to connectivity lengths chosen such that the connectivity volume fraction is slightly below (first column) or above (second column) the percolation threshold. In Figs. (a) and (b), we set $\sigma = 0$, and the horizontal axis is instead given in terms of r/λ, with λ the connectivity length.*

part, we divide the Van Hove function in a connectedness Van Hove function $G^+(\mathbf{r}, \Delta t)$ and a blocking Van Hove function $G^*(\mathbf{r}, \Delta t)$. They correspond to the probability that two particles are found to be connected or disconnected at $t = \Delta t$ and that one of the particles is located at $\mathbf{r}$ at $t = \Delta t$ and the other at the origin at time $t = 0$. With this definition, $G^+(\mathbf{r}, 0) = g^+(\mathbf{r})$ and $G^*(\mathbf{r}, 0) = g^*(\mathbf{r})$. In the case of spherical particles in a homogeneous dispersion, all functions above depend only on the radial distance r.

In Fig. E.2, we show the Van hove functions for the same parameters as chosen in Fig. E.1. In the first row, we show them for ideal particles. We see that the low-r information in the connectedness and blocking functions decays as the time difference is increased. This happens on a timescale of tens or hundredths of simulation time units. As $\Delta t \to \infty$, the functions become constant, and seem to become equal to the $r \to \infty$-limit of g^+ and g^*. In the non-dilute case, we see that the structural correlations disappear on much shorter time scales (a few τ).

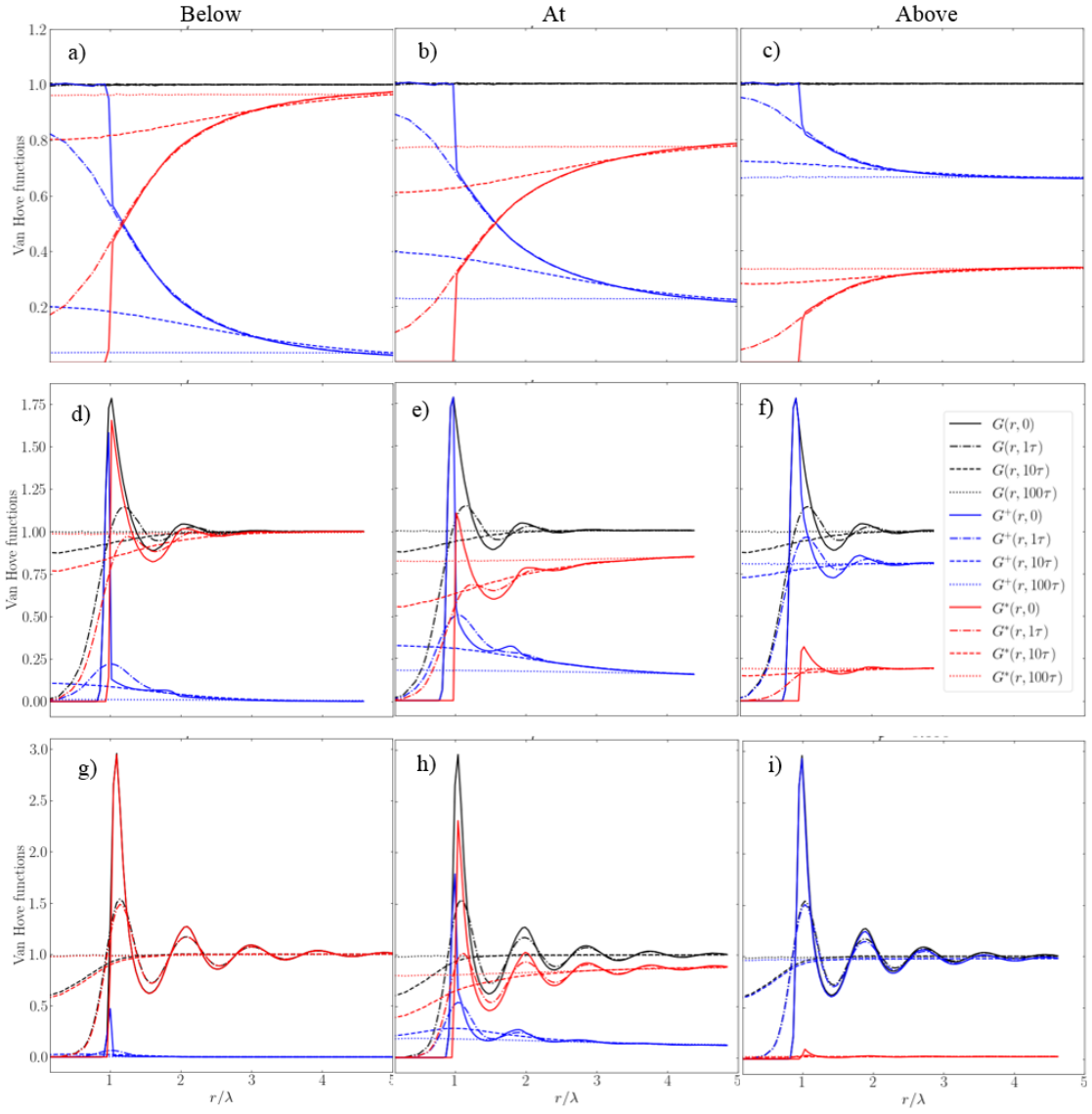

Figure E.2: *The Van Hove function $G(r)$ (black), the connectedness Van Hove function G^+ (blue) and blocking Van Hove function G^* (red), from a simulation with $N = 1000$ particles interacting with the Weeks-Chandler-Andersen potential at number density (a, b, c) $\rho\sigma^3 = 0$, (d, e, f) $\rho\sigma^3 = 0.5$, (g, h, i) $\rho\sigma^3 = 0.9$. The columns correspond to connectivity lengths chosen such that the connectivity volume fraction is slightly below (first column), at (second column) or above (third column) the percolation threshold. The solid lines correspond to a time difference $\Delta t = 0$, and therefore are equal to the data in Fig. E.1. The broken lines correspond to time differences indicated in the legend, where τ is defined as the simulation time unit.*

Appendix F

Numerical procedure

In this appendix, we describe a few of the numerical procedures used in the text. We start by giving a brief overview of the Lebedev quadrature, which is used to accurately integrate over the surface of a sphere. Subsequently, we describe the numerical procedure that we invoke to solve Eq. (4.12). Lastly, we describe a numerical integration method to solve the Ornstein-Zernike equation with the Percus-Yevick closure.

F.1 Lebedev quadrature

The Lebedev quadrature is a numerical scheme for approximating the integral of some function f over the unit sphere [105]

$$I = \int_{\theta=0}^{\pi} \int_{\phi=0}^{2\pi} f(\theta, \phi) \sin\theta \mathrm{d}\theta \mathrm{d}\phi \approx \sum_{i=0}^{N} f(\theta_i, \phi_i) w_i. \tag{F.1}$$

Lebedev proposed that the points $\mathbf{u}_i = \{\theta_i, \phi_i\}$ and weights $\{w_i\}$ can be found by imposing octahedral symmetry, and requiring that the approximation (F.1) is exact for all spherical harmonics $Y_l^m(\theta, \phi)$ up to order l, where $-l \leq m \leq l$ This is equivalent to requiring that the integration is exact for all three-dimensional polynomials up to degree l. The latter condition results in a system of nonlinear algebraic equations that must be solved for the weights w_i. The points and weights have been tabulated up to order 131 [146]. An example of the distribution of points is shown in Fig. F.1. The scheme of order 131 has a discretisation with 5810 gridpoints.

(a) **(b)**

Figure F.1: *Distribution of grid points of the Lebedev quadrature of order 23 (a) and 131 (b), which is used for integration on a spherical surface.*

F.2 Numerical solution procudure for Eq. (4.12)

In this appendix, we outline the numerical method we use to determine the radial distribution function in simple shear.

We solve equation (4.12) writing its solution as a linear combination of derivatives of the free space Green's functions given by equation (B.12). For reference, these multipole sources functions are reprinted here.

$$\delta g'_{\alpha\beta}\left(x',y',z',t'\right)=\left(\frac{\partial}{\partial x'}\right)^{\alpha}\left(\frac{\partial}{\partial y'}-t'\frac{\partial}{\partial x'}\right)^{\beta}G\left(x'+t'y',y',z',t'\right), \tag{F.2}$$

where

$$G\left(u,v,w,s\right)=\frac{1}{4}\left(\frac{1}{s\pi}\right)^{3/2}\sqrt{\frac{3}{s^2+12}}\exp\left(-\frac{v^2}{4s}-\frac{w^2}{4s}-\frac{3\left(2u+vs\right)^2}{4s\left(s^2+12\right)}\right). \tag{F.3}$$

As doing the high order derivatives numerically introduces many discretisation errors, we choose to tabulate the analytical closed form of these functions up to the necessary cut-off. For our choice to neglect all terms with $\alpha+\beta>10$, a total of 66 functions remain. The first few are presented below. The steady state solution is expressed in time integrals of the above functions.

$$\begin{aligned}
\delta g'_{00}\left(x,y,z,t\right) &= \tfrac{1}{4}\sqrt{\tfrac{3}{t^2+12}}\exp\left(-\tfrac{y^2}{4t}-\tfrac{z^2}{4t}-\tfrac{3}{4t}\tfrac{2x-yt}{t^2+12}\right)/\left(\pi^{\frac{3}{2}}t^{\frac{3}{2}}\right)\\
\delta g'_{01}\left(x,y,z,t\right) &= \left(-\tfrac{1}{4}\left(-t^2y+3tx+6y\right)\sqrt{\tfrac{3}{t^2+12}}\exp\left(-\tfrac{y^2}{4t}-\tfrac{z^2}{4t}-\tfrac{3}{4t}\tfrac{2x-yt}{t^2+12}\right)\right)/\left(\pi^{\frac{3}{2}}t^{\frac{5}{2}}\left(t^2+12\right)\right)\\
\delta g'_{02}\left(x,y,z,t\right) &= \left(\tfrac{1}{4}\left(-2t^5+t^4y^2-6t^3xy-30t^3+9t^2x^2-12t^2y^2+36txy-72t+36y^2\right)\sqrt{\tfrac{3}{t^2+12}}\exp\left(-\tfrac{y^2}{4t}-\tfrac{z^2}{4t}-\tfrac{3}{4t}\tfrac{2x-yt}{t^2+12}\right)\right)/\left(\pi^{\frac{3}{2}}t^{\frac{7}{2}}\left(t^2+12\right)^2\right)\\
\delta g'_{10}\left(x,y,z,t\right) &= \left(-\tfrac{3}{4}\left(-ty+2x\right)\sqrt{\tfrac{3}{t^2+12}}\exp\left(-\tfrac{y^2}{4t}-\tfrac{z^2}{4t}-\tfrac{3}{4t}\tfrac{2x-yt}{t^2+12}\right)\right)/\left(\pi^{\frac{3}{2}}t^{\frac{5}{2}}\left(t^2+12\right)\right)\\
\delta g'_{11}\left(x,y,z,t\right) &= \left(\tfrac{3}{4}\left(-t^4+t^3y^2-5t^2xy-12t^2+6tx^2-6ty^2+12xy\right)\sqrt{\tfrac{3}{t^2+12}}\exp\left(-\tfrac{y^2}{4t}-\tfrac{z^2}{4t}-\tfrac{3}{4t}\tfrac{2x-yt}{t^2+12}\right)\right)/\left(\pi^{\frac{3}{2}}t^{\frac{7}{2}}\left(t^2+12\right)^2\right)\\
\delta g'_{20}\left(x,y,z,t\right) &= \left(\tfrac{3}{4}\left(-2t^3+3t^2y^2-12txy-24t+12x^2\right)\sqrt{\tfrac{3}{t^2+12}}\exp\left(-\tfrac{y^2}{4t}-\tfrac{z^2}{4t}-\tfrac{3}{4t}\tfrac{2x-yt}{t^2+12}\right)\right)/\left(\pi^{\frac{3}{2}}t^{\frac{7}{2}}\left(t^2+12\right)^2\right)
\end{aligned}$$

To perform this time integration, we use Simpson's rule on a logarithmically spaced grid with a cutoff at $t=10^5$ using 200 grid points. To fulfil the boundary conditions we sum the result according to Eq. (B.20), where the coefficients $C_{\alpha\beta}$ are determined by the boundary conditions.

This determination is done by an expansion of the boundary conditions in terms of real spherical harmonics, see Eq. (B.23)

$$\frac{\partial T'_{\alpha\beta}}{\partial r'} - \frac{x'y'}{r'}T'_{\alpha\beta} = \sum_{l=0}^{\infty}\sum_{m=-l}^{l} j_{\alpha\beta}^{lm} Y_{lm}(\hat{\mathbf{r}}'). \tag{F.4}$$

Due to the orthonormality of the real spherical harmonics, the coefficients $j_{\alpha\beta}^{lm}$ are easily calculated to be

$$j_{\alpha\beta}^{lm} = \int_0^{2\pi} \mathrm{d}\phi \int_0^{\pi} \mathrm{d}\theta \sin(\theta) Y^{lm}(\theta,\phi) \left(\frac{\partial T'_{\alpha\beta}}{\partial r'} - \frac{x'y'}{r'}T'_{\alpha\beta} \right), \tag{F.5}$$

at $r' = \sqrt{2\mathrm{Pe}}$, where we used the standard convention of the spherical coordinates (polar angle θ, azimuthal angle ϕ). We perform the r'-derivative analytically (we evaluate it before the numerical time integration) and we apply the Lebedev quadrature for the angular integrals. We use the Lebedev scheme of degree 47, meaning that it exactly integrates any polynomial function up to that degree. A discretisation error is introduced for functions with higher oscillatory behaviour. If more precision is needed, a higher degree of accuracy can be chosen. We have found the degree to be sufficient as long as it is significantly higher than $l_{\max}$. This scheme approximates the integral by a sum of the function evaluated at 770 different grid points on the surface of a sphere, each with unique weights.

The last step is to solve the square linear system of Eq. (B.27). This is relatively common problem which can be performed by any suitable standard algorithm.

F.3 Integration of the Ornstein-Zernike relation

Here, we present a numerical procedure for solving the Ornstein-Zernike equation for spherical particles using the Percus-Yevick closure. Eqs. (2.2) and (2.7) are not analytically solvable in general. Therefore, we resort to numerics to find the pair correlation function and structure factor. For spherical particles, we define the discrete spatial grid $r_i = i\Delta_r$, $i \in \{1, \ldots, M-1\}$ and corresponding reciprocal grid $k_j = j\Delta_k$, $j \in \{1, \ldots, M-1\}$, where M is the number of grid points. We set $\Delta_r = M^{-1/2}$ and $\Delta_k = \pi M^{-1/2}$, such that $\Delta_r\Delta_k = \pi/M$. Now we discretise the functions $\Psi_i = r_i\psi(r_i)$ and $\hat{\Psi}_j = k_j\hat{\psi}(k_j)$, $\Psi \in \{\Gamma, C\}$. In terms of these discrete functions, Eqs. (2.2) and (2.7) become [147]

$$\hat{\Gamma}_j = \frac{n\hat{C}_j^2}{k_j - n\hat{C}_j}, \qquad \text{and} \qquad C_i = f_i(\Gamma_i + r_i) \tag{F.6}$$

respectively, with $f_i = \exp[-\beta U(r_i)] - 1$ the discrete Mayer function and $U(r_i)$ the interaction potential between the particles. We use the following procedure to find the solutions to Eqs. (F.6).

(i) Make an initial estimate for the function $\Gamma_i^{(0)}$. The guess $\Gamma_i^{(0)} = 0$ is satisfactory in our case. (ii) Find $C_i^{(0)}$ using (F.6), and (iii) transform to find $\hat{C}_j^{(0)}$ using the discrete sine transform

$$\hat{\Psi}_j = 4\pi\Delta_r \sum_{i=1}^{M-1} \Psi_i \sin\left(\frac{\pi ij}{M}\right) \qquad \text{for} \qquad j \in \{1, \ldots, M-1\}. \tag{F.7}$$

(iv) Find $\Gamma_j^{(1)}$ using Eq. (F.6) and (v) transform back to real space using

$$\Psi_i = \frac{\Delta_k}{2\pi^2} \sum_{j=1}^{M-1} \hat{\Psi}_j \sin\left(\frac{\pi i j}{M}\right) \qquad \text{for} \qquad i \in \{1, \ldots, M-1\} \tag{F.8}$$

to find a new estimate $\Gamma_i^{(1)}$. For high densities, it is necessary to mix this new estimate with the old estimate for better convergence. (vi) Check if the solution of $\Gamma_i^{(1)}$ has converged or diverged. If so, stop. In this work, we used the convergence criterion $(\zeta^{(t)})^2 = \sum_i \left(\Gamma_i^{(t)} - \Gamma_i^{(t-1)}\right)^2 < 10^{-10}$, and we label solutions as divergent if they did not converge within 10^6 recursive iterations. (vii) Repeat steps (i)–(vi) [147].